Diagnosing oxidation in the free troposphere and in cities over North America using space-based observations

By

Qindan Zhu

A dissertation submitted in partial satisfaction of the

requirements for the degree of

Doctor of Philosophy

in

Earth and Planetary Science

in the

Graduate Division

of the

University of California, Berkeley

Committee in charge:

Professor Ronald C. Cohen, Chair
Professor David Romps
Professor Allen Goldstein

Spring 2022

Diagnosing oxidation in the free troposphere and in cities over North America using space-based observations

by

Qindan Zhu

Abstract

Diagnosing oxidation in the free troposphere and in cities over North America using space-based observations

by

Qindan Zhu

Doctor of Philosophy in Earth and Planetary Science

University of California, Berkeley

Professor Ronald C. Cohen, Chair

The oxidative capacity of the troposphere – primarily characterized by the burden of the most abundant and reactive of oxidants, the hydroxyl radical (OH) – determines the lifetime of many trace gases of importance to climate and human health, including air pollutants and the greenhouse gas methane. In the upper troposphere, there is large uncertainty in the oxidative capacity associated with the lightning NO_x production, for which reported results range from 16-700 mol NO flash^{-1}. I implemented a lightning parameterization which significantly improves the representation of lightning in one chemical transport and and showed that this parameterization should be more effective in any model. I combined the model simulations configured with this new lightning parameterization with the satellite observations of NO_2 column to yield a better estimate of lightning NO_x production over the continental US. In cities, urban OH controls the removal rate of primary pollutants and triggers the production of ozone. Interannual trends of OH in urban areas are not well documented or understood due to the short lifetime and high spatial heterogeneity of OH and of OH precursors. Here I synthesized a machine learning technique, satellite observations and simulations from a state-of-art chemical transport model to estimate OH trends between 2005 and 2014 in 49 North American cities. I described trends in the summertime OH with wide variation among different cities. The variation of OH is explained by the shift in chemical regime from one where additional NO_x slows chemistry to one where additional NO_x speeds chemistry over the years. The identification of chemical regime, in turn, sheds light on the effective policy for controlling ozone.

To everyone I love.

Contents

List of Figures

List of Tables

Acknowledgments

Thanks to my advisor, Ron Cohen, for your immense support and guidance. I would like to thank you for encouraging my research and boosting my confidence. Your advice on both research as well as on my career have been invaluable.

Thanks to David Romps, David Shuster, Tina Chow and Allen Goldstein, for serving as my qualifying and dissertation committee members,

Thanks to Josh Laughner, my mentor in Cohen group, my co-author on all three chapters. I cannot imagine how my Ph.D would be without you. Thanks so much for flying back to Berkeley to attend my after-Qual party. It was a big surprise for me.

Thanks to my lab cohorts, Helen Fitzmaurice and Bryan Place for being the best same-year peers, Hannah Kenagy for bring so much laughter into our lab, Erin Delaria and Naomi Asimow for being great office mates, Paul Wooldridge for the daily greeting, Milan Patel, Anna Winter and Yishu Zhu for taking over responsibilities of organizing group events.

Thanks to my close friends, Amy Gawon Sung for being my first friend when I arrived at US, Nam Maneerat for living with me for two years, Yuexin Li for being the best company when we got trapped at home during pandemic.

Thanks to my parents, Suilan Jin and Jiang'an Zhu, and my brother, Ting Zhu, for their unconditional love. Special shout-out to my Mom. You are the strongest woman I know and has been my role model in life. Thanks to my boyfriend, Songhe Hu. You are always the one I turned to when I got stuck and doubted myself. The confidence that you offered to me is what sustained me this far.

I gratefully thank support from NASA Grant 80NSSC19K0945. I acknowledge high-performance computing support from Savio computational cluster resource provided by the Berkeley Research Computing program at the University of California, Berkeley (supported by the UC Berkeley Chancellor, Vice Chancellor for Research, and Chief Information Officer). I acknowledge use of the WRF-Chem preprocessor tools MOZBC provided by the Atmospheric Chemistry Observations and Modeling (ACOM) laboratory of NCAR.

Chapter 1

Introduction

1.1 Oxidation capacity in the troposphere

The atmosphere is a recipient of various trace gases emitted by both natural sources and as a result of anthropogenic activities. Although trace gases constitute only a tiny fraction of air, they are responsible for driving the majority of the chemistry in the troposphere and trigger substantial influences on global climate and air quality. For instance, methane (CH_4) is only about 2 parts per million of the molecules in air, yet it contributes to roughly one-fifth of the increase in radiative forcing by human-linked greenhouse gases (Nisbet et al., 2014). Another example are the volatile organic compounds (VOCs) and nitrogen oxides ($NO_x \equiv NO+NO_2$) that range from parts per trillion to 10s of parts per billion of air and are two dominant groups of pollutants affecting local air quality. These trace gases are directly emitted to the atmosphere and are commonly referred to as primary. They undergo chemical reactions to form secondary air pollutants such as ozone (O_3) and aerosols. Both ozone and aerosols lead to adverse impacts on human and ecosystem health, agricultural productivity, and climate (e.g. Jerrett et al., 2009; Anenberg et al., 2010; Mauderly and Chow, 2008). Once emitted, trace gases stay in the atmosphere until physically removed (e.g. by depositing to the earth's surface) or chemically transformed (e.g. converted to CO_2 or HNO_3). As a result, the abundances of atmospheric trace gases are determined by both emission strengths and lifetimes to removal from or chemical conversion within the atmosphere. The ability to chemically remove these trace gases and prevent them from endless growing is referred as oxidation capacity.

The most important oxidant is the hydroxyl radical (OH). OH reacts with almost all pollutants thereby initializing their ultimate removal from the atmosphere. Other oxidants such as Cl or NO_3 are known, but their effects on global and urban oxidation rates are small compared to OH. Since reaction with OH is in many cases the rate-determining step in this chemical sequence leading to oxidation to stable end products such as CO_2 and since the other oxidants have only a small fraction of the effect of OH, the OH concentration is a mea-

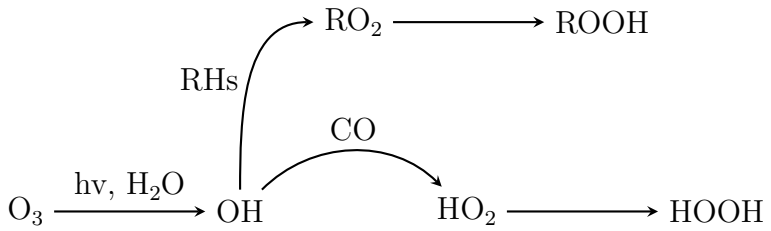

Figure 1.1: Simplified schematic of OH chemistry without OH cycling by NO.

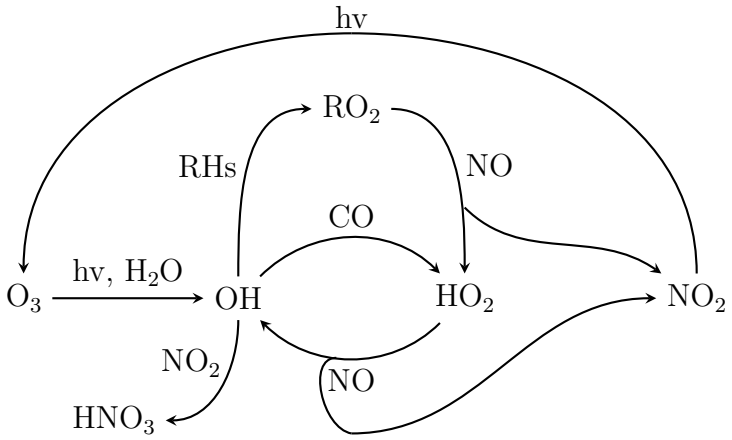

Figure 1.2: Simplified schematic of OH chemistry with the presence of NO_x.

sure for the atmosphere's oxidation capacity. Thus understanding the spatial and temporal variation of OH is of fundamental importance to both atmospheric chemistry and climate science.

1.2 The role of NO_x in trospospheric OH chemistry

The abundance of OH in the troposphere changes rapidly on a wide variety of spatial and temporal scales. Due to the high reactivity of OH (τ = 0.01–1.00s), the effects of air mass transport can be ignored and the OH concentration is dependant only on the solar irradiance and in situ chemical environment(Logan et al., 1981). Depicted in Fig. 1.1 and Fig. 1.2, NO_x plays a dominant role among all trace gases associated with OH chemistry.

In environment where NO_x abundance is negligible (Fig. 1.1), the primary OH production occurs when water vapor reacts with the reactive singlet oxygen atom, $O(^1D)$, the product of ozone photolysis by the ultraviolet radiation at wavelengths less than 310 nm. The photolysis of formaldehyde (HCHO), which leads to production of HO_2 and then converts to OH, is also considered important in producing OH. There are other minor OH productions pathways such as photolysis of nitrous acid (HONO) (Ren et al., 2006) and alkene ozonolysis reactions

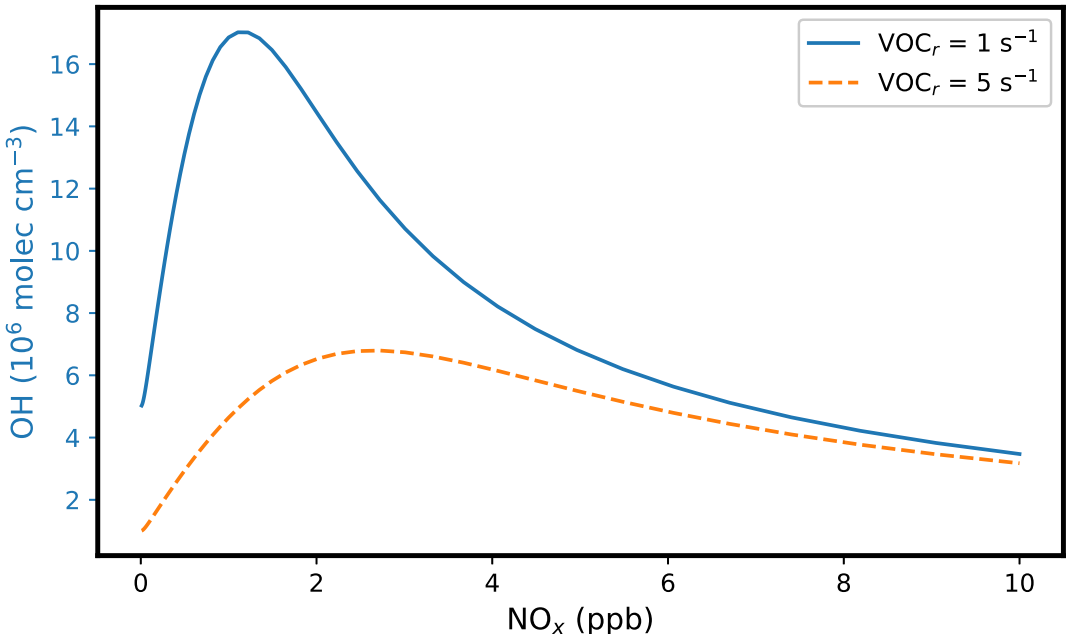

Figure 1.3: A schematic of OH as a function of NO_x at the photochemical steady state. Two scenarios represent a high VOC reactivity ($VOC_r = 5\ s^{-1}$) condition and low VOC reactivity condition ($VOC_r = 1\ s^{-1}$), respectively.

(Donahue et al., 1998), which are important during winter or at night.

$$O_3 + hv \longrightarrow O(^1D) + O_2 \tag{1.1}$$
$$O(^1D) + H_2O \longrightarrow 2\,OH \tag{1.2}$$

The OH loss paths attribute to the oxidation of CO and VOCs (also referred as hydrocarbons (RHs)). OH rapidly reacts with CO to form CO_2 an H atom that quickly combines with O_2 to form hydroperoxy free radicals, HO_2. OH also reacts with VOCs by adding to a double bond or removing hydrogen to form organic free radical (R), which then adds to O_2 resulting in formation of organic peroxy radicals (RO_2) (Jacob, 1999). The radical reaction chains are terminated by radical–radical reactions that form hydroperoxides (ROOH and HOOH).

$$OH + CO \longrightarrow CO_2 + H \tag{1.3}$$
$$H + O_2 \longrightarrow HO_2 \tag{1.4}$$
$$OH + RH \longrightarrow R + H_2O \tag{1.5}$$
$$R + O_2 \longrightarrow RO_2 \tag{1.6}$$

The presence of NO_x alters this chemistry (Fig. 1.2). Besides the primary production path by $O(^1D)$ reacting with H_2O, secondary OH can form by HO_2 reacting with NO. Typically, in the atmosphere this secondary production path is a factor of five faster than the primary (Ehhalt, 1999), accelerating OH production rates. In parallel, the byproduct of NO reacting with HO_2 is NO_2, which undergoes photolysis by the solar radiation at the wavelengths less than 430 nm resulting in a sequence that forms O_3 and reforms NO (Reactions 1.7-1.9) (Crutzen, 1979). As a consequence, NO_x serves as catalyst in the OH cycle and fuels primary OH production.

$$HO_2 + NO \longrightarrow OH + NO_2 \tag{1.7}$$

$$NO_2 + hv \longrightarrow NO + O(^3P) \tag{1.8}$$

$$O(^3P) + O_2 \longrightarrow O_3 \tag{1.9}$$

NO_x plays a dual role. It promotes OH productions. It also leads to removing OH from the environment by OH reacting with NO_2 to form HNO_3.

$$OH + NO_2 \longrightarrow HNO_3 \tag{1.10}$$

The NO_x contribution to both production and loss pathways of OH results in a nonlinear relationship between OH and NO_x (Fig. 1.3). At low NO (referred as a NO_x limited regime), VOCs are more competitive than NO_x for reacting with OH so that HO_2 and RO_2 radical–radical reactions dominate HO_x chemistry. The OH formation through radical cycling overwhelms the OH loss due to HNO_3 formation, leading an increase with concurrent increase of NO_x. In the high NO_x condition (referred as a NO_x suppressed regime), OH is more prone to react with excess NO_2 than VOCs, terminating radical cycle and forming HNO_3. Since OH loss by NO_x dominants the chemical system, higher NO_x leads to lower OH. The overturn point between NO_x limited and NO_x suppressed is determined by the VOC reactivity (defined as the aggregate rate of all reactions of VOC with OH, the sum over the product of the individual rate constants for OH reaction and the concentration of each VOC) in the air mass. With more VOCs reacting with OH to initiate OH cycle, it allows for more NO to convert HO_2 to OH until OH cycle is hampered by OH reacting with NO_2.

1.3 OH in the free troposphere

The boundary layer is a dividing line in the troposphere. Within the boundary layer, the influence of anthropogenic emissions are concentrated and immediate. Most of the human activities leading to emissions occur within the boundary layer (aircrafts are a prominent exception). OH in the free troposphere, above the boundary layer, governs the global mean

oxidative capacity (Jaeglé et al., 2001; Lelieveld et al., 2004) and determines the lifetime of greenhouse gases such as CH_4 and trospospheric O_3.

Airborne measurements since late 1990s have included observations of OH in the free troposphere. Comparing observed OH to calculated values from a photochemical box model that is constrained with simultaneous measurements of environmental conditions and chemical constituents has advanced our understanding of OH chemistry. Early OH measurements occurred in 1995 on the NSF C-130 aircraft over the Pacific Ocean (Mauldin III et al., 1998). They showed a remarkably good agreement with box model calculations. In October 1995 and August 1996, OH measurements were made using NASA ER-2 aircraft in the upper troposphere both near Hawaii and near California (Wennberg et al., 1998). The observed OH was twice the modeled OH. The discrepancy was resolved by recognizing the importance of acetone photolysis as a source of OH that was not included in the original model. However, later studies showed that the photolysis frequency of acetone at upper tropospheric temperatures is too small to make an important contribution (Blitz et al., 2004). Another airborne measurements in 1996 on NASA DC-8 flight found observed OH more than 4 times higher than the model (Brune et al., 1998) and hypothesized the missing OH sources such as photolysis of HCHO and other oxygenated volatile organic compounds (OVOCs). Subsequent airborne studies in the 21st century were equipped with measurements of additional chemical constituents. These more complete descriptions of chemicals present resulted in better agreement between OH observations and model calculations (e.g. Cantrell et al., 2003; Olson et al., 2012; Ren et al., 2012; Brune et al., 2018; Brune et al., 2020).

These airborne studies highlighted that OH variability is driven by NO_x variability in the free troposphere. Natural NO_x emissions result from an inhomogeneous set of sources including microbial processing of nitrogen in soils and lightning. Lightning is the largest source of NO_x emissions to the free troposphere, contributing more than 80% of the total NO_x emissions there (Murray, 2016). Lightning can inject an enormous amount of NO_x in a short time. Since it lacks co-emission of VOCs that would counteract the influence from NO_x, the near field is converted to a NO_x limited environment. As a result, OH sees an significant enhancement along with the emitted NO_x from lightning. Brune et al. (2021) described the distribution of OH measured on the NASA DC-8 aircraft flying through anvils of deep convective clouds during the Deep Convective Clouds and Chemistry (DC3) field study in the summer of 2012. The observed OH in the outflow of deep convection was orders of magnitude greater than any previous atmospheric observation.

The quantification of lightning induced OH remains highly uncertain. Murray et al. (2013) illustrated that variability in global mean OH is most sensitive to lightning of any major emission source. Mao et al. (2021) found that lightning-produced oxidants can increase global mass weighted OH by 0.3%–10%, whereas Brune et al. (2021) estimated the contribution to be 2 to 16% of global OH oxidation. The major source of uncertainty is the wide spread in estimates of lightning NO_x emission rate, ranging from 16 to 700 mol NO flash^{-1} (DeCaria

et al., 2005; Hudman et al., 2007; Martin et al., 2007; Schumann and Huntrieser, 2007; Huntrieser et al., 2009; Beirle et al., 2010; Bucsela et al., 2010; Jourdain et al., 2010; Ott et al., 2010; Miyazaki et al., 2014; Liaskos et al., 2015; Pickering et al., 2016; Pollack et al., 2016; Laughner and Cohen, 2017; Nault et al., 2017). Better constraining the lightning NO_x emission rate is crucial to accurately describe the OH enhancement associated with lightning occurrence and the overall global tropospheric OH.

In Chapter 2, I present an estimate of lightning NO_x production rates using satellite observations and model simulations. I first implement a lightning parameterization using the product of convective available potential energy (CAPE) and convective precipitation rate (PR) coupled with the Kain– Fritsch convective scheme (KF/CAPE-PR) within the Weather Research and Forecasting-Chemistry (WRF-Chem) model. I show that this CAPE-PR parameterization improves the correlation of lightning flash density when comparing against the Earth Networks Total Lightning Network. I then run a series of model simulations configured with KF/CAPE-PR parameterization and a range of lightning NO_x production rates until the model matches to NO_2 satellite observations, and conclude that the lightning NO_x production rate of 500 mol NO $flash^{-1}$ yields the best agreement.

1.4 OH in cities

Cities are characterized by dense population and prevalent pollution. By 2050, two-thirds of the Earth's projected population of 9.3 billion is expected to reside within urban areas (Seto et al., 2014). Feature growing population, cities endure severe direct impact on human health due to pollution exposure. For instance, ambient fine particulate matter air pollution is responsible for 85,000 to 200,000 excess deaths per year in the United States, the majority of the excess deaths are in cities (Burnett et al., 2018). In other parts of the world, the situation is worse, with higher particle exposure and higher death rates (Manisalidis et al., 2020). Since OH is the key species in controlling local pollution, understanding OH chemistry and constraining the OH abundance in cities is of particular importance to predicting the efficacy of policies aimed at improving the air quality and eliminating heavy pollution.

The extremely low concentration and the high reactivity of OH make routine measurements of OH impossible with current technologies. As a result, there have been relatively few field experiments to measure OH abundance and investigate OH chemistry in cities. As summarized in Table 1.1, OH was measured in 12 cities over the past 30 years.

These ground measurements show a distinction in OH chemistry between summer and winter. During the PUMA (Pollution of the Urban Midlands Atmosphere) field campaign in the city of Birmingham, UK, the observed summertime OH at midday was two times that in winter (Emmerson et al., 2005b; Emmerson et al., 2005a). A larger seasonal difference in OH was found in Tokyo, Japan. The observed OH was enhanced by a factor of four in summer compared to winter in the same year during IMPACT (Integrated Measurement Program

for Aerosol and oxidant Chemistry in Tokyo) field campaign (Kanaya et al., 2007). The same conclusion was reached using observations in New York City, OH and HO_2 measured during winter in 2004 (Ren et al., 2006) were lower by a factor of 5 than in summer of 2001 (Ren et al., 2003). The difference is explained by a combination of effects. There is reduction in OH production from ozone photolysis and increased OH productions by reactions of ozone with alkenes, carbonyl photolysis and HONO photolysis in winter. At the same time, concentrations of NO_x are higher and OH lifetimes are shorter.

Among the urban OH observations in summer, there exists a wide spread across cities. The lowest summertime midday OH of 3×10^6 molecule cm^{-3} was observed in Birmingham, UK during PUMA-1 field campaign (Emmerson et al., 2005a), while the highest midday OH was up to 2.6×10^7 molecule cm^{-3} in the Pearl River Delta, China in 2006. There are only a few cities where OH observations have been made more than once, allowing for an investigation of annual variability of OH. The midday median OH observed in Houston decreased from 1.6×10^7 molecule cm^{-3} in 2000 to 1.2×10^7molecule cm^{-3} in 2006 (Mao et al., 2010), and was further reduced to 8×10^6 molecule cm^{-3} in 2009 (Ren et al., 2013). A more drastic decrease in OH was observed in Pearl River Delta; the observed OH in 2004 (Lu et al., 2012) was 2-4 times higher than it was in 2014 (Tan et al., 2019b). In contrast, Los Angeles and Beijing showed the same range of observed OH even though the observations were 17 years apart in Los Angeles (George et al., 1999; Griffith et al., 2016) and 8 years apart in Beijing (Lu et al., 2013; Tan et al., 2019a).

Meteorological conditions partially explain the OH difference. Rohrer and Berresheim (2006) presented a tight correlation between observed OH and ozone photolysis frequency, $J(O^1D)$, which is determined by the solar irradiance. Even though this correlation was based on OH measurements at a rural sites, similar correlations between OH and $J(O^1D)$ were reported in urban measurements as well (e.g. Griffith et al., 2016; Lu et al., 2012; Lu et al., 2013). Citywise comparison also addressed the importance of solar irradiance. Mao et al. (2010) compared the OH observations in four field studies: TEXAQS2000, NYC2001, MCMA2003 and TRAMP2006, and found that the lowest OH observations occurred in the New York City and could be explained in part by the lower OH sources due to lower $J(O^1D)$.

Besides effects of meteorological conditions, the large OH variation across cities is primarily the result of a wide range of NO_x and VOC conditions (Stone et al., 2012). NO_x is mainly generated by anthropogenic combustion of fuels from traffic, industrial processes and household activities (Steinfeld, 1998). Anthropogenic VOC emissions from vehicles (Warneke et al., 2012) as well consumer and industrial products (collectively "volatile chemical products," VCPs) (McDonald et al., 2018; Coggon et al., 2021) are important in the chemistry of cities and biogenic VOC may also play a role. Since NO_x and VOC emissions introduce intricate chemical conditions across cities, it is impossible to generalize OH chemistry from the cities where measurements have been made to other urban regions except by reference to the concentrations of NO_x and VOC.

In Chapter 2, I explore a machine learning (ML) approach to constrain the OH abundance in a range of cities without direct OH observations. This approach accounts for the variations in meteorological and chemical conditions. I train this ML model based on the parameters simulated from the WRF-Chem model, and it suggests that six observable predictive parameters are capable of explaining 76% of the OH variability. The parameters are the tropospheric NO_2 column, the tropospheric HCHO column, $J(O^1D)$, H_2O, temperature, and pressure. I then use observations of the tropospheric NO_2 column and HCHO column from satellite observations along with meteorological observations as input to the ML model to enable measurement-based prediction of daily near surface OH at 1:30 pm local time. The result is validated by comparing the OH predictions to measurements of isoprene, which has a source that is uncorrelated with OH and is removed rapidly and almost exclusively by OH in the daytime. I demonstrate that the predicted OH is, as expected, anticorrelated with isoprene. I also show that this ML model is consistent with our understanding of OH chemistry.

In Chapter 4, I utilize machine learning with observational inputs emphasizing satellite remote sensing observations to predict surface OH in 49 North American cities from 2005 to 2014. I observe changes in the summertime OH over one decade, with wide variation among different cities. In 2014, compared to the summertime OH in 2005, 3 cities show a significant increase of OH, whereas, in 27 cities, OH decreases in 2014. The year to year variation of OH is mapped to the decline of the NO_2 column. I conclude that the cities in this analysis are either in the NO_x-limited regime or at the transition from a NO_x suppressed regime to a NO_x-limited regime. The result emphasizes that, in the future, controlling NO_x emissions will be most effective in regulating the ozone pollution in these cities.

Campaign	Date	City	Measured OH (10^6 mole cm^{-3})	Reference
LAFRE	Sep 1993	Los Angeles, CA, US	5.5 (midday)	George et al. (1999)
SOS	Jun-Jul 1999	Nashville, TN, US	16 (noon)	Martinez et al. (2003)
PUMA-1	Jun 1999	Birmingham, UK	3 (midday)	Emmerson et al. (2005b)
PUMA-2	Jan-Feb 2000	Birmingham, UK	1.5 (midday)	Emmerson et al. (2005a)
TEXAQS	Aug-Sep 2000	Houston, Texas, US	16 (midday median)	Mao et al. (2010)
PMTACS-1	Jun-Aug 2001	New York City, NY, US	5-20 (daytime)	Ren et al. (2003)
MCMA	Apr 2003	Mexico City, Mexico	7 (midday median)	Shirley et al. (2006)
TORCH	Jul-Aug 2003	Essex, UK	1.2-7.5 (daytime)	Emmerson et al. (2007)
IMPACT IV	Jan-Feb 2004	Tokyo, Japan	1.5 (midday median)	Kanaya et al. (2007)
IMPACT L	Jul-Aug 2004	Tokyo, Japan	6 (midday median)	Kanaya et al. (2007)
PMTACS-2	Jan-Feb 2004	New York City, NY, US	1.4 (daytime)	Ren et al. (2006)
MILAGRO	Mar 2006	Mexico City, Mexico	5-10 (midday)	Dusanter et al. (2009)
PRIDE	Jul 2006	Pearl River Delta, China	15-26 (daily maximum)	Lu et al. (2012)
TRAMP	Aug-Sep 2006	Houston, TX, US	12 (midday median)	Mao et al. (2010)
CARE	Aug-Sep 2006	Beijing, China	4-17 (daily maximum)	Lu et al. (2013)
SHARP	Apr-May 2009	Houston, TX, US	8 (midday median)	Ren et al. (2013)
MEGAPOLI	Jul 2009	Paris, France	5 (daytime maximum)	Michoud et al. (2012)
CALNex-LA	May-Jun 2010	Los Angeles, CA, US	4-8 (midday)	Griffith et al. (2016)
ClearfLo	Jul-Aug 2012	London, UK	6-9 (midday)	Whalley et al. (2018)
CARE-2	Jul 2014	Beijing, China	4-8 (midday)	Tan et al. (2019a)
PRIDE-PRD2014	Oct-Nov 2014	Pearl River Delta, China	4.5 (midday maximum median)	Tan et al. (2019b)

Table 1.1: OH measurements in polluted urban environments

Chapter 2

Lightning NO_2 simulation over the Contiguous US and its effects on satellite NO_2 retrievals

The chapter was adapted from: Q. Zhu, J. L. Laughner, and R. C. Cohen (2019c). "Lightning NO 2 simulation over the contiguous US and its effects on satellite NO 2 retrievals". *Atmospheric Chemistry and Physics* 19.20, pp. 13067–13078

2.1 Introduction

Nitrogen oxides ($NO_x \equiv NO + NO_2$) are key species in atmospheric chemistry, affecting the oxidative capacity in the troposphere by regulating the ozone and hydroxyl radical concentrations (Crutzen, 1979). Anthropogenic sources (mainly fossil fuel combustion) are the largest contributor to the NO_x budget on a global scale. Natural sources of NO_x are also nonnegligible (Denman et al., 2007). While anthropogenic emissions of NO_x are intensively studied, natural sources are less understood (Delmas et al., 1997; Lamsal et al., 2011; Miyazaki et al., 2012). Lightning contributes to ~10% of NO_x budget on a global scale and represents over 80% of NO_x in the upper troposphere (UT) (Schumann and Huntrieser, 2007; Nault et al., 2017). Over the US, the anthropogenic NO_x emissions have been decreasing rapidly (Russell et al., 2012; Lu et al., 2015), making lightning an increasingly important source of NO_x and an increasingly large fraction of the source of column NO_2. Ozone (O_3) in UT has long lifetime and leads to a more pronounced radiative effect than ozone elsewhere in the troposphere. Varying lightning NO_x emission (LNO_x) by a factor of four (123 to 492 mol NO $flash^{-1}$) yields up to 60 % enhancement of UT O_3 and increases the mean net radiative flux by a factor of three (Liaskos et al., 2015). This range in the lightning NO_x production rate is similar to the current uncertainty of estimated lightning emission rates. Further, incorrect representation of LNO_x in a priori profiles for satellite NO_2 retrievals leads to biases

in the retrieved NO_2 columns. This is exacerbated by the greater sensitivity of UV/Vis NO_2 retrievals to the UT (e.g. Laughner and Cohen, 2017; Travis et al., 2016).

When lightning occurs, NO is emitted as a result of high temperatures and NO_2 forms through rapid photochemistry. Studies report the estimated LNO_x production rate ranges widely from 16 to 700 mol NO $flash^{-1}$ (DeCaria et al., 2005; Hudman et al., 2007; Martin et al., 2007; Schumann and Huntrieser, 2007; Huntrieser et al., 2009; Beirle et al., 2010; Bucsela et al., 2010; Jourdain et al., 2010; Ott et al., 2010; Miyazaki et al., 2014; Liaskos et al., 2015; Pickering et al., 2016; Pollack et al., 2016; Laughner and Cohen, 2017; Nault et al., 2017).

Two categories of methods, one emphasizing the near-field of lightning NO_x and the other the far-field, have previously been applied to estimate LNO_x. In near-field approaches the total NO_x from direct observation close to the lightning flashes is divided by the number of flashes from a lightning observation network to yield the NO_x per flash (e.g. Schumann and Huntrieser, 2007; Huntrieser et al., 2009; Pollack et al., 2016). Near-field estimates of LNO_x per flash have also been made through use of cloud-resolved models with LNO_x constrained by observed flashes and aircraft data from storm anvils (e.g. DeCaria et al., 2005; Ott et al., 2010; Cummings et al., 2013). In contrast, the far-field approach uses downwind observations to constrain a regional or global chemical transport model. The emission rate of lightning NO_x is varied in the model (either ad hoc or through formal assimilation methods) until the modeled NO_x agrees with the measurements of total NO_x at the far field location (Hudman et al., 2007; Martin et al., 2007; Jourdain et al., 2010; Miyazaki et al., 2014; Liaskos et al., 2015; Laughner and Cohen, 2017; Nault et al., 2017). In general, far-field approaches yield estimates of LNO_x at the upper end of reported range, while estimates from the near-field studies are typically at the lower end of the range. Nault et al. (2017) showed that a large part of this discrepancy is because prior near-field studies assume a long NO_x lifetime in the UT, while active peroxy radical chemistry in the near field leads to a short NO_x lifetime (˜3 h). Without accounting for this chemical loss, the near-field and far-field estimates are biased low compared to each other. However, this effect cannot completely reconcile the discrepancy between LNO_x reported from near- and far- field studies.

In chemical transport models, LNO_x production is modeled by assuming a fixed number of moles of NO are produced per lightning flash, typically 250 or 500 mol NO $flash^{-1}$ (Zhao et al., 2009; Allen et al., 2010; Ott et al., 2010). This presents an additional challenge to the far-field approaches to constrain LNO_x, as errors in the simulation of lightning flashrate will propagate into errors in the LNO_x production per flash. However, explicitly simulating the cloud scale processes that produce lightning is generally too computationally expensive to be applied in a regional or global model as it requires spatial resolution at the scale of cloud processes. Instead, the convection is parameterized using simplified convection schemes. Lightning is then parameterized by a suite of convection parameters. The most prevalent lightning parameterization relates lightning to the cloud top height (CTH) (Price and Rind,

1992; Price et al., 1997). Price and Rind found a consistent proportionality between cloud-to-ground (CG) lightning flashes and the fifth power of cloud top height. Other meteorological variables, including upward cloud mass flux (UMF), convective precipitation rate (CPR), convective available potential energy (CAPE), cloud ice flux (ICEFLUX) have been suggested as alternative lightning proxies for CG flashes or in some cases total flashes (Allen and Pickering, 2002; Choi et al., 2005; Wong et al., 2013; Romps et al., 2014; Finney et al., 2014). When CG flashes are predicted, the total lightning rate, including CG and Intra-Cloud (IC) flashes, is derived by defining a regional dependent CG:IC ratio (Boccippio et al., 2002).

Several previous studies have evaluated the performance of these lightning parameterizations in regional and global models. Tost et al. (2007) concluded none of them accurately reproduce the observed lightning observations even though some are inter-comparable. Wong et al. (2013) showed that a model using the Grell-Devenyi ensemble convective parameterization and the CTH lightning parameterization simulates erroneous flash count frequency distribution over time while the integrated lightning flash count is consistent with the observation. Luo et al. (2017) tested the single-variable parameterizations (CTH, CAPE, UMF, CPR) and the paired parameterizations based on power law relationship (CAPE-CTH, CAPE-UMF, UMF-CTH), each of which was coupled with Kain Frisch convective scheme, and demonstrated that the two-variable parameterization using CAPE-CTH improves upon the previous single-variable parameterizations; it captures temporal change of flash rates but the simulated spatial distribution is still not satisfactory.

In this study, we implemented the CAPE-PR lightning parameterization (Romps et al., 2014) into WRF-Chem and assess the performance in reproducing lightning flash density. Our motivation is to produce a better representation of a proxy-based lightning parameterization in the regional chemistry transport model. We also evaluate the effect of modeled lightning NO_x on both the a priori profiles used in satellite NO_2 retrievals and the retrievals themselves.

2.2 Methods: models and observations

WRF-Chem

This study applies the Weather Research and Forecast Model coupled with Chemistry (WRF-Chem) version 3.5.1 to the time periods May to June, 2012 and August to September, 2013. The model domain covers North America from 20 °N to 50 °N with 12 km×12 km horizontal resolution and 29 vertical layers. The North American Regional Reanalysis (NARR) provides initial and boundary conditions. Temperature, wind direction, wind speed and water vapor are nudged every 3 h towards to NARR product. Chemistry initial and boundary conditions are provided by the Model for Ozone and Related Chemistry Tracers (MOZART, `https://www.acom.ucar.edu/wrf-chem/mozart.shtml`). Anthropogenic emissions are driven by the National Emissions Inventory 2011 (NEI 11), with a scaling

factor to match the total emissions to 2012 emission from the Environmental Protection Agency (EPA, 2016). Biogenic emissions are driven by the Model of Emissions of Gases and Aerosol from Nature (MEGAN; (Guenther et al., 2006)). We use a customized version of the Regional Atmospheric Chemistry Mechanism version 2 (RACM2), the details are described by Zare et al. (2018).

The default lightning parameterization used in WRF-Chem is based on cloud top height (CTH). The parameterized lightning flash rates are proportional to a power of cloud top height with linear scaling varied by region:

$$f = \begin{cases} 3.44 \times 10^{-5} H^{4.9} & \text{Continental} \\ 6.20 \times 10^{-4} H^{1.73} & \text{Marine} \end{cases} \tag{2.1}$$

where f is the CG flash rate in each grid and H is the colocated cloud top height in units of kilometers.

We also implement an alternative lightning parameterization where lightning flash rates are defined to be proportional to the product of the convective available potential energy (CAPE) and precipitation rate (PR).

$$f = \begin{cases} 0.9 \times 10^{-4} \times E \times PR & \text{Southeastern CONUS} \\ 1.8 \times 10^{-4} \times E \times PR & \text{Elsewhere CONUS} \end{cases} \tag{2.2}$$

where f the CG flash rate in each grid cell, E the convective available potential energy and PR the convective precipitation rate. Southeastern CONUS in the context is the region between 94 °W to 76 °W and 25 °N to 37 °N. This parameterization was proposed by Romps et al. (2014). Romps et al. (2014) used a year-round observation of lightning and meteorological parameters and found a good correlation between observed lightning flash densities and observed CAPE times PR over the CONUS. CAPE-PR was further examined in Tippett and Koshak (2018) who computed the proxy in a numerical forecast model and found a fairly good agreement between the spatial pattern of the daily CG flash rate and the forecast proxy over 2003-2016. To our knowledge CAPE-PR parameterization has not previously been coupled with chemistry. Note that we compute these two meteorological variables every 72 seconds in our model setup and produce lightning flash rates in a much shorter time step compared to Romps et al. (2014) and Tippett and Koshak (2018). We also apply a regional scaling factor of 0.5 to the southeastern US (See Sec 2.3).

We analyze WRF-Chem outputs from three model runs. The first run, referred as "G3/CTH", is consistent with Laughner and Cohen (2017); it selects the Grell 3D ensemble cumulus convective scheme (Grell, 1993; Grell and Dévényi, 2002) and the CTH lightning parameterization. The Grell 3D convective scheme readily computes the neutral buoyancy level which serves as the optimal proxy for cloud top height (Wong et al., 2013). The "G3/CTH" is the only option for the coupled convective-lighting parameterization used

in WRF-Chem at a non-cloud resolving resolution (12 km). In addition, we run WRF-Chem with the CTH lightning parameterization coupled with the Kain-Fritsch cumulus convective scheme (Kain and Fritsch, 1990; Kain, 2004) ("KF/CTH") to test the effect of switching convective schemes. In the "KF/CTH" parameterization, the cloud top height is the level where the updraft vertical velocity equals to zero. Another run, referred as "KF/CAPE-PR", selects the Kain-Fritsch cumulus convective scheme and the CAPE-PR lightning parameterization described above. Compared to the Grell 3D convective scheme, the Kain-Fritsch uses the depletion of at least 90% CAPE as the closure assumption and calculates CAPE on the basis of entraining parcels instead of undiluted parcels, which also improves the calculation of precipitation rate (Kain, 2004). The lightning NO_x production rate is defined to be 500 mol NO flash^{-1}. The CG:IC ratio and the LNO_x post-convection vertical distribution are the same as used by Laughner and Cohen (2017).

ENTLN lightning observation network

To assess the performance of the lightning parameterizations we compare to lightning flashes from Earth Networks Total Lightning Network (ENTLN). ENTLN employs over 100 sensors across the United States and observes both CG and IC pulses (`https://www.earthnetworks.com/why-us/networks/lightning/`). All lightning pulses within 10 km and 700 ms of each other are grouped as a single flash. The IC and CG flashes are summed over the grid spacing defined in WRF-Chem.

Compared to National Lightning Detection Network (NLDN), ENTLN is selected for high detection efficiencies of both CG and IC flashes. The average detection efficiency for total flashes observed by ENTLN was 88% over CONUS relative to the space-based Tropical Rainfall Measurement Mission (TRMM) Lightning Imaging Sensor (LIS) (Lapierre et al. (2020), private communication). Shown in Fig. A.2, we matched the ENTLN data to LIS flashes both in time and space after the correction of LIS data based on its detection efficiency (Cecil et al., 2014) during May 13-June 23, 2012. It shows a median correlation ($R^2 = 0.51$) with the slope of 1.0, indicating the ENTLN data during the study time period is in agreement with the LIS observation. We use the ENTLN for analysis as reported and consider the detection efficiency of ENTLN as a source of uncertainty when comparing the modeled lightning flashes.

In Situ Aircraft Measurements

We compare our simulations to observations from aircraft campaigns that focus on deep convection. The Deep Convective Clouds and Chemistry (DC3) campaign (Barth et al., 2015) took place during May and June of 2012 over Colorado, Oklahoma, Texas and Alabama. The Studies of Emissions and Atmospheric Composition, Clouds, and Climate Coupling by Regional Surveys (SEAC4RS) (Toon et al., 2016) took place during August and September of 2013; most of the flight tracks occurred over the southeastern US. Both aircraft campaigns

		G3/CTH	KF/CTH	KF/CAPE-PR
Southeastern	Slope	2.08	0.94	0.96
	R^2	0.30	0.67	0.72
Elsewhere	Slope	0.98	0.54	1.19
	R^2	0.27	0.48	0.62

Table 2.1: Correlation statistics between observed and modeled (G3/CTH, KF/CTH, KF/CAPE-PR) flash density per day averaged by regions

flew into and out of storms and sampled deep convection. The combination of these two aircraft campaigns cover the regions with the most active lightning in the domain.

Satellite Measurements

The Ozone Monitoring Instrument (OMI) is an ultraviolet/visible (UV/Vis) nadir solar backscatter spectrometer launched in July 2004 on board the Aura satellite. It detects backscattered radiance in the range of 270-500 nm and the spectra are used to derive column NO_2 at a spatial resolution of 13 km×24 km at nadir (Levelt et al., 2006). The OMI overpass time is ∼13:30 local time.

We use the Berkeley High Resolution (BEHR) v3.0B OMI NO_2 retrieval (Laughner et al., 2018a). The air mass factor (AMF) is calculated based on the high spatial resolution a priori input data including surface reflectance, surface elevation and NO_2 vertical profiles. In this study we apply an experimental branch of the BEHR product which differs from v3.0B in several ways. First, instead of calculation based on temperature profiles from WRF-Chem, the tropopause pressure is switched to GEOS-5 monthly tropopause pressure which is consistent with NASA Standard Product (SP2) (Mak et al., 2018). Analysis shows the algorithm used in BEHR v3.0B to calculate the WRF-derived tropopause pressure is very much dependent on the vertical spacing predefined in WRF-Chem setup, which causes biases when the vertical layers are at a coarse resolution. Second, the NO_2 vertical profiles are outputs using the modified lightning parameterization described in Eq. 2.2.

2.3 Results

Comparison with observed lightning flash density

The lightning parameterizations are compared against observations from ENTLN in Fig 2.1. Each of the datasets is averaged from May 13 to June 23, 2012, covering DC3 field campaign. The ENTLN data is summed to the 12 km×12 km WRF grid. The G3/CTH parameterization fails to reproduce the spatial pattern of flashes observed by ENTLN over the CONUS. Compared to the G3/CTH, the KF/CTH parameterization improves the spatial correlation in the southeast region of US and yields a lower amount of lightning flashes. It

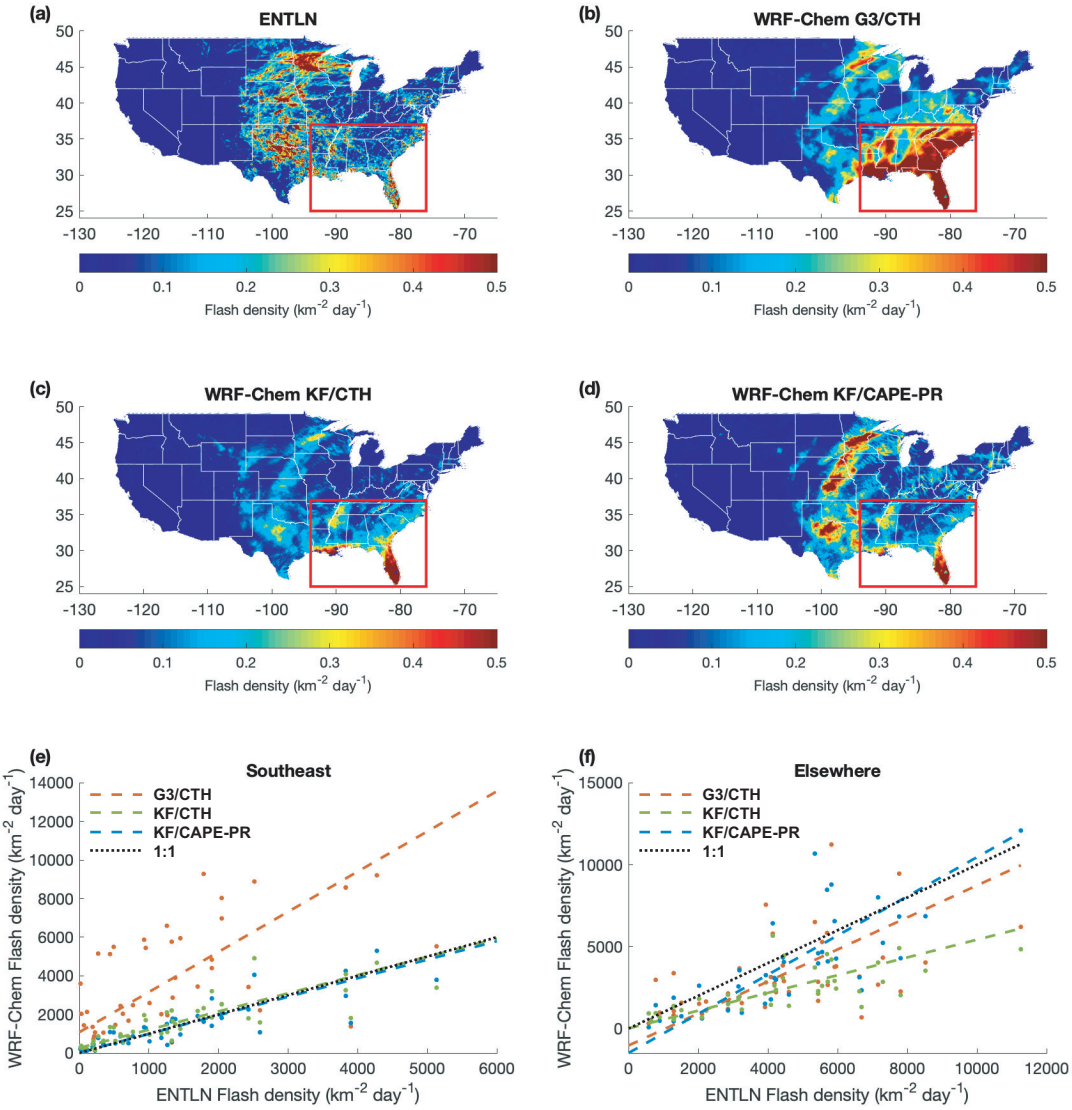

Figure 2.1: Observed flash densities from the ENTLN dataset **(a)** and WRF-Chem using three coupled convective-lightning parameterizations, the G3/CTH parameterization **(b)**, the KF/CTH parameterization **(c)** and the KF/CAPE-PR parameterization **(d)**, respectively. The correlation of total flash density per day between WRF-Chem outputs and ENTLN for the southeastern US (denoted by the red box in **a-d**) is shown in panel **(e)** and the correlation for elsewhere in CONUS is shown in **(f)**. The model using G3/CTH is in red, KF/CTH is in green, and KF/CAPE-PR is in blue. Dash lines are corresponding fits. For slope and R^2, see Table 2.1.

indicates that KF convective scheme produces smaller cumulus cloud top heights than G3 scheme by including entrainment and detrainment processes during the convection. The result is consistent with Zhao et al. (2009). The KF/CAPE-PR parameterization better captures the spatial distribution of flash densities both in the southeast region and elsewhere in CONUS. However the KF/CAPE-PR parameterization still fails to capture the gradients in flash occurrence within smaller regions. For instance, ENTLN shows that more lightning occurs along the east coast than west coast in Florida, however, WRF-Chem generates a lightning flash density of the same magnitude over both areas. Nevertheless, the KF/CAPE-PR substantially improves the model performance in reproducing lightning spatial patterns.

To evaluate the agreement quantitatively, we regress the WRF daily regional average flash densities against those measured by ENTLN. The daily regional averaged flash density is calculated by summing the total flash rates and dividing them by the corresponding regional size. The regressions are shown in Fig 2.1 (e) and (f); the correlation statistics are shown in Table 2.1. The regressions by forcing intercept equals to zero are also tested, and the results are unaffected.

Both models using the KF/CTH and KF/CAPE-PR parameterizations improve the correlation between modeled and observed lightning flash densities over the US domain. In the southeastern US, changing from G3 to KF convective scheme substantially increases the R^2 from 0.30 to 0.67 and reduces the slope from 2.08 to 0.94. Switching from CTH to CAPE-PR lightning parameterization only contributes a slight increment on the correlation. While the slopes close to unity both for KF/CTH and KF/CAPE-PR, we note that the improved scaling of the slope in KF/CAPE-PR is mainly caused by the scaling factor of 0.5 applied to the southeast region. In this simulation, a constant linear coefficient for CAPE-PR is not adequate to represent the observed lightning over CONUS, in contrast to the finding of Romps et al. (2014). Elsewhere in CONUS, both the changes in convective scheme and lightning parameterization yield a better representation of lightning flash densities compared to the observation. The R^2 for KF/CAPE-PR improves significantly to 0.62 compared to both G3/CTH and KF/CTH. The slope for KF/CAPE-PR is 1.19, which is within the uncertainty of the detection efficiency of ENTLN. In general the KF/CAPE-PR lightning parameterization captures the day-to-day variation in flash densities better than the G3/CTH and KF/CTH parameterizations as shown by the improved R^2 values.

Comparison with observed vertical profiles

We compare the WRF NO_2 profile to the average vertical profile of NO_2 measured during DC3 and SEAC4RS in Fig 2.2. Data points are matched in time and space by finding the WRF-Chem output nearest in time and closest in space to a given observation. We only compare NO_2 profiles from WRF-Chem using KF/CAPE-PR against the one using G3/CTH.

The effect of lightning NO_x on the profiles is indistinguishable close to the surface. In

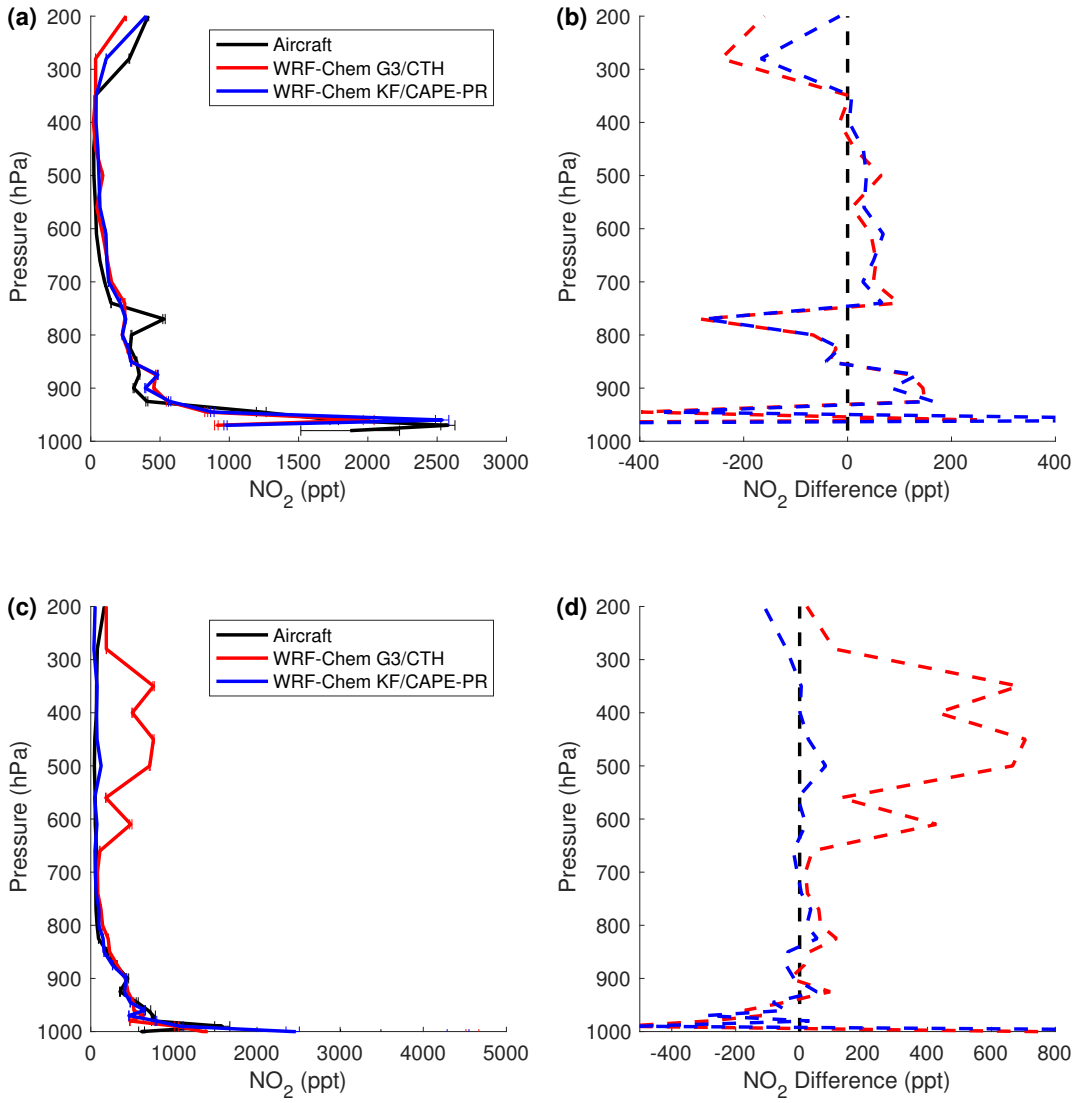

Figure 2.2: Comparison of WRF-Chem and aircraft NO_2 profiles from the **(a,b)** DC3, **(c,d)** SEAC4RS campaigns. Vertical NO_2 profiles are shown in **(a,c)**, the solid line is the mean of all profiles and the bars are 1 standard deviation for each binned level. The corresponding absolute difference compared to observations are shown in **(b,d)**. Aircraft measurements are shown in black, WRF-Chem using G3/CTH parameterization in red and WRF-Chem using KF/CAPE-PR parameterization in blue.

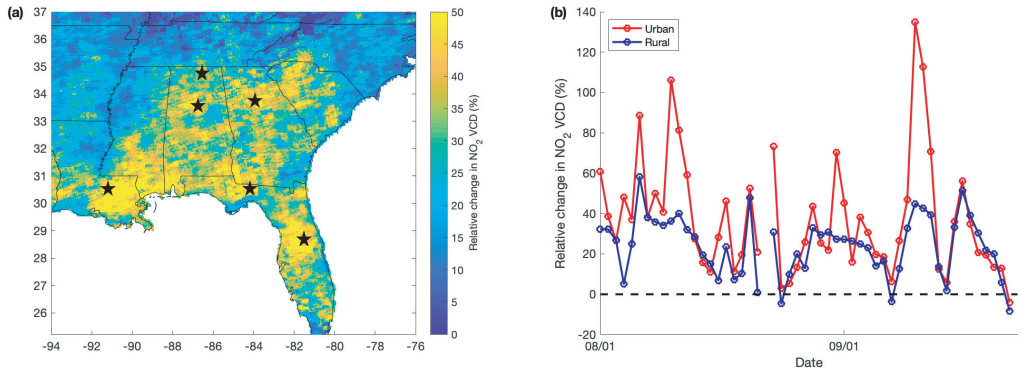

Figure 2.3: Relative change in BEHR NO_2 VCD over the southeastern US switching the source of a prior NO_2 profiles from WRF-chem outputs using G3/CTH to one using KF/CAPE-PR lightning parameterization. **(a)** shows the mean spatial distribution of the changes from Aug 01 to Sep 23, 2013 and **(b)** shows the temporal variation over urban and rural areas. Only observations with cloud fraction less than 20% are included. Medium to large cities, including Atlanta, GA; Huntsville, AL; Birmingham, AL; Tallahassee, FL; Orlando, FL; and Baton Rouge, LA, are marked by stars in panel **(a)**.

		AMF G3/CTH	AMF KF/CAPE-PR	%ΔAMF	VCD G3/CTH	VCD KF/CAPE-PR	%ΔVCD
Sep 10	Urban	1.64	0.72	-56.0	2.19×10^{15}	5.16×10^{15}	134.9
	Rural	1.96	1.33	-32.0	1.11×10^{15}	1.63×10^{15}	44.9
Aug 24	Urban	1.07	0.95	-11.3	2.56×10^{15}	2.64×10^{15}	3.1
	Rural	1.23	1.25	1.60	1.91×10^{15}	1.82×10^{15}	-4.6

Table 2.2: Differences for BEHR AMFs and tropospheric VCDs when using the a priori NO_2 profiles from models with CTH vs CAPE-PR parameterizations in the AMF calculation. For definitions of "urban" and "rural", see the text.

the upper and middle troposphere, both model simulations yields similar NO_2 vertical profiles compared to the measurements from DC3. WRF-Chem using KF/CAPE-PR performs slightly better between 200 hPa to 400 hPa but the negative bias still exists. NO_x from both the observations and the models are very small in the middle troposphere between 400 hPa to 700 hPa.

Laughner et al. (2019) previously identified a high bias of WRF-Chem UT NO_2 versus SEAC4RS in the southeast US when using the G3/CTH parameterization. The model using the KF/CAPE-PR parameterization reduces this high bias of NO_2 in the middle and upper troposphere. The KF/CAPE-PR parameterization slightly overestimates NO_2 in the middle troposphere (400 - 530 hPa) and underestimates it in the upper troposphere ($<$ 280 hPa), which is consistent with the comparison to observations from DC3 campaign.

Impact on BEHR NO_2 retrievals

In space-based retrievals of NO_2, the AMF is required to convert the slant column density (SCD) obtained by fitting the observed radiances into a vertical column density (VCD). The AMF depends on scattering weights (which describe the sensitivity of the measurement to different levels of the atmosphere) and an NO_2 profile which is either measured or simulated by a chemical transport model, such as WRF-chem. Over a dark surface, the scattering weights in the UT are up to 10x greater than near the surface, due to the greater probability that a photon that reaches the lower troposphere will be absorbed by the surface. Therefore, errors in the UT NO_2 profile can have large effects on the AMF (e.g. Laughner and Cohen, 2017). Here, we investigate how the NO_2 profiles simulated by the KF/CAPE-PR parameterization affect the BEHR NO_2 retrievals.

Fig. 2.3(a) shows the relative change in tropospheric VCD averaged between Aug 01 to Sep 23, 2013 induced by changing the a priori profiles from the model using G3/CTH to the one using the KF/CAPE-PR lightning parameterization. The relative enhancement of VCD is 19% on average over southeast US but it varies significantly.

We follow the same algorithm used in Laughner and Cohen (2017) to determine if the result is significant. The overall uncertainty due to AMF calculation for BEHR v3.0B is smaller than 30% during the study period (Sec 6 in supplementary from Laughner et al. (2019)). Over 90% of the uncertainty attributes to the a prior NO_2 profiles, the tropopause and cloud pressures. As each grid in Fig. 2.3(a) is the average of 45±9 pixels, the reduced uncertainty is less than 4.5%. The overall change in VCD is four times larger than the reduced uncertainty. The switch of lightning parameterization leads to changes in VCD exceeding the averaged uncertainty in ˜94% of pixels in the southeast region of US.

The spatial pattern in Fig. 2.3(a) suggests that the magnitude of the improved representation of lightning is quite different in urban and rural areas. The cities indicated by stars and their vicinity regions are associated with substantial increase in NO_2 VCD. To quantify this, we define urban and rural areas by difference in column NO_2 calculated from WRF-Chem without LNO_x. Urban ares are the top 5% of columns with the average VCD of 2.2 $\times 10^{15}$ mole cm^{-2}. The selected rural areas have the same size as urban areas and the average VCD is 0.72×10^{15} mole cm^{-2}. Fig 2.3(b) shows the relative change in VCD over the urban and rural areas as a function of time. The increase in VCD due to the change in profiles is more pronounced over urban areas with averaged relative change of ˜38% compared to the average change of ˜24% in rural areas. Changes in urban VCDs span -10% to 135%. In contrast, using the NO_2 profiles produced by the KF/CAPE-PR simulation leads to only maximum 58.3% increase in VCD over rural areas.

Table 2.2 presents the AMF and VCD obtained from using a priori profiles with G3/CTH or KF/CAPE-PR lightning parameterizations as well as the relative changes on Sep 10 and Aug 24, 2013. The corresponding a priori NO_2 profiles and scattering weights over urban

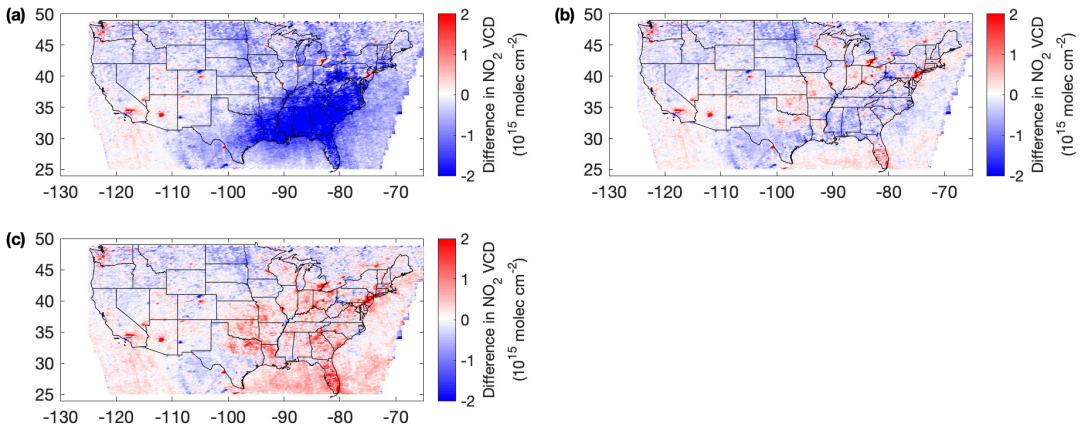

Figure 2.4: Difference in NO_2 VCD between BEHR retrievals and WRF-Chem ("WRF-Chem" − "BEHR"). **(a)** excludes LNO_x in model simulation, **(b)** adds LNO_x emission with production rate of 500 mol NO $flash^{-1}$. **(c)** includes the same LNO_x emission as **(b)** but uses NO_2 profiles scaled upward by 60% at pressure lower than 400 hPa. The average time covers May 13 to June 23, 2012. Pixels with cloud fraction larger than 0.2 are filtered out in the analysis.

and rural areas are shown in Fig. A.3. Sep 10 is an example of one day when the change in NO_2 profiles has a very large impact on the NO_2 VCDs. The WRF-Chem using G3/CTH parameterization places a large amount of NO_2 between 200-600 hPa with the maximum value comparable to the near surface NO_2 over the urban areas. The calculated AMF is predominantly determined by lightning NO_2 due to the combination of higher scattering weight and larger NO_2 in the middle and upper troposphere. The change in AMF is -56.0% over urban areas and -32.0% over rural areas; the corresponding VCD increases by 134.9% and 44.9%, respectively. In contrast, Aug 24 is an example where the lightning parameterization has very little effect. While the positive bias in NO_2 aloft is also observed by using G3/CTH parameterization, the amount of NO_2 in the middle and upper troposphere is smaller than Sep 10. It leads to lower sensitivity in AMF to the erroneous NO_2 caused by the lightning parameterization. With smaller relative change in AMF, the relative change in VCD is 3.1% over urban areas and -4.6% over rural areas.

2.4 Discussion

Here, we apply the improved KF/CAPE-PR simulation to the problem of constraining LNO_x production over CONUS. To do so, we vary the lightning NO_x production rate prescribed in WRF-Chem to produce the simulated map of NO_2 VCD, and compare against OMI NO_2 retrievals using a priori profiles from model simulations with the same LNO_x production rate. In our model-satellite comparisons the averaging kernel is applied to remove the representa-

tive errors introduced by a priori knowledges of NO_2 vertical profiles (Boersma et al., 2016). Figure 2.4 shows the difference between satellite retrieved NO_2 VCD and model simulated NO_2 VCD without lightning NO_x **(a)** and with lightning NO_x production rate of 500 mol NO $flash^{-1}$ **(b)** averaged between May 13 to June 23, 2012. Figure A.4 shows difference plots with varied lightning NO_x production rates (400 and 665 mol NO $flash^{-1}$). The corresponding root-mean-square errors (RMSE) are included in Table A.1. LNO_x production rate of 500 mol NO $flash^{-1}$ yields the lowest RMSE of 0.41×10^{15} mole cm^{-2} between modeled and observed NO_2 VCD over CONUS. This is at the high end of previous estimates of the lightning NO_x production rate (16-700 mol NO $flash^{-1}$).

The RMSE for urban areas (top 5% of NO_2 VCD simulated by WRF-Chem without LNO_x) remains at high value (˜0.9-1.3$\times10^{15}$ mole cm^{-2}) when switching the LNO_x production rate. It indicates that the bias in the modeled VCD over urban areas is more likely due to surface NO_2. The RMSE for non-urban areas shows pronounced change with varied LNO_x production rate. Excluding urban areas lowers the RMSE to 0.37×10^{15} mole cm^{-2} for LNO_x production rate of 500 mol NO $flash^{-1}$. The RMSEs are significant considering the uncertainty for retrievals. During the average time period, 32 $\pm$ 6 pixels contribute to each value in the plots. While the global mean uncertainty for tropospheric NO_2 VCD retrievals is 1×10^{15} mole cm^{-2} (Bucsela et al., 2013), the reduced uncertainty in our analysis is ˜0.2×10^{15} mole cm^{-2}. The calculated RMSEs are twice of the uncertainty.

However, we note that this lightning NO_x estimate is systematically biased high due to the negative bias in $[NO_2]/[NO_x]$ ratio in the middle and upper troposphere. The satellite observed NO_2 column serves as a proxy for total NO_x emitted by lightning. The rapid interconversion between NO and NO_2 reaches the photochemical steady state in a short time (˜120s). Consequently, if the model kinetics result in an incorrect NO-NO_2 photochemical steady state ratio, this error will propagate into the LNO_x production estimate. Comparisons against aircraft measurements show $[NO_2]/[NO_x]$ ratio in the WRF-Chem simulations is around 40% smaller than observations in upper troposphere (Fig. A.5). Given that the simulated $[NO_2]/[NO_x]$ is too small, the model will simulate smaller NO_2 VCDs per unit of LNO_x emitted, requiring a greater LNO_x production efficiency to match satellite NO_2 VCD observations. Comparison of modeled NO_2 columns recalculated with NO_2 profiles scaled up by 60% (the ratio of observed and modeled $[NO_2]/[NO_x]$) at pressure levels where $p < 400$ hPa and observations is shown in Fig. 2.4 **(c)**. This suggests that the 500 mol NO $flash^{-1}$ is greater than the actual LNO_x production rate when the bias caused by $[NO_2]/[NO_x]$ ratio is accounted for.

Several recent studies also report an underestimate in modeled $[NO_2]/[NO_x]$ ratios in SE US(Travis et al., 2016; Silvern et al., 2018); both feature observations from SEAC4RS field campaign to validate model simulations. Silvern et al. (2018) suggests the underestimate is either caused by an unknown labile NO_x reservoir species or error in reaction rate constant for the NO+O_3 reaction and NO_2 photolysis reaction. In contrast, Nault et al.

(2017) utilizes measurements from DC3 field campaign and demonstrates a positive bias in modeled $[NO_2]/[NO_x]$ ratio compared against observations. Understanding the difference in $[NO_2]/[NO_x]$ between model and observations requires additional study, but is crucial to reducing the uncertainty in LNO_x estimates.

2.5 Conclusions

We implement an alternative lightning parameterization based on convective available potential energy and precipitation rate into WRF-Chem and couple it with Kain Frisch convective scheme. We first validate it by comparing against lightning observations and find that the switch of convective scheme reproduces day-to-day variation of lightning flashes in the southeastern US and the switch of lightning parameterization contributes to the improvement on lightning representation elsewhere in the US. We also compare the simulated NO_2 profiles against aircraft measurements and find that the simulated NO_2 using KF/CAPE-PR is more consistent with observations in the mid and upper troposphere.

The improved lightning NO_2 simulation has significant impact on AMFs and VCD of NO_2. Over the southeastern US the AMF is reduced by 16% on average leading to a 19% increase in the NO_2 VCD. The effects on AMF and on VCD are very locally dependent. The VCD increase over urban areas is more pronounced and can be up to over 100%. This study emphasizes the importance of including reliable lightning NO_2 in a priori profiles for satellite retrievals. The model-satellite NO_2 column comparison suggests 500 mol NO $flash^{-1}$ is the upper bound for the estimate of lightning NO_x production rate.

Code and data availability

The experimental branch of BEHR v3.0B product used in this study is hosted by UC Dash (Zhu et al., 2019a; Zhu et al., 2019b) as well as on `behr.cchem.berkeley.edu`. The BEHR algorithm is available at `https://github.com/CohenBerkeleyLab/BEHR-core/` (Laughner and Zhu, 2018). The revised WRF-Chem code is available at `https://github.com/CohenBerkeleyLab/WRF-Chem-R2SMH/tree/lightning` (Zhu and Laughner, 2019).

Chapter 3

Combining machine learning and satellite observations to predict spatial and temporal variation of near surface OH in North American cities

The chapter was adapted from: Q. Zhu, J. L. Laughner, and R. C. Cohen (2022a). "Combining Machine Learning and Satellite Observations to Predict Spatial and Temporal Variation of near Surface OH in North American Cities". *Environmental Science & Technology*

3.1 Introduction

The hydroxyl radical (OH) is the most influential oxidant in the daytime tropospheric chemistry (Levy, 1971). On a global scale it determines the lifetime of greenhouse gases such as methane (CH_4), therefore regulates their impacts on radiative forcing. Over urban areas, it reacts with local pollutants such as CO, NO_x and volatile organic compounds (VOCs), leading to the formation of ozone (O_3) and secondary organic aerosols (SOA). Ozone near the surface triggers negative impacts on human health with exposure increasing the risk of respiratory diseases (Jerrett et al., 2009; Anenberg et al., 2010). SOA is a major component of particulate matter (PM) and is associated with adverse respiratory and cardiovascular health outcomes (Mauderly and Chow, 2008). PM and ozone are the most prominent known causes of early deaths among pollutants and result in more than 90% of total air-pollution-related mortalities (Dedoussi et al., 2020).

Given the vital role of OH in photochemistry, OH observations are notably sparse. The short lifetime (<1s) and low concentration make direct observations challenging (Eisele et al., 1997; Brune et al., 1998; Stone et al., 2012). The high spatial heterogeneity restricts our

ability to generalize from in-situ OH measurements. A global or hemispheric average OH can be inferred from the uniformly distributed species whose production is well constrained and the dominant sink pathway is the reaction with OH. Atmospheric methyl chloroform (CH_3CCl_3) has been used extensively to constrain the annual or decadal OH variability (Lovelock, 1977; Singh, 1977; Montzka et al., 2000). zhang18 utilized an inverse modeling system to constrain global mean OH using the CH_4 satellite observations and its emissions inventories. These studies contribute to an enriched global annual record of OH, however, they provide little mechanistic insight into the controls over OH at urban scales. Wolfe et al. (2019) showed that a linear relationship between formaldehyde (HCHO) and OH exists in the remote atmosphere, and then mapped the OH column using the synthesis of airborne and satellite HCHO observations. Wolfe et al. (2019) provides an estimate of the OH column with global coverage and at much finer spatial scales than was previously available. By incorporating daily HCHO column measurements it also enables OH predictions with daily time resolution.

Compared to the remote atmosphere, in cities, wide variations in NO_x and much more complex VOC chemistry affect OH, requiring a more varied set of parameters to describe OH. The basic chemistry is as follows. Ozone photolysis to yield $O(^1D)$ which then reacts with H_2O is a typical initiator of OH formation. OH then oxidizes VOCs and CO to initiate the HO_x cycling. It is the wide range and high abundance of VOCs that make urban chemistry distinctly different from the remote atmosphere where CH_4 and CO chemistry dominates. OH reacts with VOCs to form organic peroxy radicals (RO_2) and reacts with CO to form the hydroperoxy radical (HO_2). In the presence of NO_x, RO_2 reacts with NO to yield HO_2. HO_2 will then react with NO, reforming OH. NO_x serves as a catalyst to fuel the HO_x cycle. The HO_x cycle is terminated by the formation of HNO_3 from the reaction of OH with NO_2, the formation of alkyl nitrates ($RONO_2$) from RO_2 reacting with NO (Perring et al., 2013), as well as the RO_2 and HO_2 reactions that form stable products such as hydroperoxides (ROOH and HOOH).

Characterizing trends in OH on annual time scales will be especially important for understanding urban chemistry. Laughner and Cohen (Laughner and Cohen, 2019a) show that trends in urban NO_x chemistry can be inferred at the length scale of urban plumes. Their research infers trends in the NO_x lifetime from the trend in the shape of NO_2 plumes as observed from space. That method offers the potential to estimate trends in the plume-average OH concentrations, however, the direct mapping to OH is hampered by the unknown chemical parameters such as the partitioning of loss NO_x between alkyl nitrates and nitric acid as well as competition of VOC for OH.

There also have been a number of efforts to generalize this chemistry and find simple relationships that describe urban OH variability over space and time. For example, Rohrer and Berresheim (2006) presented four years of in-situ OH measurements from 1999 and 2003 at a suburban site located in southern Germany. They found a surprisingly strong correlation

between $J(O^1D)$ and OH. The authors attributed the presence of a simple linear correlation in what is well known to be a highly non-linear system to be the result of compensating effects in the controls over OH. Similar correlations have been reported for OH measurements at several other locations (Ren et al., 2003; Griffith et al., 2016; Sanchez et al., 2018), although for those sites the temporal extent of the observations is weeks rather than the 4 years described by Rohrer and Berresheim (2006). We note, however, that the slope of the reported linear correlation of OH with $J(O^1D)$ shows a wide spread over urban areas as summarized in Table B.1. $J(O^1D)$ alone is not enough to interpret the OH variability across multiple urban environments.

3-D chemical transport models represent a comprehensive approach to describe the combined effects of emissions, transport and chemical reactions on OH. The models represent effects of variability and trends in emissions and climate and can therefore describe variability and trends in OH over time. The chemical mechanisms in current models, such as RACM/RACM2, have been applied to investigate OH chemistry under polluted conditions in atmospheric models featuring various dimensions, ranging from zero-dimensional chemical box model to three-dimensional chemical transport models like WRF-Chem. These numerous studies demonstrate that the largest source of biases in OH simulations in cities is attributed to the representation of NO_x and VOC concentrations (Ren et al., 2003; Shirley et al., 2006; Kanaya et al., 2007; Dusanter et al., 2009; Mao et al., 2010; Stone et al., 2012; Griffith et al., 2016).

Given the limited success of purely observational approaches and the inconsistent representation of VOC and NO_x concentrations in models, a method for evaluating OH variability and trends that combines the advantages of both approaches is desirable. One method is data assimilation. It optimizes the model simulations by propagating observational information in time and space, from a limited number of observed species to a wide range of chemical components (Sun et al., 2020). A series of studies have demonstrated the capability of data assimilation techniques for improving chemical weather forecasts (Eibern and Schmidt, 1999; Elbern and Schmidt, 2001; Vira and Sofiev, 2012; Miyazaki et al., 2017) including a recent analysis showing how observations of chemicals can lead to improved predictions of winds(Liu et al., 2021). However, data assimilation is computationally intensive and is most effective where there are large data volumes(Migliorini et al., 2008; Jiang et al., 2015; Mizzi et al., 2016).

To develop an observationally constrained model of OH at lower computation expense, we explore use of machine learning (ML). We use the ML first to simplify representation of the chemical weather model and to replace parameters from the chemical weather model with observations. We describe evolutional variability and trends analysis of modeled OH chemistry in 49 North American cities as computed in a state-of-the-art chemical transport model (CTM), and seek a set of parameters that are capable of explaining the OH variability across all of the cities. Our methods are described in Sect.2. The ML model is shown to

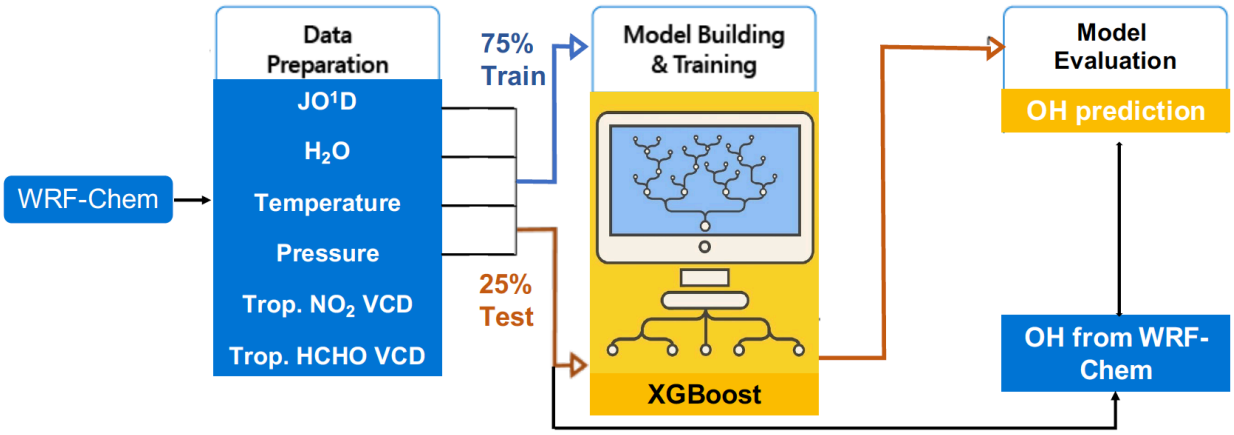

Figure 3.1: Schematic representation of our machine learning workflow.

capture the full range of urban OH variability in this CTM. We evaluate the accuracy of the ML model first by comparing predictions of the ML OH to CTM calculations of OH that were not part of the training data (Sect.3). We then utilize this ML model with observational inputs emphasizing satellite remote sensing observations to predict near surface OH. We evaluate the ML model predictions against independent observations that are sensitive to OH, such as the observed concentration of isoprene (Sect.4). We finish by applying this method to calculate trends in OH in 49 North American cities. We conclude with a discussion of opportunities to improve this ML model using other data sets such as isoprene column retrievals.

3.2 Methods: model and observations

A supervised learning ML system requires input data for various purposes. Training data sets are those the ML model use to learn. Test data sets are commonly from the same source as the training data sets but are entirely independent of the training data sets. Test data sets are used to evaluate the statistical performance of the ML model. In our study, both training and test data sets are collected from WRF-Chem simulation (Sect.2.1.1) and are processed to prepare feature sets suitable for ML inputs (Sect.2.1.2). The workflow of building our ML model is shown in Figure 3.1.

Once the ML model is built, it offers considerable flexibility for incorporation of observations to estimate near surface OH. To this end, we make use of the satellite observations described in Sect.2.1.3.

In addition to the data being fed into the ML system for OH prediction, we also collect other data sets used for validation, to be more specific, in-situ isoprene measurements discussed in Sect.2.1.4.

Input data

WRF-Chem simulations

WRF-Chem is used to simulate OH chemistry over North America. The simulations are described in more detail in Laughner et al. (2018b). Briefly, the model years included are 2005, 2007-2009 and 2011-2014. The model is configured at the spatial resolution of 12 km $\times$ 12 km with 29 hybrid vertical pressure levels. The North American Regional Reanalysis (NARR) defines the meteorological initial and boundary conditions, from which water vapor, temperature and winds are nudged every three hours. The chemical initial and boundary conditions use the Model for Ozone and Related Chemical Tracers (MOZART) (Emmons et al., 2010).

A priori knowledge of emissions is collected from various sources. Biogenic emissions are driven by the Model of Emissions of Gases and Aerosols from Nature (MEGAN v2.1, Guenther et al. (2006)), and anthropogenic emissions utilize the National Emissions Inventory 2011 (NEI 11). To account for the interannual variation in anthropogenic emissions, we apply a scaling factor to the NEI emission so that the annual emissions are matched to those reported by EPA at each model year (EPA, 2016). The lightning NO_x emission is described in Laughner and Cohen (2017). The lightning flash counts are parameterized using the cloud top height (Price and Rind, 1992) and we assume a 500 mol NO generated per flash. The soil NO_x is simulated using the Yienger and Levy model(Yienger and Levy, 1995). The biomass burning emission is inactive. We used RACM2_Berkeley (Zare et al., 2018) as the chemical mechanism. This mechanism is based on RACM2 (Goliff et al., 2013) but incorporates a more detailed organic nitrate chemistry. Zare et al. (2018) demonstrated this mechanism agrees well with observations of $RONO_2$ and their lifetime.

WRF-Chem data preparation for ML input

Preparing the WRF-Chem data for the ML requires two steps. First, we select which model variables ("features" in ML parlance) to use as input parameters for the ML. Second, we must pre-process the model output into an acceptable format for the ML package that also mimics real observations.

We use multiple criteria to select ML features. First, even though the ML model is purely data-driven, we select the features based on our understanding of urban OH chemistry and ensure that the features show explicit linkage to near surface OH. Second, we choose features for which there either exist long-term observations covering the study domain or can be quickly calculated using an atmospheric model constrained with observations. This ensures that we will be able to use the ML along with observations (instead of WRF-Chem output) to describe OH. For instance, even though near surface NO_x is expected to have a strong association with the near surface OH concentration, we use the tropospheric NO_2 column as a proxy since the column can be observed from space and the space-based measurements

offer a multi-decadal record with global coverage. Third and finally, we keep the feature list as simple as possible while maintaining good model performance. Many features were explored, we only retain features that meet the long-term availability criteria and that result in notable improvement on model performance.

Six features fulfilled the criteria described above, including four near surface variables ($J(O^1D)$, H_2O, T, P) and two tropospheric column variables (NO_2 column and HCHO column). The near surface variables are calculated using the average of the bottom five layers in WRF-Chem, which corresponds to ∼350 m above ground level. $J(O^1D)$ represents the photolysis of ozone with the product O^1D. In combination with H_2O it determines the production of OH and initiation of the HO_x cycle via the reaction of O^1D with H_2O. Temperature and pressure define the geophysical condition and affect the chemical kinetics. The two column variables are calculated using model simulated vertical profiles weighted by the averaging kernels from the corresponding satellite products summarized in Sect.2.1.3. Weighting by the averaging kernel simulates the column that would be observed from a satellite given the modeled vertical profile. The tropospheric NO_2 column represents the NO_2 integrated from the surface to the tropopause with an nonuniform vertical sensitivity. Previous studies have inferred the ground level NO_2 from the NO_2 column with a good level of agreement (Kharol et al., 2015; Bechle et al., 2013; Lamsal et al., 2008), confirming that the column NO_2 has adequate surface sensitivity to assess the role of NO_2 in near surface OH. The second column variable is the tropospheric HCHO. HCHO is an indicator of VOC oxidation as it is a product of many reactions of VOC with OH, moreover, it is an important entry point into the HO_x catalytic cycle as it has a short lifetime to photolysis and reaction with OH. Specifically, HCHO is a key oxidation intermediate from OH reactions with isoprene. Valin et al. (2016) describes the relationship between the HCHO column and near surface OH and found that it offers the potential to illustrate the variability of OH production rate.

To explore near surface OH chemistry over urban areas, we select the grids from WRF-Chem covering 49 North American cities and their surrounding areas to sample a variety of urban environments. The list of 49 cities is in line with Russell et al. (2012) and Laughner and Cohen (Laughner and Cohen, 2019a). We use the methodology in Laughner and Cohen (Laughner and Cohen, 2019a) to define boundaries of cities and select radii between 0.5 and 1.0 deg to capture each city's plume without encountering plumes from other sources (Table B.3). In each simulation year, we pick the daily WRF-Chem outputs whose time is closest to the satellite overpass time (∼13:30 LT) during April to September. The choice of temporal constraint facilitates the synthesis of satellite observations. We omit days with simulated lightning(Zhu et al., 2019c) or cloud fraction larger than 20%. Lightning emits NO_x in the upper troposphere and leads to the enhancement in NO_2 column, but it is not associated with near surface OH chemical conditions. Cloudy days affect the photochemical conditions via photolysis frequency. A large uncertainty remains in simulating clouds within the chemical transport model (Hong et al., 2004), thus we confine the study to clear sky conditions. We

treat each 12km×12km grid from WRF-Chem as an independent observation, and this data set is 5.5 million observations in total. Out of those observations, we randomly picked 75% of the observations as the training data and put aside the rest of data separately for evaluation.

Satellite data

Satellite observations can be applied to our ML model to enable estimate of near surface OH. The resulting OH predictions are then not emulating the WRF-Chem simulated OH but reflect the ambient OH in the urban environments.

Among the six features, we take $J(O^1D)$, H_2O, temperature and pressure from the model outputs. $J(O^1D)$ in WRF-Chem is calculated using Fast-J photolysis scheme. Since the WRF-Chem is constrained by the NARR meteorological fields with nudging every three hours, we expect the latter three parameters are in a good agreement with the observations. The two column features can be observed from the space, here we use OMI satellite observations to obtain both tropospheric NO_2 column and HCHO column features. The result is an ML prediction of OH that is largely based on observed parameters.

The Ozone Monitoring Instrument (OMI) is a nadir-viewing spectrometer aboard NASA Aura spacecraft. Launched in 2004, OMI measures the back-scattered solar irradiance at ∼13:30 local time at the spatial resolution of 13×24 km^2 at nadir. Absorption signals in the recorded spectra provide slant column density (SCD) of various trace gases including NO_2 and HCHO. To produce tropospheric vertical column densities (VCD), the stratospheric column is subtracted (Boersma et al., 2011; Bucsela et al., 2013) and an air mass factor (AMF) is calculated to convert SCD to VCD(Palmer et al., 2001).

For the tropospheric NO_2 column, we use Version 3.0B of the Berkeley High Resolution (BEHR) OMI NO_2 product (Laughner et al., 2018b). It builds upon the the NASA standard product v3.0; the major changes are the calculation of tropospheric AMFs using high-resolution a priori input data for surface reflectance, surface elevation and NO_2 vertical profiles. The daily NO_2 profiles are simulated from WRF-Chem whose configuration is the same as the one described in Sect.2.1.1, and are used to capture the day to day variation. Laughner et al. (2019) evaluated the BEHR NO_2 products over North America and concluded that the uncertainty during summertime is ∼30%.

We use tropospheric HCHO column densities from the Quality Assurance For Essential Climate Variables (QA4ECV) project (Lorente et al., 2017) (`www.qa4ecv.eu`). HCHO profiles from the TM5 model on a 1°x1° latitude-longitude grid are used as a priori in AMF calculation (Nightingale et al., 2018). Lorente et al. (2017) discussed the structural uncertainty in the retrieval products from QA4ECV project and they concluded 31%-42% uncertainty resulting from AMF calculation in their NO_2 product. We assume that the uncertainty of the HCHO product is similar. To be more conservative, we estimate the uncertainty in HCHO column to be 60%, the upper limit reported in previous studies across different

HCHO retrieval products (De Smedt et al., 2012; Barkley et al., 2012).

The satellite retrievals are matched in time and space to the WRF-Chem output. We collect the column observations between 2005 and 2014. To reconcile the difference in the spatial resolution, both NO_2 column and HCHO column are re-gridded to the WRF-Chem native spatial resolution. We find that the ranges of HCHO column and NO_2 column from WRF-Chem simulations cover those from satellite observations (Fig. B.1), which demonstrates that the NO_2 and HCHO columns from WRF-Chem are sufficiently representative of real atmospheric composition.

Isoprene data for validation

We also use ground measurements of isoprene from Photochemical Assessment Monitoring Station (PAMS) sites for validation. The measurements are available from the EPA Air Quality System (AQS) database (https://www.epa.gov/outdoor-air-quality-data). We include sites where hourly isoprene and temperature measurements are available. The isoprene measurements are matched to our OH predictions both in time and space, therefore the ground measurements are restricted to 1pm to 2pm local hour between 2005 and 2014. Four sites featuring more than 100 observations are available and we denote them by the city names the sites are closest to, including Fort Worth, Dallas, Washington DC and Baltimore, respectively.

ML configuration

ML selection and design

Our choice of the ML technique is the gradient boosted tree implemented from XGBoost (Chen and Guestrin, 2016). The choice is based on three factors. First, it outperforms linear regression and its variants as it accounts for the non-linearity of urban OH chemistry. Second, it is optimized to run on distributed computing environments and can handle a large volume of input data. Third, compared to a neural network, the results of the gradient boosted tree model are more interpretable, making it possible to connect the results to identifiable chemical characteristics of the system. We note, also, that XGBoost library has gained popularity in atmospheric science community; it has been applied, for instance, to correct the bias between model and observations of ozone (Ivatt and Evans, 2020; Keller et al., 2021). The design of the gradient-boosted tree model used in this study is shown in Appendix B.1.

ML training and feature sets

We train a single ML model on all of the urban WRF-Chem data and denote it as "General" system. We then use two distinct OH prediction sets, differentiated by what input data is given when asked to predict near surface OH. We focus attention on parameters that are

observable so that the WRF output can be swapped with observations to yield a combined model-observation synthesis for estimating OH. As mentioned earlier, we use space-based observations for NO_2 and HCHO because global, long-term records are available from satellite instruments including GOME, GOME-2, OMI and TROPOMI. This makes our ML approach more generally applicable than if it relied on surface observations, which are not available for all cities, especially in developing countries. However, adopting other satellite retrieval products requires retraining the ML with model columns weighted by the averaging kernels consistent with the satellite products.

The "General-WRF" OH predictions are produced using the "General" ML model and the input features from WRF-Chem, including NO_2 and HCHO columns.

The "General-Satellite" OH predictions use the same ML model with the NO_2 and HCHO columns observations from OMI instead of modeled quantities.

In addition, we train a separate ML model for each of the 49 cities identified in Sect.2.1.2. The discussion of OH predictions from these city-specialized ML models are in Appendix B.4 and B.5.

3.3 Validation of OH prediction using WRF-based features ("General-WRF")

Our first step is to assess the ML performance in the General-WRF case. We check the correlation of predicted OH against the true WRF-Chem OH, including a test of how each of the six selected input features improve the prediction.

Two metrics are applied to assess the model performance. We use the correlation coefficient (R^2) to measure how much of the OH variability is explained by the model prediction and the root-mean squared error (RMSE) to measure the standard deviation of the residuals and describe the bias/error in the prediction.

We first investigate the effect of individual features on the model performance. The model is benchmarked by adding the features iteratively. Starting with a single parameter, we add a new feature in each iteration and calculate the overall improvement of the model performance. Figure 3.2(a) is a demonstration of the effectiveness of selected features. A model trained on $J(O^1D)$ and water vapor only explains 13% of the OH variability. Two column variables, the NO_2 column and the HCHO column, provide the most important constraints on the OH abundance. Introducing these two column variables increases the R^2 to 42% and 70%, respectively. The corresponding RMSE declines from 4×10^6 molec cm^{-3} to 2.37×10^6 molec cm^{-3}. The final model incorporates near surface temperature and pressure, leading to an increase in R^2 from 70% to 76%. We tested changing the order of

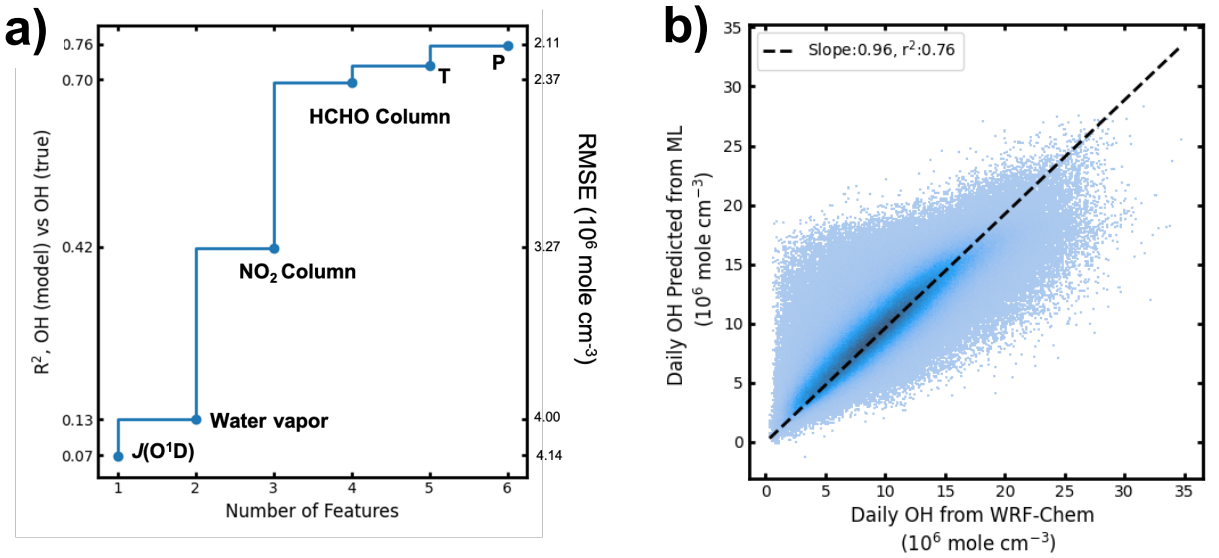

Figure 3.2: Evaluation of the ML model performance. a) shows the increases of R^2 and the corresponding decrease of RMSE with respect to incremental feature selection. b) shows the comparison of OH predicted from ML against OH from WRF-Chem. Darker color corresponds to higher data density. A linear regression is denoted by the dashed line.

the parameters and found no significant effect on the performance of the model.

The performance of the model is shown in Figure 3.2(b). A linear regression comparing the ML OH predictions versus WRF-Chem OH yields a slope of 0.98. We find a mean bias of 4×10^3 molec cm^{-3}, which demonstrates that there is no systematic bias in the predictions. The RMSE is 2.11×10^6 molec cm^{-3}. While there is a considerable spread, 72% of the predictions yield an agreement with the truth OH with the relative difference of less than 20%. We also probe the model performance for each city separately. This general model yields an R^2 above 50% for 44 out of 49 cities. The remaining five cites are located in the southeast US with high lightning frequency. We believe the small training data size is the main cause of relatively poor ML model performance over these regions (Fig. B.2).

Note that the ML model is trained on the features acquired from WRF-Chem, it underlines the premise that no uncertainty is introduced in feature sets. However, constructing features from observations requires the consideration of non-negligible uncertainty embedded in the observations. It is unknown how the uncertainties from features propagate through the model configuration and affect the OH prediction. We conduct a detailed uncertainty analysis(Appendix B.3). Given that the uncertainty in BEHR NO_2 columns is 30% and the uncertainty in QA4ECV HCHO column is 60%, those uncertainties propagate through the model configuration and result in a model performance quantified by the RMSE of 3.2×10^6

molec cm^{-3}.

3.4 Validation of OH predictions using satellite-based features ("General-Satellite")

In this section, OH is predicted using our ML model and the feature set which incorporates the modeled parameters and satellite observations for two column parameters. While the near surface OH measurements across the target urban regions are extremely limited, we seek for implicit approaches to validate our predicted near surface OH.

The anticorrelation with isoprene

We compared ML OH predicted using satellite-based features to isoprene observations in four urban sites, and confirm that ML-predicted OH is anticorrelated with isoprene. Isoprene is assumed to be at steady state (Eqn.3.1) due to its short lifetime respect to OH ($<$ 1 hr) (Murphy et al., 2006). The source of isoprene (E) is assumed independent of OH and the sink of isoprene is predominantly OH oxidation. Hence isoprene serves as a probe of local OH abundance as higher OH results in a lower isoprene concentration. This inverse relationship between OH and isoprene demonstrates that our ML OH prediction is consistent with our understanding of OH chemistry.

$$[ISO] = \frac{E}{k_{iso+OH}} \frac{1}{[OH]} \tag{3.1}$$

For each site, isoprene and OH concentrations are normalized to their mean to facilitate an integrated analysis. We then segregate the samples into two groups; the first group contains samples with OH levels lower than the average, and samples with higher than average OH conditions are summarized into the second group. The number of samples are similar in both groups, demonstrating that the distribution of OH levels are not heavily skewed and the average OH levels are not driven by the outliers. This segregation method ensures a significant difference in OH levels between both groups. The statistics are summarized in Table 3.1. The difference in OH levels after segregation is consistent across the four sites. The first groups present OH levels on average 70% of the mean condition, whereas OH levels in the second group are $\sim$25% higher than the average.

Figure 3.3 shows the normalized isoprene in both groups for individual sites. We also diagnose the distribution of isoprene using T-test analysis. Characteristic of low OH, the first group exhibits a higher than average isoprene abundance, ranging from 13% to 29% above average. An opposite pattern is found in the second group marked by high OH. The isoprene

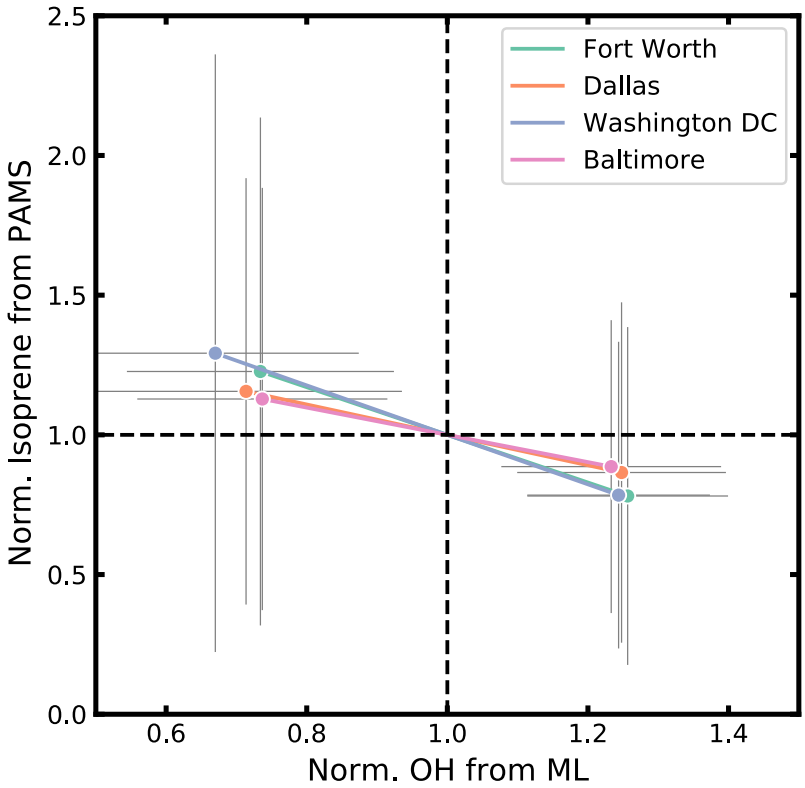

Figure 3.3: The opposite relationship between isoprene from ground measurements and OH from model prediction using OMI satellite observations. Both isoprene and OH are normalized to their average, and are segregated into two groups based on their OH levels. The sites include Fort Worth, Dallas, Washington DC and Baltimore.

observations coincident with high OH show a consistent lower than average level, ranging from 11% to 22% below average. Note that the ML OH is predicted without knowing the isoprene concentration, and the PAMS measurements are independent of our ML model. This observed negative correlation is a strong evidence that predicted OH is chemically reasonable.

We also investigate the role of temperature. Temperature variations lead to a perturbation of isoprene. The data segregation into high and low isoprene groupings is not correlated with temperature, but rather emerges from OH variations. To confirm this independence of temperature, we performed a two-sided T-test to diagnose the distribution of temperature. Each site shows that there is no significant difference in temperature between the low and high OH groups.

City	Norm. OH	Norm. Isoprene	p value (iso)	Temperature (K)	p value (temp)
Fort Worth	0.73 (0.19) 1.26 (0.14)	1.23 (0.91) 0.78 (0.60)	0.0002	305.4 (4.2) 304.4 (3.3)	0.10
Dallas	0.71 (0.22) 1.25 (0.15)	1.16 (0.76) 0.86 (0.61)	0.0019	304.2 (5.2) 303.8 (4.2)	0.58
Washington DC	0.67 (0.20) 1.24 (0.13)	1.29 (1.07) 0.78 (0.55)	0.0002	300.2 (4.0) 299.3 (3.2)	0.16
Baltimore	0.74 (0.18) 1.23 (0.16)	1.13 (0.76) 0.89 (0.52)	0.03	300.2 (4.0) 299.6 (2.8)	0.30

Table 3.1: The statistical analysis of temperature, normalized isoprene and normalize OH across four PAMS sites located in Fort Worth, Dallas, Washington DC and Baltimore, respectively. The values in the brackets represent the corresponding standard deviations. Two-sided T tests are applied on temperature and normalized isoprene to determine if there is a significant difference between the means of two groups for each city. A P value smaller than 0.05 is considered statistically significant.

Comparison of satellite constrained OH with WRF-Chem simulated OH

We compare our ML OH prediction constrained by satellite observations against the WRF-Chem simulation, and aim to validate our OH prediction by interpreting the OH difference between our OH prediction ("General-Satellite") and the WRF-Chem simulations. We find that the discrepancy is physically reasonable and attribute it to the difference in the NO_2 column between model and observations.

We compare the annual trends between ML OH prediction ("General-Satellite") and the WRF-Chem simulation, shown in Fig. 3.4(a). Annual average OH predicted using satellite observed NO_2 and HCHO columns as features is $\sim$10% lower than WRF-Chem OH, which we interpret as resulting from the difference in the annual trends of NO_2 column. Annual average NO_2 and HCHO columns are shown in Fig. 3.4 (b) and (c). Overall WRF-Chem agrees well with OMI for HCHO column, both of which present a fairly constant HCHO column over the course of ten years. However, WRF-Chem exhibits a large disagreement with respect to the annual trends of NO_2 column. In 2005, both WRF-Chem and OMI NO_2 columns are 4.3×10^{15} mole cm^{-2} on average over North American cities. However, WRF-Chem consistently overestimates NO_2 columns afterwards. The largest positive bias is observed between 2009 and 2011 when WRF-Chem NO_2 columns are up to 70% greater than those observed by OMI. WRF-Chem shows a fairly linear decrease at the rate of 0.17×10^{15} mole cm^{-2} per year. Satellite observed NO_2 columns show a sharper decrease before 2010 and the reduction slows afterwards. Coincidentally, the two records are close to matching again in 2014.

In terms of the annual trend, both model simulation and satellite observations agree on a

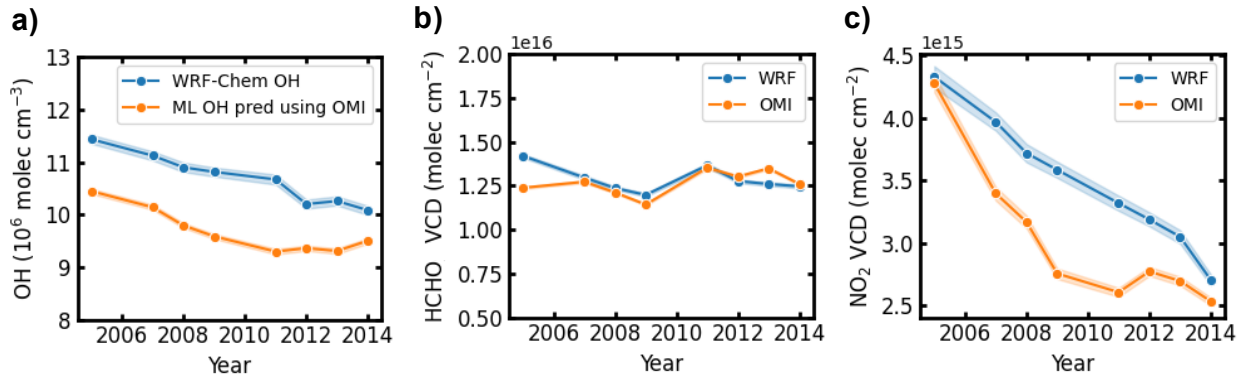

Figure 3.4: The comparison of the trends in annual averages of a) OH directly from WRF-Chem simulation and OH predicted from the ML model using observation-based features, b) WRF-Chem + OMI HCHO column and c) WRF-Chem + OMI NO_2 column.

decreasing pattern over the years. Both show a similar rate of decrease before 2010. After 2010, the observation-based OH predictions show no significant decrease while the modeled-based OH predictions continue decreasing on the order of ∼10% per year.

We also investigate the comparison of spatial gradient between city center and the surrounding areas shown in Appendix B.6 and Fig. B.7. Overall, further away from the city center there is better agreement between OH predictions and WRF-Chem simulations, and it coincides with better agreement between modeled and observed NO_2 columns.

3.5 Discussion: further improvement

We conclude in Sect.3.1 that our current ML model is capable of explaining 76% of the simulated OH variability from WRF-Chem. This is the best performance achievable with the current suite of globally available observations. Here we discuss the factors that would further improve the model performance to shed light on how future observations might benefit predictions and assessment of OH across urban regions.

To determine what factors would improve the ML predicted OH the most, we add each variable under consideration as a seventh input feature to the ML, retrain the ML on the new combined feature set, and compare the updated ML performance to the current model trained on six features. The two features that lead to significant improvement in the ML model performance are the isoprene column and surface NO.

Isoprene column

The isoprene column improves the ML performances substantially more than all other candidates. Introducing the isoprene column into the feature sets allows the ML model to capture 89% of the OH variability and decreases the RMSE from 2.11×10^6 molec cm^{-3} to 1.30×10^6 molec cm^{-3}. This emphasizes that the role of isoprene on OH chemistry is larger than all other VOC species that are present in urban environment.

We also note a redundancy of including both HCHO column and isoprene column. We tested another model trained on six parameters where HCHO column is replaced by the isoprene column. This model results in R^2 of 88% and corresponding RMSE of 1.45×10^6 mole cm^{-3}, which is very similar to the model whose features include both the isoprene and HCHO columns. It is a well-established approach to constrain isoprene concentrations by employing HCHO columns (Marais et al., 2014; Millet et al., 2008; Bauwens et al., 2016). Our result shows that HCHO column cannot represent the full extent of the role isoprene plays in OH chemistry and highlights the necessity of direct isoprene measurements. Recent studies have demonstrated the potential for space-based measurements of isoprene. Fu et al. (2019) diagnosed the isoprene spectral signatures detectable from space using the satellite-borne Cross-track Infrared Sounder (CrIS) for the first time, and Wells et al. (2020) developed an artificial neural network (ANN)-based algorithm for deriving global isoprene columns from the CrIS measurements. Implementing these isoprene columns into the ML feature set would achieve better constraints on urban OH in the future.

Surface NO

The second effective feature is the surface NO. Adding surface NO into the feature sets and retraining the ML model yields an improved R^2 from 76% to 84% and an reduced RMSE from 2.6×10^6 mole cm^{-3} to 1.6×10^6 mole cm^{-3}. Surface NO compensates the existing NO_2 column as a control over OH. For instance, it constrains the OH loss pathway via the production of alkyl nitrates which depends on NO rather than NO_2.The combination of NO and NO_2 better captures the decline of NO_x emission over the years as well.

Incorporating surface NO into the feature sets requires continuous NO observations. Compared to the chemical components detectable from the space, surface NO relies on in-situ observations. EPS AQS, for instance, provides hourly surface NO measurements at the widest regional converge. It provides the potential to expand OH prediction from ML model using the ground measurements.

3.6 Conclusion

We propose a generalized machine learning model that combines information about OH from a CTM with satellite observations to describe surface OH levels across 49 cities over

North America. A gradient boosted tree is trained on WRF-Chem simulations to produce a simplified presentation of urban OH chemistry. Here we utilize six predictive parameters, including surface $J(O^1D)$, water vapor, temperature, pressure and two column features, NO_2 column and HCHO column. All of these parameters are observable.

We evaluate the model performance using the testing data sets that are independent of those used for training. Our ML model explains 76% of the OH variability with a RMSE of 2.11×10^6 molec cm^{-3} across different urban environments. Accounting for the uncertainty of the two column features where we use satellite observations increases the RMSE to 3.2×10^6 molec cm^{-3}. The feature relative importance is proposed as an effective indicator of the physical processes that drive OH chemistry.

We then construct the feature set from the satellite observations, and feed them into our ML model for prediction of daily OH levels across the study domain. We validate this ML model by showing that it is consistent with our understanding of the effect of OH chemistry on isoprene. No information about isoprene is directly included in the training data set. Comparing the OH prediction to measurements of isoprene, we found a consistent inverse relationship between isoprene and OH as expected. We also compare the predicted OH from the ML model using observation-based features against WRF-Chem simulations, and conclude that the difference is well explained by the difference between modeled and observed NO_2 column.

We discuss the further improvement to the performance of this ML model, which could be accomplished by adding the observed isoprene column or surface NO observation to the feature sets. With additional satellite observations at higher spatial and temporal resolution available, we foresee a better constraints on surface OH utilizing this ML model technique.

Chapter 4

Estimate of OH Trends over One Decade in North American Cities

The chapter was adapted from: Q. Zhu, J. L. Laughner, and R. C. Cohen (2022b). "Estimate of OH trends over one decade in North American cities". *Proceedings of the National Academy of Sciences* 119.16, e2117399119

4.1 Introduction

The hydroxyl radical (OH) is the dominant oxidant in the atmosphere. Reactions with OH initiate the chemistry of a variety of trace gases (Levy, 1971; Ehhalt, 1998; Lelieveld et al., 2004), including greenhouse gases such as methane (CH_4) and primary pollutants including carbon monoxide (CO), nitrogen dioxides (NO_x ($\equiv$ NO+NO_2)) and volatile organic compounds (VOCs). As a result, OH affects radiative forcing over a global scale and governs local pollution events over cities. In cities, the lifetime of the freshly emitted species is anti-correlated with the OH concentration(Valin et al., 2013). Laughner and Cohen (Laughner and Cohen, 2019b) observe the NO_x lifetime directly from the space and concludes significant shifts in the NO_x lifetime occurred between 2005 and 2014 among 30 North American cities, which in turn suggests an underlying variation in OH in these cities.

Moreover, OH defines the production of ozone (O_3) (Thornton et al., 2002; Stone et al., 2012). Ground-level ozone is a major secondary pollutant that leads to negative impacts on human health and triggers the risk of death from respiratory causes (Jerrett et al., 2009). Ozone exceeds health based standards most often during summertime. Ozone results from reactions involving two predominant ozone precursors: NO_x and VOCs. In the presence of sunlight, OH oxidizes VOCs to form organic peroxy radicals (RO_2) and then RO_2 can react with NO to form NO_2 which photolyzes to produce O_3. The ozone production rate $P(O_3)$ is a non-linear function of both NO_x and VOCs, and its dependence on NO_x is similar to the dependence of OH on NO_x. Two distinct regimes are observed. At high VOC reactivity and

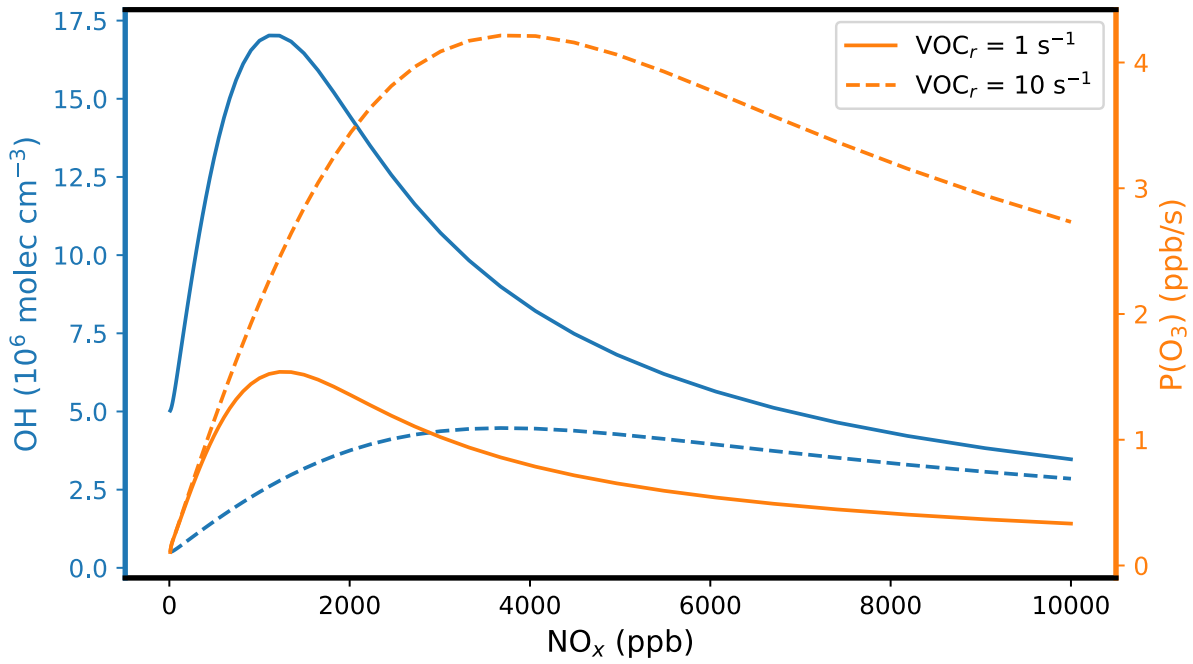

Figure 4.1: A schematic of OH and $P(O_3)$ as a function of NO_x at the photochemical steady state. We assume a NO_2/NO ratio of 4, the alkyl nitrate branching ratio α of 0.04, and a HO_x production rate of 0.3 ppt s^{-1}. Two scenarios represent a high VOC reactivity (VOC_r = 10 s^{-1}) condition and low VOC reactivity condition (VOC_r = 1 s^{-1}), respectively.

low NO_x, both $P(O_3)$ and OH increase with enhancing NO_x, and the corresponding regime is identified by the limiting reagent as a NO_x limited regime. In contrast, both $P(O_3)$ and OH show the opposite relationship with NO_x in the NO_x saturated regime, which is characterized by high NO_x compared to the VOC reactivity. In terms of reducing ozone pollution, the effectiveness of the emissions control strategy depends on whether the photochemical regime of ozone formation is a NO_x saturated or NO_x limited regime. Therefore, OH is the ideal target molecule to examine the chemical regime; the relationship between OH and NO_x at interannual time scales serves as an explicit proxy to monitor the shift of the chemical regimes.

Despite its pivotal role in oxidation chemistry, OH observations at urban or suburban areas are remarkably sparse. The longest record is reported in (Rohrer and Berresheim, 2006) where continuous OH measurements were conducted at a rural site in southern Germany between 1999 and 2003. Other OH measurements, occurring either in situ or airborne, are limited to a shorter time scale ranging from days to months (Emmerson et al., 2005b; Emmerson et al., 2007; Ren et al., 2003; Kanaya et al., 2007; Griffith et al., 2016; Sanchez et al., 2018; Lu et al., 2012; Lu et al., 2013). The short lifetime ($<$ 1s) of OH, owing to the

high reactivity, means local in situ chemistry dominates the OH budget. As a result, the high spatial heterogeneity makes it impossible to describe OH chemistry over a large spatial scale solely from in-situ OH observations.

In a recent paper, we developed a machine learning (ML) model to represent the OH chemistry emphasizing urban areas (Zhu et al., 2022a). The model aims to represent the OH chemistry simulated from a state-of-art chemical transport model relying on a small set of observed constraints that are available with records over one decade. The ML model with observational inputs from satellite remote sensing yields estimates of surface OH across 49 North American cities for the time period of 2005−2014.

4.2 Methods: models and observations

Observational and model records used

All observational inputs are publicly available. We use observations from the Ozone Monitoring Instrument (OMI). The NO_2 retrievals are from Version 3.0B of the Berkeley High Resolution (BEHR) OMI NO_2 product (`https://behr.cchem.berkeley.edu/`), and HCHO retrievals are from the Quality Assurance For Essential Climate Variables (QA4ECV) project (`www.qa4ecv.eu`). We conduct a start-of-art chemical transport model simulation using WRF-Chem over North America. Hourly outputs are sampled at the spatial resolution of 12km×12km. The model configuration is described in detail in (Laughner et al., 2018b).

ML model

We utilize a gradient boosted tree model to represent the OH chemistry over urban areas during summertime. It is a supervised machine learning model and is optimized for predicting the surface OH by learning the training data.

We prepare training data solely from a chemical transport model WRF-Chem. We use six parameters as predictors, including four surface variables ($J(O^1D)$, H_2O, temperature, pressure) and two column variables (NO_2 column and HCHO column). The calculation of two column variables incorporates the averaging kernel from the satellite products to emulate the quantities observed from the space, referring to the Sect.7.4 from Laughner et al. (2018b). We select the WRF-Chem grids covering 49 North American cities and each grid has a spatial scale of 12km×12km. To represent each city, we select grid cells in a circular area with the radius varying from 0.5 deg to 1.0 deg around the city center based on the city size and the surrounding interference. The selection of 49 cities is consistent with Russell et al. (2012) and Laughner and Cohen (2019b). We constrain the time to ∼13:30 local hour from April through September between 2005 and 2014 to present summertime conditions where the ozone pollution due to active photochemistry is most of a concern. For each city, we only filter out the days with lightning occurrence and with cloud fraction larger than 0.2.

Zhu, Laughner, and Cohen (Zhu et al., 2022a) evaluate the accuracy of this ML model and prove that the ML model using this six parameters is capable of capturing 76% of the OH variability and yields a RMSE of 2.1 $\times$ 10^6 molec cm^{-3}. Therefore, the ML model serves as an efficient alternative of OH simulation using the computationally expensive chemical transport model.

OH predictions

We combine model simulations and satellite observations to construct the observation-based inputs, and use the ML model to predict OH. Among the six features, we take $J(O^1D)$, H_2O, temperature and pressure from the WRF-Chem outputs. Since meteorological parameters are constrained by the North American Regional Reanalysis (NARR) every three hours, we expect these parameters are in good agreement with the observations. We use satellite retrievals described above to obtain both NO_2 column and HCHO column features. Based on the availability of OMI satellite observations and BEHR retrieval products that are optimized to remove bias on the spatial resolution of cities, we confine our study to 8 year between 2005 and 2014. OH Predictions for year 2006 and 2010 are absent due to lack of WRF-Chem or BEHR retrievals.

Zhu, Laughner and Cohen (Zhu et al., 2022a) calculate the uncertainty of the OH predictions. Besides of those inherent in the ML model, the uncertainties from observed input parameters, especially the NO_2 column and the HCHO column, propagate through the ML model configuration and lead to non-negligible influence on model performance. Considering the uncertainties of the retrievals products for both NO_2 column and HCHO column, we estimate the RMSE of OH predictions as 3.2 $\times$ 10^6 molec cm^{-3}.

Summertime average OH

We segregate the OH predictions by year and city, and then take the averages of grid cells per city per year to be representative of the summertime OH (Eqn.B.1):

$$OH_{city,summer} = \frac{\sum_{day_i \subset summer} \sum_{grid_j \subset city} OH_{day_i,grid_j}}{\sum_{day_i \subset summer} 1 \times \sum_{grid_j \subset city} 1} \tag{4.1}$$

The number of OH predictions used for calculation varies as it depends on the number of grids for each city region as well as the number of valid days. The number of individual grid OH predictions ranges between 1000 and 16000. The minimum number corresponds to summertime OH in 2014 over Orlando, Florida, which is consistent with a relatively small city size and fewer valid days in the analysis after filtering the days with lightning occurrence. We treat each OH prediction as an independent variable and use the lower bound of the

number of observations, the RMSE of summertime average OH is 1.0×10^5 molec cm^{-3}. It is a conservative estimate to compensate the fact that the OH predictions are not perfectly orthogonal.

We then, for each city, assess the relative difference of summertime average OH between 2005 and 2014 (rel. OH hereinafter). The summertime average OH across all cities ranges from 8.7×10^6 molec cm^{-3} to 1.33×10^7 molec cm^{-3} in 2005, and ranges from 8.2×10^6 molec cm^{-3} to 1.25×10^7 molec cm^{-3} in 2014. Considering the estimate of RMSE of 1.0×10^5 molec cm^{-3}, we calculate the upper bound of the standard deviation of rel. OH is 2%. Therefore we take 4% as a threshold in the analysis; a rel. OH larger than 4% is considered statistically significant with 95% confidence.

Relationship between OH and NO_2 column

To reconcile the large city-wise variation in both OH and NO_2 column, both OH and NO_2 column are normalized to their 2005 averages for a given city. We apply linear regressions to fit the normalized OH to the normalized NO_2 column and collect the slopes from the linear fitting. The shifts in slopes between OH and NO_2 column are discussed in the results.

4.3 Variation of urban OH over one decade

The 49 selected cities exhibit a full range of variation in OH chemistry as characterized by the HCHO columns and NO_2 columns. Both HCHO columns and NO_2 columns are acquired from satellite-based observations and serve as indicators for VOCs (Palmer et al., 2003; Fu et al., 2007; Fu et al., 2019) and NO_x (Martin et al., 2004; Lamsal et al., 2008), respectively. We use the ratio of the HCHO column and the NO_2 column (satellite HCHO/NO_2) to reflect the relative availability of NO_x and total organic reactivity to hydroxyl radicals sillman95. Fig. 4.2 shows the ratio of average HCHO and NO_2 columns during April to September between 2005 and 2014 over selected cities. The satellite HCHO/NO_2 varies by a factor of 3, reflecting a range in NO_x and VOC chemistry. High satellite HCHO/NO_2 is indicative of an abundance of VOC relative to NO_x and presents in southeast US cities. It is consistent with VOC emissions mostly from biogenic sources, for instance, isoprene from vegetation (Guenther et al., 2006). In contrast, the cities along the west coast and the Northwest US exhibit a relatively low satellite HCHO/NO_2 ratio. Those cities feature large anthropogenic NO_x emissions whereas the VOC emissions are unreactive compared to the Southeast US(Kharol et al., 2015).

It also worth emphasizing the variation of the NO_2 and HCHO columns over one decade. Anthropogenic NO_x emissions exhibited a significant reduction over the US due to stringent air pollution regulations during the 2005−2014 period. This is reflected in the decline in the satellite-observed NO_2 column. The selected cities include examples with the largest NO_2 column as well as the most pronounced reduction (Fig. C.1). The observed NO_2 column

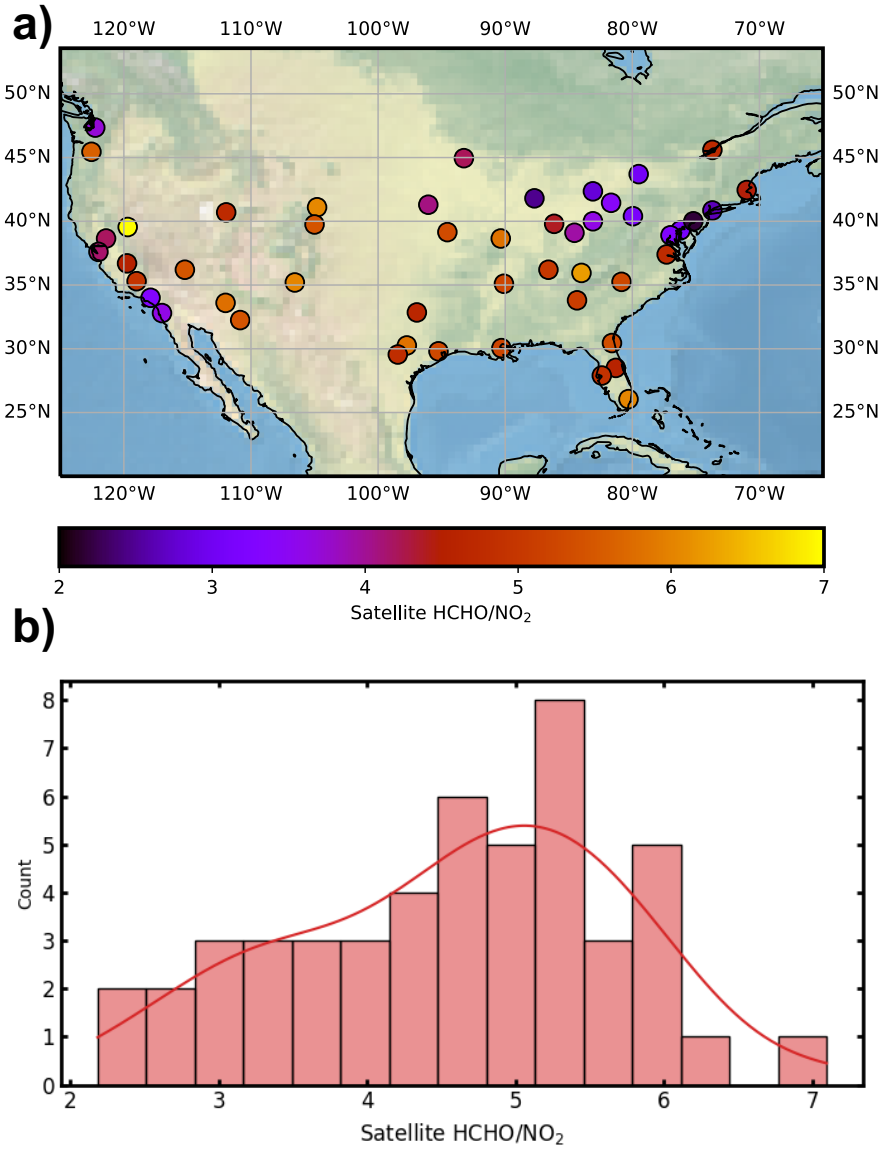

Figure 4.2: The satellite $HCHO/NO_2$ over selected 49 cities. a) The map of satellite based summertime average of $HCHO/NO_2$ between 2005 and 2014 over 49 North American cities, b) shows the frequency distribution of satellite $HCHO/NO_2$.

decreases by 33% on average over this time period. The largest decline of NO_2 column by up to 55% is observed in Los Angeles, followed by other populous cities including Chicago, Boston and New York. Austin observes the smallest decrease, 11%. We also note the smaller decrease of the NO_2 column over urban regions in Central US, which is thought to be partially due to the offset of increasing soil NO_x emission (Vinken et al., 2014). Compared to the NO_2 column, HCHO columns show no consistent interannual variation (Fig. C.2). Among the selected cities, the relative change of HCHO column between 2005 and 2014 ranges from -15% to 10%. The causes of 10 years variation in the HCHO column are complex. While the anthropogenic VOC emissions from vehicles and industry declined(EPA, 2016), volatile chemical product emissions may be growing (McDonald et al., 2018). Also, the changes in anthropogenic VOC emissions are masked by the large HCHO background driven by biogenic sources(Zhu et al., 2017).

The interannual variation in both the NO_2 column and the HCHO column leads to variation in OH. Compared to summertime in 2005, the relative change of urban OH in 2014 ranges from -17% to 11% over the 49 cities (Fig. 4.3). We find 30 cities show statistically significant changes in surface OH between 2005 and 2014. In four cities, including Los Angeles, New Orleans, New York and Toronto, the increase of summertime averaged OH is larger than 4%. 30 out of 49 cities witness a decline of annual OH in 2014 larger than -4%. Uncertainties are described in the Method. The full OH trends between 2005 and 2014 for each city are shown in Fig. C.3.

4.4 The relationship between OH and NO_2 column

Mapping the predicted OH to the concurrent NO_2 column depicts the relationship between OH and NO_x, and it reveals which chemical regime the urban environment falls in. For each city we select the areas covering both city center and surrounding areas. If we assume that VOC reactivity is similar in all grids for a given urban area for a given year, the relationship between OH concentration and NO_2 column provides information about the dominant chemical regime. Assuming minimal variation in the VOC reactivity is supported by the small annual variation in HCHO shown in Fig. S2 and similar weekend/weekday VOC reactivity observed in Beirle et al. (e.g. 2003), Kaynak et al. (2009), and Russell et al. (2010).

Recall from Fig. 4.1 that the dependence of OH on NO_x is non-linear, and the slope of OH vs NO_x varies with its chemical regime. In the NO_x saturated regime, OH is inversely correlated with NO_x yielding a negative slope. The turnover point between the NO_x saturated regime and NO_x limited regime leads to a slope fluctuating around the zero point. Conversely, in the NO_x limited regime, the slope is positive. The further away from the turnover point, the slope is larger.

Figure 4.4 shows how two cities, Los Angeles and Denver, illustrate different relationships

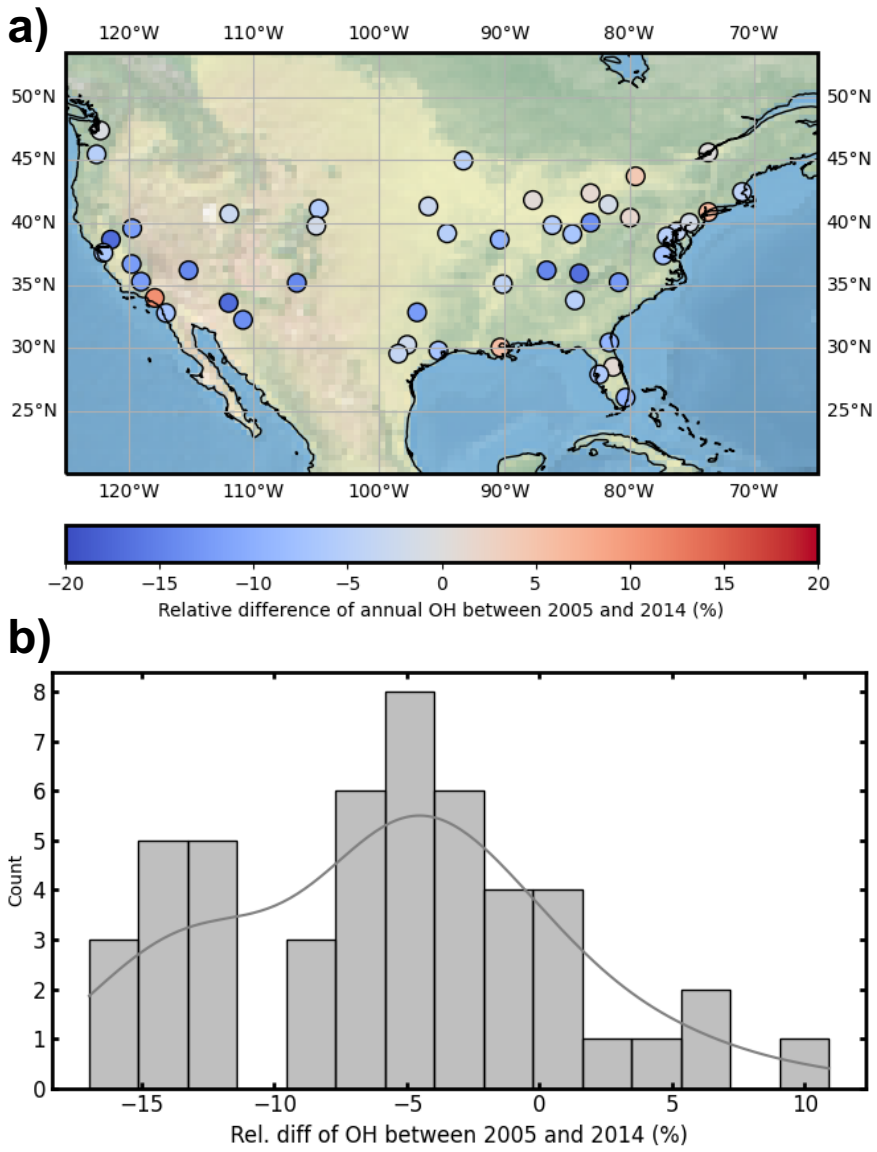

Figure 4.3: The OH variation over selected 49 cities. a) The map of the relative difference of summertime OH between 2005 and 2014 over 49 North American cities, the frequency distribution is shown in b).

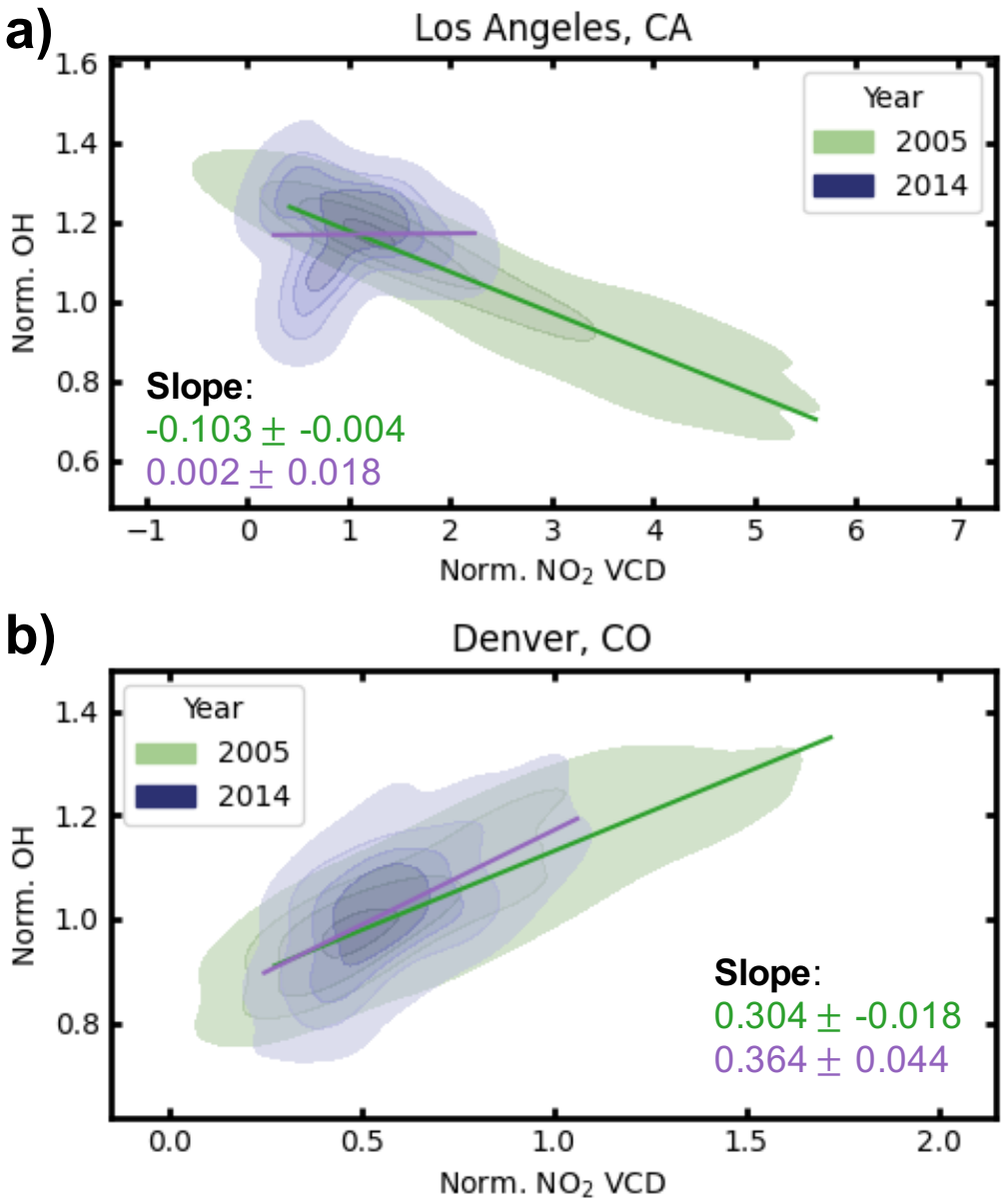

Figure 4.4: The density plot between OH and NO_2 column in 2005 and 2014 over LA (a) and Denver (b), respectively. For each city, both OH and NO_2 column are normalized to their annual averages in 2005. The lines and corresponding slopes denote the linear regression results between normalized OH and normalized NO_2 column.

between OH and NO_2 column and how it has shifted over the years. In 2005, Los Angeles was characterized by high NO_x gottlieb06. The average NO_2 column was 9.2×10^{15} molec cm^{-2} and the largest NO_2 column was 2.4×10^{16} molec cm^{-2}. The OH from the ML model also shows a wide spread within the city where OH concentration varies by a factor of 2. We note a significant inverse relationship; a higher NO_2 column corresponds to a lower OH concentration, yielding a slope of -0.1 (Fig. 4.4a). The observed slope matches the theoretical pattern of a NO_x saturated regime as shown in Fig.4.1. In contrast, LA in 2014 presented a much lower NO_2 columns. The average NO_2 column is 60% lower than in 2005. Compared to the remarkable decline in NO_2 column, the OH concentration shows a slight enhancement, on average 10% higher than those in 2005. As a consequence, the negative correlation between OH and the NO_2 column in 2005 vanishes. In 2014, OH presented a strong non-linear dependence on NO_2 column. Though a linear regression fails to describe the full pattern between OH and the NO_2 column, the slope from linear fitting shows a large fluctuation near the zero point, indicative of the turnover point between the NO_x saturated regime and NO_x limited regime. Expanding the relationship analysis of OH and NO_2 column to each year between 2005 and 2014 shows a continuous increase of the slope, indicating a consistent transition from a NO_x saturated regime (Fig. C.4).

In contrast, the OH-NO_2 column relationship in Denver indicates that NO_x-limited chemistry dominated the Denver plume between 2005 and 2014 (Fig. C.5) and Fig. 4.4b shows the OH-NO_2 column relationship in 2005 and 2014. In 2005, the NO_2 column was moderate compared to LA; the average NO_2 column was 2.8×10^{15} molec cm^{-2} and the largest NO_2 column was 7.2×10^{15} molec cm^{-2}. A positive correlation between OH and NO_2 column is observed, with a slope of 0.30. The slope of the correlation suggests Denver was already NO_x limited in 2005. In 2014, on average, there was a 16% decrease in the NO_2 column. However, the peak NO_2 column decreased by 36%, reflecting the effective emission control near the city center. The positive correlation between OH and NO_2 column continues in 2014 with its fitted slope increasing from 0.30 to 0.36. The enhancement in slope is consistent with in 2014 moving further away from the turnover point along with the decline in the NO_2 column.

We extend the investigation of the relationship between OH and NO_2 column to 49 cities. In both 2005 and 2014, we conduct the linear regression between normalized OH and normalized NO_2 column; these slopes are summarized in Fig. 4.5 and the slopes for all years between 2005 and 2014 are shown in Fig. C.6. 2005 sees a wide scatter of the slope between normalized OH and normalized NO_2 column. 5 cities, including New Orleans, Los Angeles, Tampa, Boston, present a negative relationship between OH and NO_2 column. 16 cities yield a slope fluctuating around zero and a correlation coefficient (r^2) lower than 0.6. The rest of cites observe strong positive correlations ($r^2 > 0.6$) with the slope larger than 0.2.

In 2014, the slopes in 45 out of 49 cities are more positive than they were in 2005. Cities such as LA, have a negative slope closer to zero, indicating a transition from the NO_x saturated regime to the turnover point of two regimes. Most cities whose slope is positive in 2005

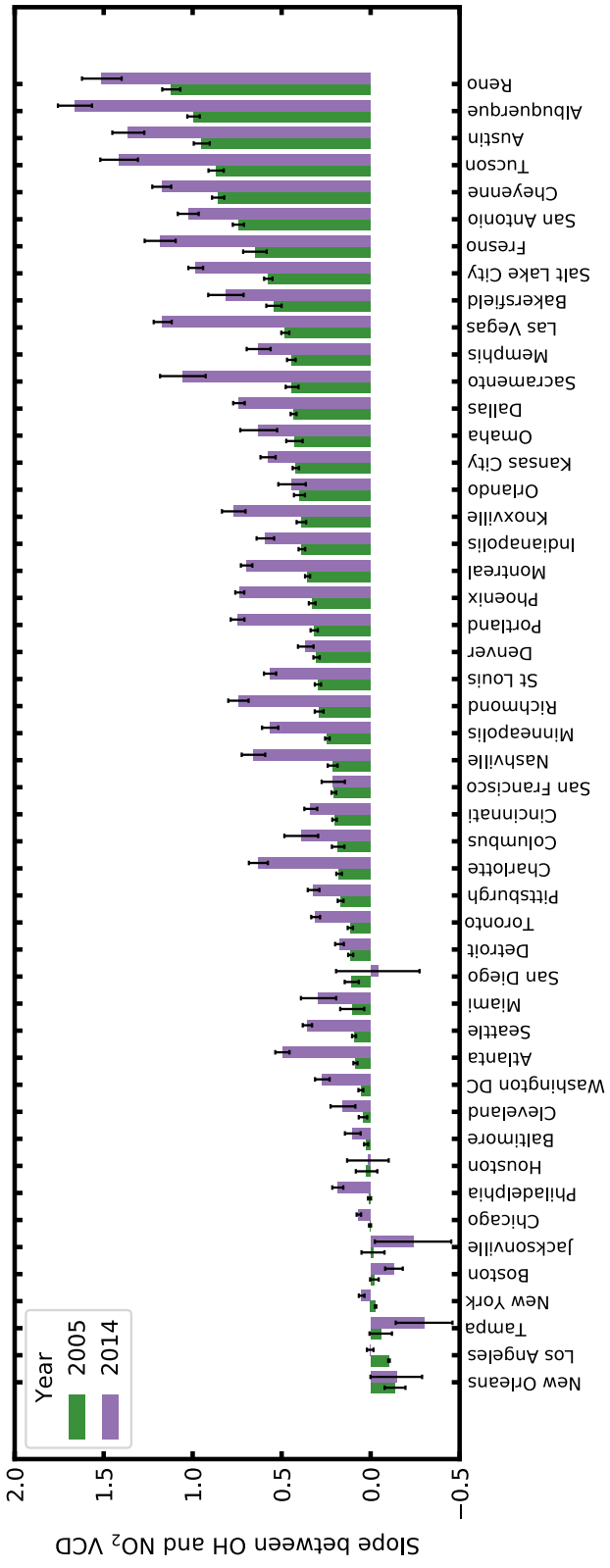

Figure 4.5: The slope calculated from linear fitting between normalized OH and normalized NO_2 column among 49 North American cities in both 2005 and 2014, same as Fig. 4.4. The error bar denotes the standard deviation of the fitted slope.

increase further, demonstrating a shift within the NO_x limited regime.

4.5 Implication for controlling ozone pollution

In 2021, 50 areas and 196 counties are designated as ozone nonattainment areas where 8 hour ozone levels fail to meet the National Ambient Air Quality Standards (NAAQS), affecting over 120 million peopleepa-ozone-nonattainment. Efforts devoted to reducing high ozone have focused on reduction of O_3 precursors emitted by anthropogenic sources. NO_x and VOC emission reductions have occurred kharol15, russell12. However, the effectiveness of emission control on lowering ozone level encompasses a large variation and is associated with the chemical regime the urban environment. In NO_x saturated regime, NO_x emission reductions are detrimental to the mitigation of ozone pollution in a short term. In the NO_x limited regime, there are immediate benefits. Based on our conclusion of the chemical regime shifts, most North American cities were NO_x limited in 2014. If further controls on NO_x emission are prioritized for regulating ozone, the regulations will likely be effective.

4.6 Conclusion

We leverage machine learning combined with satellite observations, to estimate surface OH in 49 cities. We found changes in the summertime OH between 2005 and 2014, ranging from a decrease of 17% to an enhancement of 11%. We observe a shift of chemical regimes with a NO_x limited regime now in effect in most cities. Thus continued reduction of NO_x emissions will effectively control ozone.

Code and data availability

The analysis code is available at doi.org/10.5281/zenodo.5296044 (Zhu, 2021) and intermediate data sets are available at doi.org/10.6078/D1FM75 (Zhu et al., 2021).

Chapter 5

Concluding remarks

The hydroxyl radical, OH, initiates the removal of the majority of trace gases in the atmosphere and is intimately involved in the oxidation chemistry of the atmosphere. As a result of its high reactivity, the OH concentration is determined primarily by local physical and chemical conditions and is only affected by transport to the extent its precursors are transported. OH measurements support the idea that we have a good understanding of OH chemistry and that this chemistry is dominated by NO_x, VOC and meterological parameters affecting photolysis rates and reaction kinetics. In this thesis, I aim to constrain OH and its chemistry using observations of longer-lived species, among which NO_x is of particular interest as it plays a crucial role. I emphasize satellite observations of NO_2 column density since recent advances in measurements provide unprecedented spatial coverage and consistent temporal records.

In Chapter 2, I investigate lightning NO_x emissions, the largest source of uncertainty in OH in the free troposphere. I use satellite observations to constrain a chemical transport model with a new approach to describing lightning. Lightning NO_x production rates are varied in the model until good agreement with the satellite observations are obtained. The best estimate of lightning NO_x emissions is 500 mol NO flash^{-1}, which is within the range of current lightning NO_x emission estimates but closer to the high limit. The result indicates that the impact of lightning on OH in the free troposphere is higher than what is discussed in the current literature.

Future work is proposed to quantify lightning induced OH based on the new CAPE-PR lightning parameterization and lightning NO_x production rate described in Chapter 2. Nevertheless, the projection of lightning under climate change is controversial. Studies simulating future lightning over the next century with the CTH approach have reported 5–16% increases in lightning flashes per degree increase in global mean surface temperature (e.g. Schumann and Huntrieser, 2007; Jiang and Liao, 2013; Clark et al., 2017). Banerjee et al. (2014) identified large climate-change-induced enhancements in OH concentration in the tropical upper

troposphere primarily as a consequence of greater lightning NO_x. However, Finney et al. (2018) suggested a 15% decrease of lightning in 2100 under a strong global warming scenario using IFLUX lightning parameterization. In the future, we should explore how lightning responds to climate change using CAPE-PR parameterization, and study the simultaneous future projection of OH in the free trosposphere.

In Chapter 3, I leverage machine learning approach to estimate OH concentrations in cities. Since there are only 12 cities with OH measurements and each of these only for a short period, the utilization of machine learning advances the capability of investigating OH abundance substantially both in time and in space. I show that a machine learning model can be trained based on computationally expensive chemical transport model simulations and is able to predict OH using parameters that are either from weather model or from satellite observations. Therefore, in Chapter 4, I predict near surface OH concentration variations over 49 North American cities over the course of ten years using machine learning combined with satellite observed NO_2 column density and HCHO column density. This analysis shows the OH trends in one decade in each city and also provides insights into the transition of chemical regimes in each city.

This machine learning approach opens the door to integrated analysis of OH chemistry on a variety of spatial and temporal scales. While Chapter 3 shows the past trends of OH in cities, it can also used to investigate the future changes of OH. Shared Socio-Economic Pathways (SSPs) are the new generation of scenarios primarily framed within the context of climate change mitigation and have been used in CMIP6 (Riahi et al., 2017). These scenarios reflect plausible future emissions in 21st century based on socioeconomic, environmental, and technological trends. Each SSP narrative is mapped to three categories measuring the pollution control strength (strong, median, weak), in which categories the trends of emissions factors (i.e., emissions per unit of energy) for each pollutant are prescribed (O'Neill et al., 2016). We can construct the inputs to the ML model using these emission trends and projected climate records (e.g., temperature, humidity) from CMIP6 model under different SSP scenarios, and then use the ML model to predict OH trends at the given conditions. Such a prediction would be much less computationally demanding than running a fully coupled chemistry-climate model at a resolution compatible with urban chemistry ($\sim$4-12km). The variations among the predicted OH trends will reflect the impacts of oxidative capacity in the future under different climate change mitigation strategies.

Bibliography

Allen, D. et al. (2010). "Impact of lightning NO emissions on North American photochemistry as determined using the Global Modeling Initiative (GMI) model". *Journal of Geophysical Research: Atmospheres* 115.D22. DOI: 10.1029/2010JD014062. eprint: https://agupubs.onlinelibrary.wiley.com/doi/pdf/10.1029/2010JD014062.

Allen, D. J. and K. E. Pickering (2002). "Evaluation of lightning flash rate parameterizations for use in a global chemical transport model". *J. Geophys. Res. Atmos.* 107.D23, ACH 15–1–ACH 15–21. DOI: 10.1029/2002JD002066. eprint: https://agupubs.onlinelibrary.wiley.com/doi/pdf/10.1029/2002JD002066.

Anenberg, S. C. et al. (2010). "An Estimate of the Global Burden of Anthropogenic Ozone and Fine Particulate Matter on Premature Human Mortality Using Atmospheric Modeling". *Environmental Health Perspectives* 118.9, pp. 1189–1195. DOI: 10.1289/ehp.0901220. eprint: https://ehp.niehs.nih.gov/doi/pdf/10.1289/ehp.0901220.

Banerjee, A. et al. (2014). "Lightning NO x, a key chemistry–climate interaction: impacts of future climate change and consequences for tropospheric oxidising capacity". *Atmospheric Chemistry and Physics* 14.18, pp. 9871–9881.

Barkley, M. P. et al. (2012). "Assessing sources of uncertainty in formaldehyde air mass factors over tropical South America: Implications for top-down isoprene emission estimates". *Journal of Geophysical Research: Atmospheres* 117.D13.

Barth, M. C. et al. (2015). "The Deep Convective Clouds and Chemistry (DC3) Field Campaign". *Bulletin of the American Meteorological Society* 96.8, pp. 1281–1309. DOI: 10.1175/BAMS-D-13-00290.1. eprint: https://doi.org/10.1175/BAMS-D-13-00290.1.

Bauwens, M. et al. (2016). "Nine years of global hydrocarbon emissions based on source inversion of OMI formaldehyde observations". *Atmospheric Chemistry and Physics* 16.15, pp. 10133–10158.

Bechle, M. J., D. B. Millet, and J. D. Marshall (2013). "Remote sensing of exposure to NO2: Satellite versus ground-based measurement in a large urban area". *Atmospheric Environment* 69, pp. 345–353. ISSN: 1352-2310. DOI: https://doi.org/10.1016/j.atmosenv.2012.11.046.

Beirle, S., H. Huntrieser, and T. Wagner (2010). "Direct satellite observations of lightning-produced NO_x". *Atmos. Chem. Phys.* 10, pp. 10965–10986. DOI: 10.5194/acp-10-10965-2010.

Beirle, S et al. (2003). "Weekly cycle of NO 2 by GOME measurements: a signature of anthropogenic sources". *Atmospheric Chemistry and Physics* 3.6, pp. 2225–2232.

Blitz, M. et al. (2004). "Pressure and temperature-dependent quantum yields for the photodissociation of acetone between 279 and 327.5 nm". *Geophysical Research Letters* 31.6.

Boccippio, D. J., W. J. Koshak, and R. J. Blakeslee (2002). "Performance Assessment of the Optical Transient Detector and Lightning Imaging Sensor. Part I: Predicted Diurnal Variability". *Journal of Atmospheric and Oceanic Technology* 19.9, pp. 1318–1332. DOI: 10.1175/1520-0426(2002)019<1318:PAOTOT>2.0.CO;2.

Boersma, K. F., G. C. M. Vinken, and H. J. Eskes (2016). "Representativeness errors in comparing chemistry transport and chemistry climate models with satellite UV–Vis tropospheric
column retrievals". *Geoscientific Model Development* 9.2, pp. 875–898. DOI: 10.5194/gmd-9-875-2016.

Boersma, K. et al. (2011). "An improved tropospheric NO 2 column retrieval algorithm for the Ozone Monitoring Instrument". *Atmospheric Measurement Techniques* 4.9, pp. 1905–1928.

Brune, W. et al. (1998). "Airborne in-situ OH and HO2 observations in the cloud-free troposphere and lower stratosphere during SUCCESS". *Geophysical Research Letters* 25.10, pp. 1701–1704.

Brune, W. et al. (2020). "Exploring oxidation in the remote free troposphere: Insights from Atmospheric Tomography (ATom)". *Journal of Geophysical Research: Atmospheres* 125.1, e2019JD031685.

Brune, W. et al. (2021). "Extreme oxidant amounts produced by lightning in storm clouds". *Science* 372.6543, pp. 711–715.

Brune, W. H. et al. (2018). "Atmospheric oxidation in the presence of clouds during the Deep Convective Clouds and Chemistry (DC3) study". *Atmospheric Chemistry and Physics* 18.19, pp. 14493–14510.

Bucsela, E. et al. (2013). "A new stratospheric and tropospheric NO 2 retrieval algorithm for nadir-viewing satellite instruments: applications to OMI". *Atmospheric Measurement Techniques* 6.10, pp. 2607–2626.

Bucsela, E. J. et al. (2010). "Lightning-generated NOx seen by the Ozone Monitoring Instrument during NASA's Tropical Composition, Cloud and Climate Coupling Experiment (TC4)". *Journal of Geophysical Research: Atmospheres* 115.D10. D00J10, n/a–n/a. ISSN: 2156-2202. DOI: 10.1029/2009JD013118.

Burnett, R. et al. (2018). "Global estimates of mortality associated with long-term exposure to outdoor fine particulate matter". *Proceedings of the National Academy of Sciences* 115.38, pp. 9592–9597.

Cantrell, C. A. et al. (2003). "Steady state free radical budgets and ozone photochemistry during TOPSE". *Journal of Geophysical Research: Atmospheres* 108.D4.

Cecil, D. J., D. E. Buechler, and R. J. Blakeslee (2014). "Gridded lightning climatology from TRMM-LIS and OTD: Dataset description". *Atmospheric Research* 135-136, pp. 404 – 414. ISSN: 0169-8095. DOI: https://doi.org/10.1016/j.atmosres.2012.06.028.

Chen, T. and C. Guestrin (2016). "Xgboost: A scalable tree boosting system". In: *Proceedings of the 22nd acm sigkdd international conference on knowledge discovery and data mining*, pp. 785–794.

Choi, Y. et al. (2005). "Evidence of lightning NOx and convective transport of pollutants in satellite observations over North America". *Geophysical Research Letters* 32.2. DOI: 10.1029/2004GL021436. eprint: https://agupubs.onlinelibrary.wiley.com/doi/pdf/10.1029/2004GL021436.

Clark, S. K., D. S. Ward, and N. M. Mahowald (2017). "Parameterization-based uncertainty in future lightning flash density". *Geophysical Research Letters* 44.6, pp. 2893–2901.

Coggon, M. M. et al. (2021). "Volatile chemical product emissions enhance ozone and modulate urban chemistry". *Proceedings of the National Academy of Sciences* 118.32.

Crutzen, P. J. (1979). "The role of NO and NO2 in the chemistry of the troposphere and stratosphere". *Annual review of earth and planetary sciences* 7.1, pp. 443–472.

Cummings, K. A. et al. (2013). "Cloud-resolving chemistry simulation of a Hector thunderstorm". *Atmospheric Chemistry and Physics* 13.5, pp. 2757–2777. DOI: 10.5194/acp-13-2757-2013.

De Smedt, I et al. (2012). "Improved retrieval of global tropospheric formaldehyde columns from GOME-2/MetOp-A addressing noise reduction and instrumental degradation issues". *Atmos Meas Tech* 5.11, pp. 2933–2949.

DeCaria, A. J. et al. (2005). "Lightning-generated NOX and its impact on tropospheric ozone production: A three-dimensional modeling study of a Stratosphere-Troposphere Experiment: Radiation, Aerosols and Ozone (STERAO-A) thunderstorm". *Journal of Geophysical Research: Atmospheres* 110.D14. DOI: 10.1029/2004JD005556. eprint: https://agupubs.onlinelibrary.wiley.com/doi/pdf/10.1029/2004JD005556.

Dedoussi, I. C. et al. (2020). "Premature mortality related to United States cross-state air pollution". *Nature* 578.7794, pp. 261–265.

Delmas, R., D. Serça, and C. Jambert (1997). "Global inventory of NOx sources". *Nutrient Cycling in Agroecosystems* 48.1, pp. 51–60. ISSN: 1573-0867. DOI: 10.1023/A:1009793806086.

Denman, K. L. et al. (2007). "Couplings between changes in the climate system and biogeochemistry". *International Panel on Climate Change*, pp. 499–587.

Donahue, N. M. et al. (1998). "Direct observation of OH production from the ozonolysis of olefins". *Geophysical Research Letters* 25.1, pp. 59–62.

Dusanter, S. et al. (2009). "Measurements of OH and HO_2 concentrations during the MCMA-2006 field campaign – Part 2: Model comparison and radical budget". *Atmospheric Chemistry and Physics* 9.18, pp. 6655–6675. DOI: 10.5194/acp-9-6655-2009.

Ehhalt, D. (1999). "Gas phase chemistry of the troposphere". *Global aspects of atmospheric chemistry* 6, pp. 21–110.

Ehhalt, D. H. (1998). "Radical ideas". *Science* 279.5353, pp. 1002–1003.

Eibern, H. and H. Schmidt (1999). "A four-dimensional variational chemistry data assimilation scheme for Eulerian chemistry transport modeling". *Journal of Geophysical Research: Atmospheres* 104.D15, pp. 18583–18598.

Eisele, F. L. et al. (1997). "Understanding the production and interconversion of the hydroxyl radical during the Tropospheric OH Photochemistry Experiment". *Journal of Geophysical Research: Atmospheres* 102.D5, pp. 6457–6465.

Elbern, H. and H. Schmidt (2001). "Ozone episode analysis by four-dimensional variational chemistry data assimilation". *Journal of Geophysical Research: Atmospheres* 106.D4, pp. 3569–3590.

Emmerson, K. M. et al. (2007). "Free radical modelling studies during the UK TORCH Campaign in Summer 2003". *Atmospheric Chemistry and Physics* 7.1, pp. 167–181.

Emmerson, K., N Carslaw, and M. Pilling (2005a). "Urban atmospheric chemistry during the PUMA campaign 2: Radical budgets for OH, HO2 and RO2". *Journal of atmospheric chemistry* 52.2, pp. 165–183.

Emmerson, K. et al. (2005b). "Urban atmospheric chemistry during the PUMA campaign 1: Comparison of modelled OH and HO 2 concentrations with measurements". *Journal of Atmospheric Chemistry* 52.2, pp. 143–164.

Emmons, L. K. et al. (2010). "Description and evaluation of the Model for Ozone and Related chemical Tracers, version 4 (MOZART-4)". *Geoscientific Model Development* 3.1, pp. 43–67.

EPA (2016). *Air Pollutant Emissions Trends Data*. URL: https://www.epa.gov/air-emissions-inventories/air-pollutant-emissions-trends-data (visited on 02/07/2022).

Finney, D. L. et al. (2014). "Using cloud ice flux to parametrise large-scale lightning". *Atmospheric Chemistry and Physics* 14.23, pp. 12665–12682. DOI: 10.5194/acp-14-12665-2014.

Finney, D. L. et al. (2018). "A projected decrease in lightning under climate change". *Nature Climate Change* 8.3, pp. 210–213.

Fu, D et al. (2019). *Direct retrieval of isoprene from satellite-based infrared measurements, Nat. Commun., 10, 3811.*

Fu, T.-M. et al. (2007). "Space-based formaldehyde measurements as constraints on volatile organic compound emissions in east and south Asia and implications for ozone". *Journal of Geophysical Research: Atmospheres* 112.D6.

George, L. A., T. M. Hard, and R. J. O'Brien (1999). "Measurement of free radicals OH and HO2 in Los Angeles smog". *Journal of Geophysical Research: Atmospheres* 104.D9, pp. 11643–11655.

Goliff, W. S., W. R. Stockwell, and C. V. Lawson (2013). "The regional atmospheric chemistry mechanism, version 2". *Atmospheric Environment* 68, pp. 174–185. ISSN: 1352-2310. DOI: https://doi.org/10.1016/j.atmosenv.2012.11.038.

Grell, G. A. (1993). "Prognostic Evaluation of Assumptions Used by Cumulus Parameterizations". *Monthly Weather Review* 121.3, pp. 764–787. DOI: 10.1175/1520-0493(1993)121<0764:PEOAUB>2.0.CO;2. eprint: https://doi.org/10.1175/1520-0493(1993)121<0764:PEOAUB>2.0.CO;2.

Grell, G. A. and D. Dévényi (2002). "A generalized approach to parameterizing convection combining ensemble and data assimilation techniques". *Geophysical Research Letters* 29.14, pp. 38–1.

Griffith, S. M. et al. (2016). "Measurements of hydroxyl and hydroperoxy radicals during CalNex-LA: Model comparisons and radical budgets". *Journal of Geophysical Research: Atmospheres* 121.8, pp. 4211–4232. DOI: https://doi.org/10.1002/2015JD024358. eprint: https://agupubs.onlinelibrary.wiley.com/doi/pdf/10.1002/2015JD024358.

Guenther, A. et al. (2006). "Estimates of global terrestrial isoprene emissions using MEGAN (Model of Emissions of Gases and Aerosols from Nature)". *Atmospheric Chemistry and Physics* 6.11, pp. 3181–3210.

Hong, S.-Y., J. Dudhia, and S.-H. Chen (2004). "A revised approach to ice microphysical processes for the bulk parameterization of clouds and precipitation". *Monthly weather review* 132.1, pp. 103–120.

Hudman, R. C. et al. (2007). "Surface and lightning sources of nitrogen oxides over the United States: Magnitudes, chemical evolution, and outflow". *J. Geophys. Res. Atmos.* 112.D12. ISSN: 2156-2202. DOI: 10.1029/2006JD007912.

Huntrieser, H. et al. (2009). "NO_x production by lightning in Hector: first airborne measurements during SCOUT-O3/ACTIVE". *Atmospheric Chemistry and Physics* 9.21, pp. 8377–8412. DOI: 10.5194/acp-9-8377-2009.

Ivatt, P. D. and M. J. Evans (2020). "Improving the prediction of an atmospheric chemistry transport model using gradient-boosted regression trees". *Atmospheric Chemistry and Physics* 20.13, pp. 8063–8082. DOI: 10.5194/acp-20-8063-2020.

Jacob, D. J. (1999). *Introduction to atmospheric chemistry*. Princeton University Press.

Jaeglé, L. et al. (2001). "Chemistry of HOx radicals in the upper troposphere". *Atmospheric Environment* 35.3, pp. 469–489.

Jerrett, M. et al. (2009). "Long-term ozone exposure and mortality". *The New England journal of medicine* 360.11, pp. 1085–1095. ISSN: 0028-4793. DOI: 10.1056/nejmoa0803894.

Jiang, H. and H. Liao (2013). "Projected Changes in NO x Emissions from Lightning as a Result of 2000–2050 Climate Change". *Atmospheric and Oceanic Science Letters* 6.5.

Jiang, Z. et al. (2015). "Regional data assimilation of multi-spectral MOPITT observations of CO over North America". *Atmospheric Chemistry and Physics* 15.12, pp. 6801–6814.

Jourdain, L. et al. (2010). "Lightning NO_x emissions over the USA constrained by TES ozone observations and the GEOS-Chem model". *Atmospheric Chemistry and Physics* 10.1, pp. 107–119. DOI: 10.5194/acp-10-107-2010.

Kain, J. S. (2004). "The KainÄìFritsch Convective Parameterization: An Update". *Journal of Applied Meteorology* 43.1, pp. 170–181. DOI: 10.1175/1520-0450(2004)043<0170:TKCPAU>2.0.CO;2. eprint: https://doi.org/10.1175/1520-0450(2004)043<0170:TKCPAU>2.0.CO;2.

Kain, J. S. and J. M. Fritsch (1990). "A One-Dimensional Entraining/Detraining Plume Model and Its Application in Convective Parameterization". *Journal of the Atmospheric Sciences* 47.23, pp. 2784–2802. DOI: 10.1175/1520-0469(1990)047<2784:AODEPM>2.

0.CO;2. eprint: https://doi.org/10.1175/1520-0469(1990)047<2784:AODEPM>2.0.CO;2.

Kanaya, Y. et al. (2007). "Urban photochemistry in central Tokyo: 1. Observed and modeled OH and HO2 radical concentrations during the winter and summer of 2004". *Journal of Geophysical Research: Atmospheres* 112.D21.

Kaynak, B et al. (2009). "Comparison of weekly cycle of NO2 satellite retrievals and NOx emission inventories for the continental United States". *Journal of Geophysical Research: Atmospheres* 114.D5.

Keller, C. A. et al. (2021). "Global impact of COVID-19 restrictions on the surface concentrations of nitrogen dioxide and ozone". *Atmospheric Chemistry and Physics* 21.5, pp. 3555–3592.

Kharol, S. et al. (2015). "Assessment of the magnitude and recent trends in satellite-derived ground-level nitrogen dioxide over North America". *Atmospheric Environment* 118, pp. 236–245. ISSN: 1352-2310. DOI: https://doi.org/10.1016/j.atmosenv.2015.08.011.

Kota, S. H. et al. (2014). "Evaluation of on-road vehicle CO and NOx National Emission Inventories using an urban-scale source-oriented air quality model". *Atmospheric environment* 85, pp. 99–108.

Lamsal, L. N. et al. (2008). "Ground-level nitrogen dioxide concentrations inferred from the satellite-borne Ozone Monitoring Instrument". *Journal of Geophysical Research: Atmospheres* 113.D16. DOI: https://doi.org/10.1029/2007JD009235. eprint: https://agupubs.onlinelibrary.wiley.com/doi/pdf/10.1029/2007JD009235.

Lamsal, L. N. et al. (2011). "Application of satellite observations for timely updates to global anthropogenic NOxemission inventories". *Geophysical Research Letters* 38.5, n/a–n/a. DOI: 10.1029/2010gl046476.

Lapierre, J. L. et al. (2020). "Observing US regional variability in lightning NO2 production rates". *Journal of Geophysical Research: Atmospheres* 125.5, e2019JD031362.

Laughner, J. L. and R. C. Cohen (2017). "Quantification of the effect of modeled lightning NO_2 on UV–visible air mass factors". *Atmospheric Measurement Techniques* 10.11, pp. 4403–4419. DOI: 10.5194/amt-10-4403-2017.

Laughner, J. L. and Q. Zhu (2018). *CohenBerkeleyLab/BEHR-Core: BEHR Core code*. DOI: 10.5f281/zenodo.998275.

Laughner, J. L., Q. Zhu, and R. C. Cohen (2018a). "The Berkeley High Resolution Tropospheric NO_2 Product". *Earth System Science Data Discussions* 2018, pp. 1–33. DOI: 10.5194/essd-2018-66.

Laughner, J. L. and R. C. Cohen (2019a). "Direct observation of changing NOx lifetime in North American cities". *Science* 366.6466, pp. 723–727.

— (2019b). "Direct observation of changing NOx lifetime in North American cities". *Science* 366.6466, pp. 723–727.

Laughner, J. L., Q. Zhu, and R. C. Cohen (2018b). "The berkeley high resolution tropospheric no 2 product". *Earth System Science Data* 10.4, pp. 2069–2095.

Laughner, J. L., Q. Zhu, and R. C. Cohen (2019). "Evaluation of version 3.0 B of the BEHR OMI NO 2 product". *Atmospheric Measurement Techniques* 12.1, pp. 129–146.

Lelieveld, J. et al. (2004). "On the role of hydroxyl radicals in the self-cleansing capacity of the troposphere". *Atmospheric Chemistry and Physics* 4.9/10, pp. 2337–2344.

Levelt, P et al. (May 2006). "The Ozone Monitoring Instrument". *IEEE T. Geoscience and Remote Sensing* 44, pp. 1093–1101. DOI: 10.1109/TGRS.2006.872333.

Levy, H. (1971). "Normal Atmosphere: Large Radical and Formaldehyde Concentrations Predicted". *Science* 173.3992, pp. 141–143. ISSN: 0036-8075. DOI: 10.1126/science.173.3992.141. eprint: https://science.sciencemag.org/content/173/3992/141.full.pdf.

Liaskos, C. E., D. J. Allen, and K. E. Pickering (2015). "Sensitivity of tropical tropospheric composition to lightning NOx production as determined by replay simulations with GEOS-5". *Journal of Geophysical Research: Atmospheres* 120.16, pp. 8512–8534. DOI: 10.1002/2014JD022987.

Liu, X. et al. (2021). "The potential for geostationary remote sensing of NO 2 to improve weather prediction". *Atmospheric Chemistry and Physics* 21.12, pp. 9573–9583.

Logan, J. A. et al. (1981). "Tropospheric chemistry: A global perspective". *Journal of Geophysical Research: Oceans* 86.C8, pp. 7210–7254.

Lorente, A. et al. (2017). "Structural uncertainty in air mass factor calculation for NO 2 and HCHO satellite retrievals". *Atmospheric Measurement Techniques* 10.3, pp. 759–782.

Lovelock, J. E. (1977). "Methyl chloroform in the troposphere as an indicator of OH radical abundance". *Nature* 267.5606, pp. 32–32.

Lu, K. et al. (2013). "Missing OH source in a suburban environment near Beijing: observed and modelled OH and HO 2 concentrations in summer 2006". *Atmospheric Chemistry and Physics* 13.2, pp. 1057–1080.

Lu, K. et al. (2012). "Observation and modelling of OH and HO 2 concentrations in the Pearl River Delta 2006: a missing OH source in a VOC rich atmosphere". *Atmospheric chemistry and physics* 12.3, pp. 1541–1569.

Lu, Z. et al. (2015). "Emissions of nitrogen oxides from US urban areas: estimation from Ozone Monitoring Instrument retrievals for 2005§?2014". *Atmospheric Chemistry and Physics* 15.18, pp. 10367–10383. DOI: 10.5194/acp-15-10367-2015.

Luo, C., Y. Wang, and W. J. Koshak (2017). "Development of a self-consistent lightning NOx simulation in large-scale 3-D models". *Journal of Geophysical Research: Atmospheres* 122.5, pp. 3141–3154. DOI: 10.1002/2016JD026225. eprint: https://agupubs.onlinelibrary.wiley.com/doi/pdf/10.1002/2016JD026225.

Mak, H. W. L. et al. (2018). "Improved Satellite Retrieval of Tropospheric NO2 Column Density via Updating of Air Mass Factor (AMF): Case Study of Southern China". *Remote Sensing* 10.11. ISSN: 2072-4292. URL: http://www.mdpi.com/2072-4292/10/11/1789.

Manisalidis, I. et al. (2020). "Environmental and health impacts of air pollution: a review". *Frontiers in public health*, p. 14.

Mao, J. et al. (2010). "Atmospheric oxidation capacity in the summer of Houston 2006: Comparison with summer measurements in other metropolitan studies". *Atmospheric*

Environment 44.33, pp. 4107–4115. ISSN: 1352-2310. DOI: https://doi.org/10.1016/j.atmosenv.2009.01.013.

Mao, J. et al. (2021). "Global Impact of Lightning-Produced Oxidants". *Geophysical Research Letters* 48.21, e2021GL095740.

Marais, E. A. et al. (2014). "Improved model of isoprene emissions in Africa using Ozone Monitoring Instrument (OMI) satellite observations of formaldehyde: implications for oxidants and particulate matter". *Atmospheric Chemistry and Physics* 14.15, pp. 7693–7703.

Martin, R. V., A. M. Fiore, and A. Van Donkelaar (2004). "Space-based diagnosis of surface ozone sensitivity to anthropogenic emissions". *Geophysical Research Letters* 31.6.

Martin, R. et al. (2007). "Space-based constraints on the production of nitric oxide by lightning". *J. Geophys. Res. Atmos.* 112. DOI: 10.1029/2006JD007831.

Martinez, M et al. (2003). "OH and HO2 concentrations, sources, and loss rates during the Southern Oxidants Study in Nashville, Tennessee, summer 1999". *Journal of Geophysical Research: Atmospheres* 108.D19.

Mauderly, J. L. and J. C. Chow (2008). "Health effects of organic aerosols". *Inhalation toxicology* 20.3, pp. 257–288.

Mauldin III, R. et al. (1998). "OH measurements during the First Aerosol Characterization Experiment (ACE 1): Observations and model comparisons". *Journal of Geophysical Research: Atmospheres* 103.D13, pp. 16713–16729.

McDonald, B. C. et al. (2018). "Volatile chemical products emerging as largest petrochemical source of urban organic emissions". *Science* 359.6377, pp. 760–764.

Michoud, V. et al. (2012). "Radical budget analysis in a suburban European site during the MEGAPOLI summer field campaign". *Atmospheric Chemistry and Physics* 12.24, pp. 11951–11974.

Migliorini, S., C. Piccolo, and C. D. Rodgers (2008). "Use of the information content in satellite measurements for an efficient interface to data assimilation". *Monthly weather review* 136.7, pp. 2633–2650.

Millet, D. B. et al. (2008). "Spatial distribution of isoprene emissions from North America derived from formaldehyde column measurements by the OMI satellite sensor". *Journal of Geophysical Research: Atmospheres* 113.D2.

Miyazaki, K., H. Eskes, and K. Sudo (2012). "Global NO_x emissions estimates derived from an assimilation of OMI tropospheric NO_2 columns". *Atmos. Chem. Phys.* 12, pp. 2263–2288. DOI: 10.5194/acp-12-2263-2012.

Miyazaki, K. et al. (2014). "Global lightning NO_x production estimated by an assimilation of multiple satellite data sets". *Atmos. Chem. Phys.* 14, pp. 3277–3305. DOI: 10.5194/acp-14-3277-2014.

Miyazaki, K. et al. (2017). "Decadal changes in global surface NO x emissions from multi-constituent satellite data assimilation". *Atmospheric Chemistry and Physics* 17.2, pp. 807–837.

Mizzi, A. P. et al. (2016). "Assimilating compact phase space retrievals of atmospheric composition with WRF-Chem/DART: a regional chemical transport/ensemble Kalman filter data assimilation system". *Geoscientific Model Development* 9.3, pp. 965–978.

Montzka, S. et al. (2000). "New observational constraints for atmospheric hydroxyl on global and hemispheric scales". *Science* 288.5465, pp. 500–503.

Murphy, J. et al. (2006). "The weekend effect within and downwind of Sacramento: Part 2. Observational evidence for chemical and dynamical contributions". *Atmospheric Chemistry and Physics Discussions* 6.6, pp. 11971–12019.

Murray, L. T. (2016). "Lightning NO x and impacts on air quality". *Current Pollution Reports* 2.2, pp. 115–133.

Murray, L. T., J. A. Logan, and D. J. Jacob (2013). "Interannual variability in tropical tropospheric ozone and OH: The role of lightning". *Journal of Geophysical Research: Atmospheres* 118.19, pp. 11–468.

Nault, B. A. et al. (2017). "Lightning NO_x Emissions: Reconciling Measured and Modeled Estimates With Updated NO_x Chemistry". *Geophys. Res. Lett.* ISSN: 1944-8007. DOI: 10.1002/2017GL074436.

Nightingale, J. et al. (2018). "Quality assurance framework development based on six new ECV data products to enhance user confidence for climate applications". *Remote Sensing* 10.8, p. 1254.

Nisbet, E. G., E. J. Dlugokencky, and P. Bousquet (2014). "Methane on the Rise - Again". *Science* 343.6170, pp. 493–495. DOI: 10.1126/science.1247828. eprint: https://www.science.org/doi/pdf/10.1126/science.1247828.

Olson, J. et al. (2012). "An analysis of fast photochemistry over high northern latitudes during spring and summer using in-situ observations from ARCTAS and TOPSE". *Atmospheric Chemistry and Physics* 12.15, pp. 6799–6825.

O'Neill, B. C. et al. (2016). "The scenario model intercomparison project (ScenarioMIP) for CMIP6". *Geoscientific Model Development* 9.9, pp. 3461–3482.

Ott, L. E. et al. (2010). "Production of lightning NOxand its vertical distribution calculated from three-dimensional cloud-scale chemical transport model simulations". *Journal of Geophysical Research* 115.D4. DOI: 10.1029/2009jd011880.

Palmer, P. I. et al. (2001). "Air mass factor formulation for spectroscopic measurements from satellites: Application to formaldehyde retrievals from the Global Ozone Monitoring Experiment". *Journal of Geophysical Research: Atmospheres* 106.D13, pp. 14539–14550.

Palmer, P. I. et al. (2003). "Mapping isoprene emissions over North America using formaldehyde column observations from space". *Journal of Geophysical Research: Atmospheres* 108.D6.

Perring, A., S. Pusede, and R. Cohen (2013). "An observational perspective on the atmospheric impacts of alkyl and multifunctional nitrates on ozone and secondary organic aerosol". *Chemical reviews* 113.8, pp. 5848–5870.

Pickering, K. E. et al. (2016). "Estimates of lightning NOx production based on OMI NO2 observations over the Gulf of Mexico". *J. Geophys. Res. Atmos.* 121.14. 2015JD024179, pp. 8668–8691. ISSN: 2169-8996. DOI: 10.1002/2015JD024179.

Pollack, I. B. et al. (2016). "Airborne quantification of upper tropospheric NOx production from lightning in deep convective storms over the United States Great Plains". *Journal of Geophysical Research: Atmospheres* 121.4, pp. 2002–2028. DOI: 10.1002/2015JD023941.

Price, C., J. Penner, and M. Prather (1997). "NOx from lightning: 1. Global distribution based on lightning physics". *Journal of Geophysical Research: Atmospheres* 102.D5, pp. 5929–5941. DOI: 10.1029/96JD03504.

Price, C. and D. Rind (1992). "A simple lightning parameterization for calculating global lightning distributions". *Journal of Geophysical Research: Atmospheres* 97.D9, pp. 9919–9933. DOI: 10.1029/92JD00719. eprint: https://agupubs.onlinelibrary.wiley.com/doi/pdf/10.1029/92JD00719.

Ren, X et al. (2012). "Airborne intercomparison of HO x measurements using laser-induced fluorescence and chemical ionization mass spectrometry during ARCTAS". *Atmospheric Measurement Techniques* 5.8, pp. 2025–2037.

Ren, X. et al. (2003). "HOx concentrations and OH reactivity observations in New York City during PMTACS-NY2001". *Atmospheric Environment* 37.26, pp. 3627–3637. ISSN: 1352-2310. DOI: https://doi.org/10.1016/S1352-2310(03)00460-6.

Ren, X. et al. (2006). "Behavior of OH and HO2 in the winter atmosphere in New York City". *Atmospheric Environment* 40, pp. 252–263.

Ren, X. et al. (2013). "Atmospheric oxidation chemistry and ozone production: Results from SHARP 2009 in Houston, Texas". *Journal of Geophysical Research: Atmospheres* 118.11, pp. 5770–5780.

Riahi, K. et al. (2017). "The shared socioeconomic pathways and their energy, land use, and greenhouse gas emissions implications: an overview". *Global environmental change* 42, pp. 153–168.

Rohrer, F. and H. Berresheim (2006). "Strong correlation between levels of tropospheric hydroxyl radicals and solar ultraviolet radiation". *Nature* 442.7099, pp. 184–187.

Romps, D. M. et al. (2014). "Projected increase in lightning strikes in the United States due to global warming". *Science* 346.6211, pp. 851–854. ISSN: 0036-8075. DOI: 10.1126/science.1259100. eprint: http://science.sciencemag.org/content/346/6211/851.full.pdf.

Russell, A. R., L. C. Valin, and R. C. Cohen (2012). "Trends in OMI NO_2 observations over the United States: effects of emission control technology and the economic recession". *Atmospheric Chemistry and Physics* 12.24, pp. 12197–12209. DOI: 10.5194/acp-12-12197-2012.

Russell, A. R. et al. (2010). "Space-based constraints on spatial and temporal patterns of NO x emissions in California, 2005- 2008". *Environmental science & technology* 44.9, pp. 3608–3615.

Sanchez, D. et al. (2018). "Intercomparison of OH and OH reactivity measurements in a high isoprene and low NO environment during the Southern Oxidant and Aerosol Study (SOAS)". *Atmospheric Environment* 174, pp. 227–236. ISSN: 1352-2310. DOI: https://doi.org/10.1016/j.atmosenv.2017.10.056.

Schumann, U. and H. Huntrieser (2007). "The global lightning-induced nitrogen oxides source". *Atmospheric Chemistry and Physics* 7.14, pp. 3823–3907. DOI: 10.5194/acp-7-3823-2007.

Seto, K. C. et al. (2014). "Human settlements, infrastructure and spatial planning".

Shirley, T. R. et al. (2006). "Atmospheric oxidation in the Mexico City Metropolitan Area (MCMA) during April 2003". *Atmospheric Chemistry and Physics* 6.9, pp. 2753–2765. DOI: 10.5194/acp-6-2753-2006.

Silvern, R. F. et al. (2018). "Observed NO/NO2 Ratios in the Upper Troposphere Imply Errors in NO-NO2-O3 Cycling Kinetics or an Unaccounted NOx Reservoir". *Geophysical Research Letters* 45.9, pp. 4466–4474. DOI: 10.1029/2018GL077728. eprint: https://agupubs.onlinelibrary.wiley.com/doi/pdf/10.1029/2018GL077728.

Singh, H. B. (1977). "Preliminary estimation of average tropospheric HO concentrations in the northern and southern hemispheres". *Geophysical Research Letters* 4.10, pp. 453–456. DOI: https://doi.org/10.1029/GL004i010p00453. eprint: https://agupubs.onlinelibrary.wiley.com/doi/pdf/10.1029/GL004i010p00453.

Steinfeld, J. I. (1998). "Atmospheric chemistry and physics: from air pollution to climate change". *Environment: Science and Policy for Sustainable Development* 40.7, pp. 26–26.

Stone, D., L. K. Whalley, and D. E. Heard (2012). "Tropospheric OH and HO 2 radicals: field measurements and model comparisons". *Chemical Society Reviews* 41.19, pp. 6348–6404.

Sun, W. et al. (2020). "Development and application of the WRFDA-Chem three-dimensional variational (3DVAR) system: aiming to improve air quality forecasting and diagnose model deficiencies". *Atmospheric Chemistry and Physics* 20.15, pp. 9311–9329.

Tan, Z. et al. (2019a). "Daytime atmospheric oxidation capacity in four Chinese megacities during the photochemically polluted season: a case study based on box model simulation". *Atmospheric Chemistry and Physics* 19.6, pp. 3493–3513.

Tan, Z. et al. (2019b). "Experimental budgets of OH, HO 2, and RO 2 radicals and implications for ozone formation in the Pearl River Delta in China 2014". *Atmospheric chemistry and physics* 19.10, pp. 7129–7150.

Thornton, J. et al. (2002). "Ozone production rates as a function of NOx abundances and HOx production rates in the Nashville urban plume". *Journal of Geophysical Research: Atmospheres* 107.D12, ACH–7.

Tippett, M. K. and W. J. Koshak (2018). "A Baseline for the Predictability of U.S. Cloud-to-Ground Lightning". *Geophysical Research Letters* 0.0. DOI: 10.1029/2018GL079750. eprint: https://agupubs.onlinelibrary.wiley.com/doi/pdf/10.1029/2018GL079750.

Toon, O. B. et al. (2016). "Planning, implementation, and scientific goals of the Studies of Emissions and Atmospheric Composition, Clouds and Climate Coupling by Regional Surveys (SEAC4RS) field mission". *Journal of Geophysical Research: Atmospheres* 121.9, pp. 4967–5009. DOI: 10.1002/2015JD024297. eprint: https://agupubs.onlinelibrary.wiley.com/doi/pdf/10.1002/2015JD024297.

Tost, H., P. Jöckel, and J. Lelieveld (2007). "Lightning and convection parameterisations ndash; uncertainties in global modelling". *Atmospheric Chemistry and Physics* 7.17, pp. 4553–4568. DOI: 10.5194/acp-7-4553-2007.

Travis, K. R. et al. (2016). "Why do models overestimate surface ozone in the Southeast United States?" *Atmos. Chem. Phys.* 16.21, pp. 13561–13577. DOI: 10.5194/acp-16-13561-2016.

Valin, L. C. et al. (2016). "The role of OH production in interpreting the variability of CH2O columns in the southeast U.S." *Journal of Geophysical Research: Atmospheres* 121.1, pp. 478–493. DOI: https://doi.org/10.1002/2015JD024012. eprint: https://agupubs.onlinelibrary.wiley.com/doi/pdf/10.1002/2015JD024012.

Valin, L., A. Russell, and R. Cohen (2013). "Variations of OH radical in an urban plume inferred from NO2 column measurements". *Geophysical Research Letters* 40.9, pp. 1856–1860.

Vinken, G. et al. (2014). "Worldwide biogenic soil NO x emissions inferred from OMI NO 2 observations". *Atmospheric Chemistry and Physics* 14.18, pp. 10363–10381.

Vira, J and M Sofiev (2012). "On variational data assimilation for estimating the model initial conditions and emission fluxes for short-term forecasting of SOx concentrations". *Atmospheric Environment* 46, pp. 318–328.

Warneke, C. et al. (2012). "Multiyear trends in volatile organic compounds in Los Angeles, California: Five decades of decreasing emissions". *Journal of Geophysical Research: Atmospheres* 117.D21.

Wells, K. C. et al. (2020). "Satellite isoprene retrievals constrain emissions and atmospheric oxidation". *Nature* 585.7824, pp. 225–233.

Wennberg, P. et al. (1998). "Hydrogen radicals, nitrogen radicals, and the production of O3 in the upper troposphere". *science* 279.5347, pp. 49–53.

Whalley, L. K. et al. (2018). "Understanding in situ ozone production in the summertime through radical observations and modelling studies during the Clean air for London project (ClearfLo)". *Atmospheric Chemistry and Physics* 18.4, pp. 2547–2571.

Wolfe, G. M. et al. (2019). "Mapping hydroxyl variability throughout the global remote troposphere via synthesis of airborne and satellite formaldehyde observations". *Proceedings of the National Academy of Sciences* 116.23, pp. 11171–11180. ISSN: 0027-8424. DOI: 10.1073/pnas.1821661116. eprint: https://www.pnas.org/content/116/23/11171.full.pdf.

Wong, J., M. C. Barth, and D. Noone (2013). "Evaluating a lightning parameterization based on cloud-top height for mesoscale numerical model simulations". *Geoscientific Model Development* 6.2, pp. 429–443. DOI: 10.5194/gmd-6-429-2013.

Yienger, J. and H Levy (1995). "Empirical model of global soil-biogenic NOχ emissions". *Journal of Geophysical Research: Atmospheres* 100.D6, pp. 11447–11464.

Zare, A. et al. (2018). "A comprehensive organic nitrate chemistry: insights into the lifetime of atmospheric organic nitrates". *Atmospheric Chemistry and Physics* 18.20, pp. 15419–15436. DOI: 10.5194/acp-18-15419-2018.

Zhao, C. et al. (2009). "Summertime impact of convective transport and lightning NO_x production over North America: modeling dependence on meteorological simulations". *Atmospheric Chemistry and Physics* 9.13, pp. 4315–4327. DOI: 10.5194/acp-9-4315-2009.

Zhu, L. et al. (2017). "Long-term (2005–2014) trends in formaldehyde (HCHO) columns across North America as seen by the OMI satellite instrument: Evidence of changing emissions of volatile organic compounds". *Geophysical Research Letters* 44.13, pp. 7079–7086.

Zhu, Q. and J. L. Laughner (2019). *CohenBerkeleyLab/WRF-Chem-R2SMH: WRF-Chem code*. DOI: 10.5281/zenodo.2585381.

Zhu, Q. (Aug. 2021). *qdzhu/ML-Pred-Urban-OH: First release*. Version v1.0. DOI: 10.5281/zenodo.5296044.

Zhu, Q., J. Laughner, and R. Cohen (2019a). *Berkeley High Resolution (BEHR) OMI NO2 v3.0C - Gridded pixels, daily profiles, v3, UC Berkeley Dash, Dataset*. DOI: 10.6078/D16X1T.

— (2019b). *Berkeley High Resolution (BEHR) OMI NO2 v3.0C - Native pixels, daily profiles, UC Berkeley Dash, Dataset*. DOI: 10.6078/D1BM2B.

Zhu, Q., J. L. Laughner, and R. C. Cohen (2019c). "Lightning NO 2 simulation over the contiguous US and its effects on satellite NO 2 retrievals". *Atmospheric Chemistry and Physics* 19.20, pp. 13067–13078.

— (Aug. 2021). *Supporting data for "Direct observation of changing NOx lifetime in North American cities"*. DOI: https://doi.org/10.6078/D1FM75.

— (2022a). "Combining Machine Learning and Satellite Observations to Predict Spatial and Temporal Variation of near Surface OH in North American Cities". *Environmental Science & Technology*.

— (2022b). "Estimate of OH trends over one decade in North American cities". *Proceedings of the National Academy of Sciences* 119.16, e2117399119.

Appendix A

Supplemental material for "Lightning NO_2 simulation over the Contiguous US and its effects on satellite NO_2 retrievals"

The chapter was adapted from the supplement of: Q. Zhu, J. L. Laughner, and R. C. Cohen (2019c). "Lightning NO 2 simulation over the contiguous US and its effects on satellite NO 2 retrievals". *Atmospheric Chemistry and Physics* 19.20, pp. 13067–13078

A.1 Comparison between ENTLN and NLDN

While both NLDN and ENTLN have high detection efficiency (>90%) for CG flashes, we recognize that ENTLN observes more CG flashes than NLDN. Shown in Fig. A.1, we average the flashes density over CONUS both from ENTLN and NLDN between May 13 to June 23 2012. The daily averaged CG flash density from ENTLN is tightly correlated with those from NLDN with slope of 1.5. It can be explained by discrepancy in the grouping criterions applied to produce flash counts between NLDN and ENTLN. ENTLN groups all pulses within 10 km and 700 ms of each other as a single flash, and NLDN uses 10 km and 1000 ms as the threshold. In consequence, for the same amount of CG pulses measured by both lightning observation network, ENTLN produces more flashes than NLDN according to the grouping algorithm.

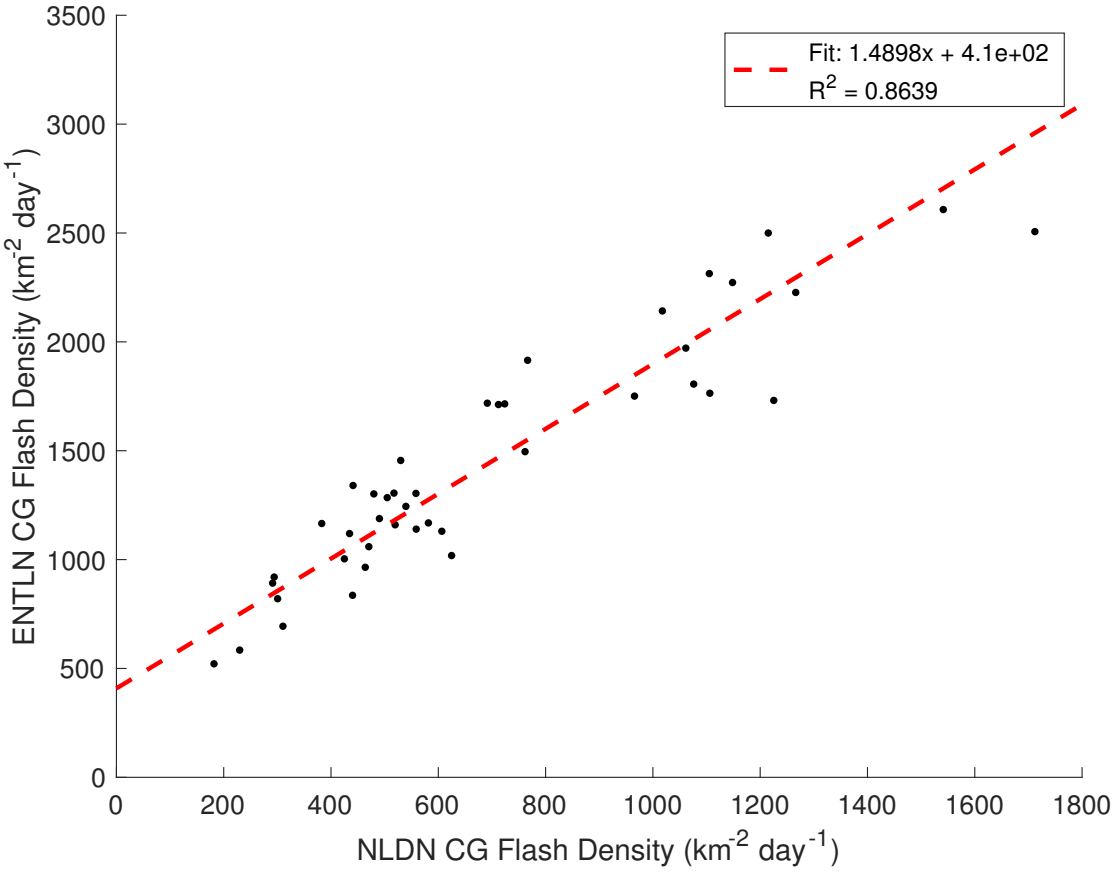

Figure A.1: Comparison between CG flash density per day observed by NLDN and ENTLN. The data spans May 13 to June 23, 2012.

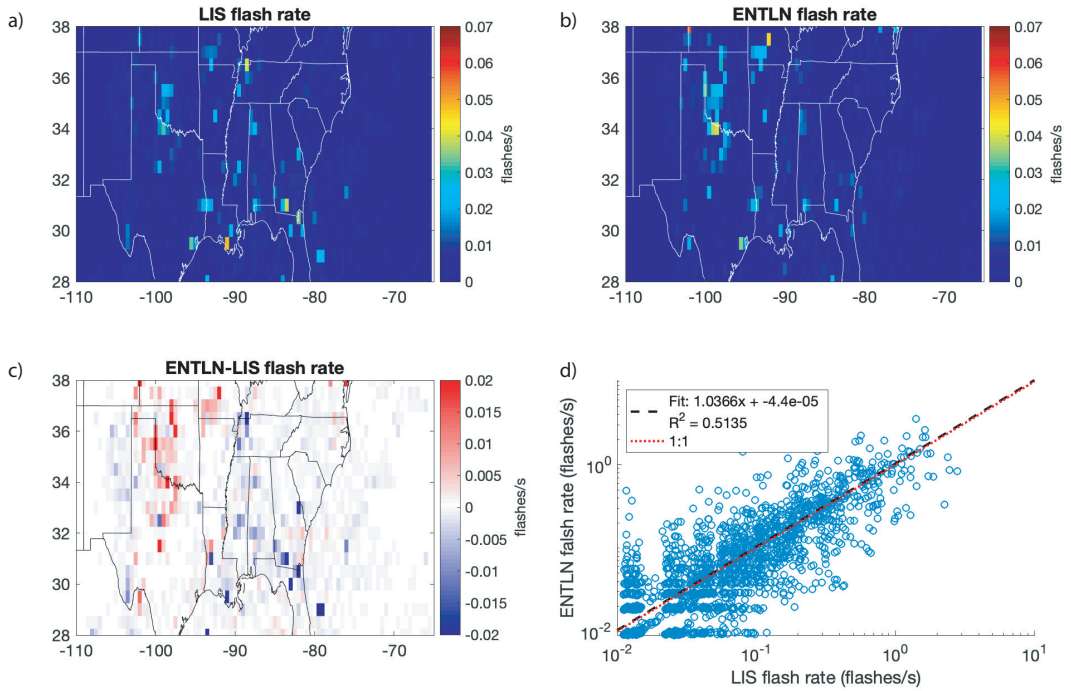

Figure A.2: Comparison between flash rates observed by ENTLN and Lightning Imaging Sensor (LIS). ENTLN data is matched to corrected LIS flashes both in time and space during May 13-June 23, 2012, and both datasets are summed onto 0.5°x 0.5°grid spacing. **(a,b)** shows the spatial pattern of lightning flash rates measured by LIS **(a)** and ENTLN **(b)**. The plot region covers 20°N - 38°N and 130°W - 65°W. **(c,d)** are corresponding absolute difference and scatter plots between LIS and ENTLN. LIS data is corrected using the detection efficiency from citetcecil14.

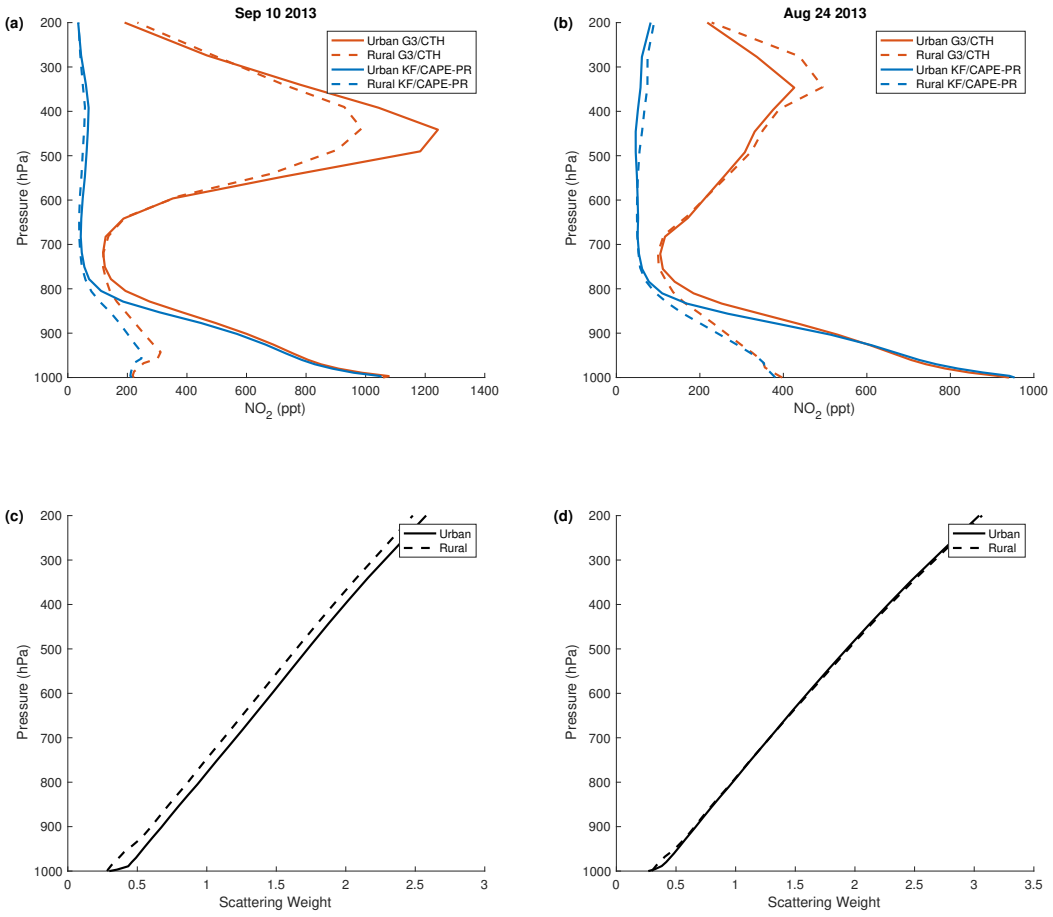

Figure A.3: The a priori NO_2 vertical profiles **(a, b)** and scattering weights **(c, d)** on Sep 10 and Aug 24 2013 averaged over all urban (solid) or rural (dashed) grid cells in SE US. The NO_2 profiles from WRF-Chem using G3/CTH parameterization are in red, those from KF/CAPE-PR parameterization are in blue.

	No lightning	400 mol NO $flash^{-1}$	500 mol NO $flash^{-1}$	665 mol NO $flash^{-1}$
CONUS	0.92×10^{15}	0.44×10^{15}	0.41×10^{15}	0.44×10^{15}
Urban	1.30×10^{15}	0.89×10^{15}	0.91×10^{15}	1.10×10^{15}
Non-Urban	0.90×10^{15}	0.41×10^{15}	0.37×10^{15}	0.39×10^{15}

Table A.1: The root-mean-square errors (RMSE) in unit of mole cm^{-2} between observed and modeled NO_2 VCD using WRF-Chem with varied LNO_x production rates (0, 400, 500, 665 mol NO $flash^{-1}$). Urban areas are selected where NO_2 columns are at top 5% calculated from WRF-Chem without lightning. Non-urban areas are CONUS excluding urban areas.

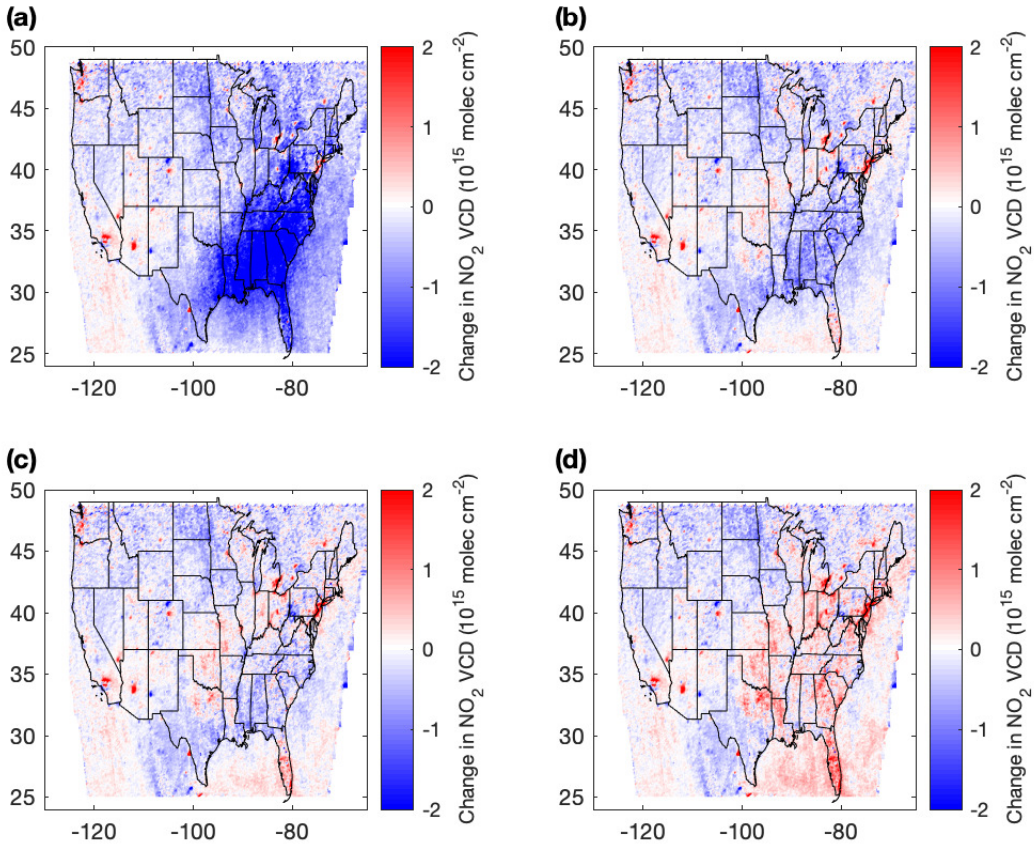

Figure A.4: Difference in NO_2 VCD between BEHR retrievals and WRF-Chem **(a)** without LNO_x and with LNO_x production rate of **(b)** 400 mol NO flash^{-1}, **(c)** 500 mol NO flash^{-1} and **(d)** 665 mol NO flash^{-1}.

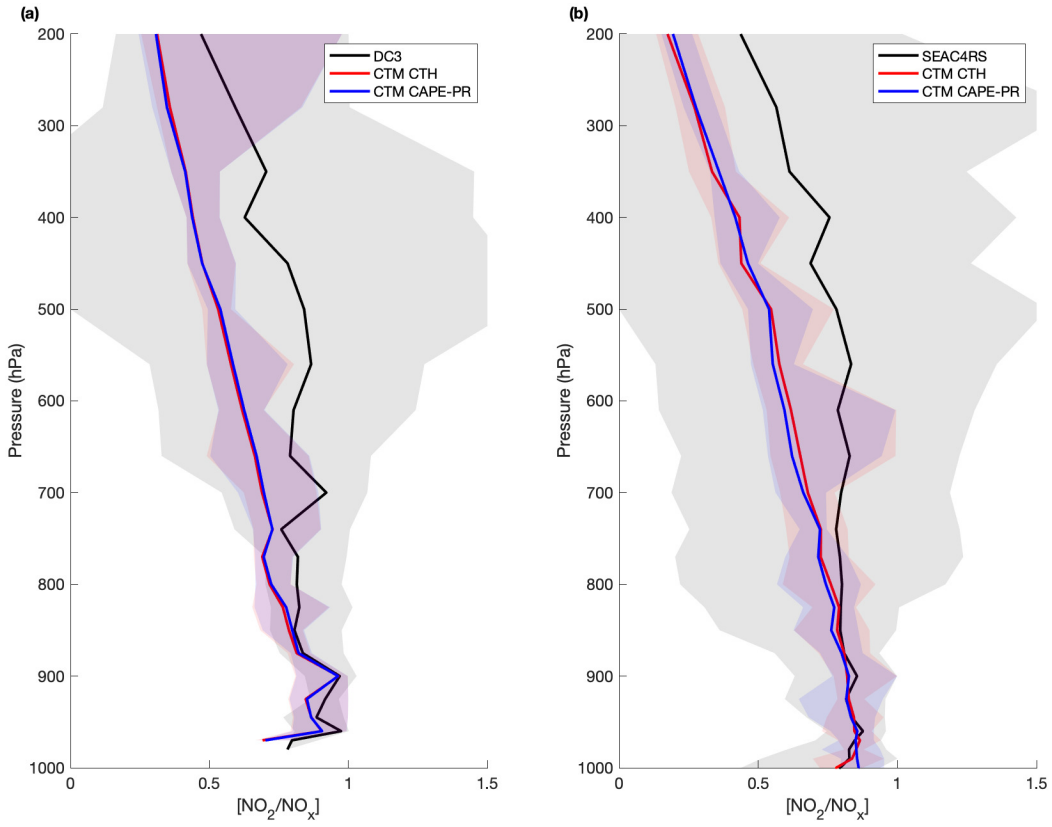

Figure A.5: Comparison of WRF-Chem and aircraft [NO_2/NO_x] profiles from the **(a)** DC3, **(b)** SEAC4RS campaigns.The solid line is the median of all profiles and the shaded areas are between 10th and 90th percentiles for each binned level. Aircraft measurements are shown in black, WRF-Chem using CTH lightning parameterization in red and WRF-Chem using CAPE-PR lightning parameterization in blue.

Appendix B

Supplemental material for "Combining machine learning and satellite observations to predict spatial and temporal variation of near surface OH in North American cities"

The chapter was adapted from the supplement of: Q. Zhu, J. L. Laughner, and R. C. Cohen (2022a). "Combining Machine Learning and Satellite Observations to Predict Spatial and Temporal Variation of near Surface OH in North American Cities". *Environmental Science & Technology*

B.1 Design of the gradient boosted tree model

The gradient-boosted tree model is a supervised machine learning model and is trained to optimize the predictions when the ground truths are known. The model consists of three elements. An objective function is defined as the goal of optimization; the decision tree is used as the weak learner to make the prediction; an additive algorithm is applied to to construct a sequence of weak learners in order to minimize the objective function.

The objective function composes a loss function (L) and a regularization term (Ω).

$$Obj(\theta) = L(\theta) + \Omega(\theta) = \sum_i (y_i - \hat{y_i})^2 + \sum (\theta_j)^2 \tag{B.1}$$

$$y = f(x_1, x_2, ...x_n) \tag{B.2}$$

Where $x_j(j = 1, 2, ..n)$ represents the set of features selected in Sect.2.1.2, y denotes the predicted near surface OH from this ML configuration, and $\hat{y}$ corresponds the near surface OH from WRF-Chem marked as ground truths. The loss function is the sum of squared error. An L2 regularization term, $\Omega(\theta)$, is added to constrain the complexity of the model and avoid overfitting.

A weak learner is defined as a simplified framework whose performance is better than random chance and can handle the prediction for partial observations. We use the regression decision tree to serve as a weak learner in the model infrastructure. The root node contains the full training data sets, and then we grow the tree by splitting the nodes and assign them the score on the corresponding child nodes. The splitting criteria is determined to achieve the largest reduction on the objective function.

The outcome of the gradient boosted tree model is an assemblage of decision trees. We use the additive model algorithm to augment the number of decision trees. At each boosting iteration, the gradient descent is calculated in the function space, which orients construction of a new tree to reduce the objective function. The new tree is then added to the existing sequence of trees in an effort to improve the final output of the model. The construction is repeated until it hits the stopping criteria.

The choice of hyperparameters are the determinants of model performance. Hyperparameters are configuration variables that are external to the model and whose value cannot be estimated from data. Our model configurations involves hyperparameters such as the number of trees, the depth, number of leaves. To tune the hyperparameters, we define a range of candidates for each hyperparameter, and enumerate all possible combinations. Those combinations are tested using the five-fold cross validation technique to determine the best candidate. The details are described in Supp.S2.

B.2 Cross Validation

The ML model performance is affected by the hyperparameters, which are prescribed externally. In our gradient boosted model, we define 50 boosted trees in total and each tree shares the same configuration which is determined by several key hyperparamters. For instance, *max_depth* defines the maximum depth and it controls the complexity of the tree, *min_child_weight* corresponds to the minimum sum of instance weight, and similarly *gamma* is the minimum loss reduction, both of which decide whether or not to make a further partition on this child node. *eta* is the learning rate. Shown in Table B.3, we define a physical reasonable range for each hyperparamter, and list out all possible combinations of these hyperparameters.

We implement a five-fold cross validation to decide the best combination of hyperparameters. The general procedure is as follows. First, we randomly split the training data sets into five

groups of approximately equal size. Within each group, we hold out this group as a validation data set and take the remaining groups as a training data set. We then retrain the model on the selected training set and evaluate this model performance on the validation data set. The step is repeated five times, and we take the average evaluation score and assign this score to selected hyperparameters. The best combination of the hyperparameters are determined by the highest evaluation score, and we present the finalized values in Table B.3.

B.3 Uncertainty analysis

Here we define the uncertainty (u) as the normalized standard deviations. We also assume the errors are independent and uncorrelated across observations and are drawn from a zero-centered normal distribution.

$$\vec{\sigma} = u \times \vec{x_{true}} \tag{B.3}$$

$$\vec{\epsilon} \sim \mathcal{N}(\vec{x_{true}}, \sigma^2) \tag{B.4}$$

$$\vec{x_{noise}} = \vec{x_{true}} + \epsilon \tag{B.5}$$

Specifically, for each feature (x_{true}), we prescribe an uncertainty (u) ranging from 0% to 100%, draw an error (ϵ) from a normal distribution determined by the uncertainty level, and add the error to the original feature sets from WRF-Chem. The ML model is again trained on noisy features (x_{noise}) and its performance is compared against the model trained on noise free feature sets.

Shown in Figure B.3(a), the uncertainty in features sets inevitably degrade the model performance reflected by the increasing RMSE. However, there is a considerable variation in terms of the model sensitivity to error propogation from different features. Uncertainty from the NO_2 column leads to the largest increase in RMSE, a 50% increase from $\sim$2 to $\sim$3$\times10^6$ OH molec cm^{-3}. The uncertainty reaches a limit when the uncertainty in NO_2 column exceeds 50%. The second largest effect results from HCHO column. The RMSE increases by about 30% from 2.1$\times10^6$ molec cm^{-3} to 2.7$\times10^6$ molec cm^{-3} for uncertainty level ranging from 0% to 40%. The remaining features lead to a slight increase in RMSE individually, each less than 10%.

Given that the ML model performance is sensitive to the uncertainties from both NO_2 and HCHO columns, we take a step further to account for uncertainties from both features simultaneously shown in Figure B.3(b). Note that the uncertainty in BEHR NO_2 columns is 30% and the uncertainty in QA4ECV HCHO column is 60%, those uncertainties propagate through the model configuration and result in a model performance quantified by the RMSE of 3.2$\times10^6$ molec cm^{-3}.

B.4 ML training and feature sets

Besides a "General" system where a single ML model is trained on all of the urban WRF-Chem data, we train a separate ML model for each of the 49 cities and call it "City" system. The "City-WRF" OH predictions are made from the series of ML models from "City" system and the input features exclusively from WRF-Chem. Table B.4 summarizes the differences between the OH prediction sets.

B.5 Validation of OH predictions using ML characteristics ("City-WRF")

One advantage of the gradient-boosted tree model is that we can check which input features have the most influence on the output OH concentrations. We can use this as a qualitative check on model performance by verifying that the relative importance of the input features reflects the current understanding of which physical processes should govern the OH in different urban environments.

This feature importance is calculated explicitly for each feature, allowing features to be ranked and compared to each other. The importance is calculated by the amount that each feature split point improves the performance measure, weighted by the number of observations the node is responsible for. The series of features importance are normalized to unity to yield the feature relative importance. The more a feature is used to make key decisions in the construction of the boosted trees, the higher its relative importance. While the model infrastructure remains unchanged, the feature relative importance reflects the difference in the training data sets sampled from various urban environments. Therefore, it is an explicit measure of how important this feature is to capture the OH variability at the target urban environment.

We start with the General-WRF system. Since it samples a variety of OH chemical conditions, the relative feature importance represents the general OH drivers over US cities. Shown in Fig. B.4, the largest contribution, 42% of the loss reduction is assigned to the NO_2 column. It combines with the HCHO column to gain 70% of the reduction on the objective function.

Compared to the generalized model, the City-WRF systems show physically plausible differences in the relative feature importance between different cities. Figure B.5 shows the normalized feature importance extracted from two ML models trained on data sampled over Chicago and Atlanta, respectively. Both yield a good representation of the simulated OH; each of them is capable of explaining $> 70\%$ of the OH variability. The Chicago ML model weights heavily on $J(O^1D)$ and NO_2 column, and it implies that the OH variability is predominantly driven by the ozone photolysis and NO_x chemistry. In contrast, Atlanta imposes

a much larger importance on the HCHO column feature. The HCHO column has 7% relative importance in the Chicago model whereas in Atlanta, the contribution is 27%, reflecting the variation in the role of VOC on OH chemistry in the two cities.

The distinction in OH drivers reflected from feature relative importance is also verified by the distributions of features from both cities shown in Fig. B.6. Among six features, both cities show similar distribution in NO_2 column, water vapor and temperature. Pressure over Chicago is consistently higher than Atlanta due to lower elevation. $J(O^1D)$ presents an opposite relationship and the average $J(O^1D)$ is higher over Atlanta due to lower latitude, however, the variance of $J(O^1D)$ is similar for both cities. The largest discrepancy attributes to HCHO column, a proxy for abundant VOC oxidation in the HO_x cycle. Atlanta exhibits higher HCHO column as well as a wider variability of HCHO, indicating that a large variability of VOC chemistry exists on a day to day basis in Atlanta.

B.6 Comparison of satellite constrained OH with WRF-Chem simulated OH

Figure B.7(a) shows the predicted OH from ML ("General-Satellite") and WRF-Chem simulations, respectively, both of which are segregated into the same distance bins determined by the distance between the grid and the city center. We found surface OH predicted using OMI observations are consistently lower than those from WRF-Chem. Near the city center, WRF-Chem overestimates the surface OH, which we attribute to the overestimate in NO_2 column. Figure B.7(b) and (c) show the corresponding spatial pattern of HCHO column and NO_2 column averaged over 49 cities from both WRF-Chem and OMI observations ranging from 2005 to 2014. We note that WRF-Chem yields a good agreement of HCHO column on average regardless of the distance from the city center. There is no gradient of HCHO column between urban center and the surrounding areas. As a contrast, the discrepancy observed in NO_2 columns between model simulation and satellite observation is distinct; WRF-Chem consistently overestimates the NO_2 columns by up to 50% near the city centers. The negative gradient of NO_2 column between city and the surrounding areas reflects the NO_x emission patterns since the largest contributors are anthropogenic emissions clustered near the city center. Therefore, the overestimate in WRF-chem NO_2 column is associated with the overestimate of anthropogenic NEI NO_x emissions prescibed in the model simulation. This finding is consistent with the results reported in Kota et al. (2014).

The difference in OH and NO_2 column also reflect the non-linearity of OH chemistry. The OH response to overestimate in NO_2 is clearly buffered: WRF-Chem shows on average 10% larger surface OH while the concurrent NO_2 column is 50% larger than the satellite observations. Further away from the city center there is better agreement between OH predictions and WRF-Chem simulations, and coinciding better agreement in NO_2 columns.

Campaign	City	R^2	Slope
CALNEX	LA	0.74	1.55
MEGAPOLI	Paris	0.62	1.94
BERLIOZ	Berlin	0.81	2.0
PRIDE-PRD2006	PRD*	0.81	4.0
CAREBeijing2006	Beijing	0.73	4.0

*Pearl River Delta

Table B.1: Summary of linear regression results between OH and $J(O^1D)$ from the in-situ measurements.

ShortName	Latitude	Longitude	Raidus
Albuquerque	35.2	-106.55	0.5
Atlanta	33.8	-84.35	1
Austin	30.26	-97.74	1
Bakersfield	35.3	-119	0.5
Baltimore	39.3	-76.2	1
Boston	42.45	-71	1
Charlotte	35.25	-80.85	1
Cheyenne	41.1	-104.8	1
Chicago	41.8	-87.7	1
Cincinnati	39.1	-84.55	1
Cleveland	41.45	-81.67	1
Columbus	40	-83.1	0.5
Dallas	32.85	-96.95	1
Denver	39.75	-105	1
Detroit	42.35	-83.1	1
Fresno	36.7	-119.75	0.5
Houston	29.8	-95.25	1
Indianapolis	39.8	-86.15	0.75
Jacksonville	30.45	-81.6	0.5
Kansas City	39.15	-94.55	1
Knoxville	35.95	-84	0.75
Las Vegas	36.2	-115.2	1
Los Angeles	34	-117.9	1
Memphis	35.1	-90.1	0.5
Miami	26.05	-80.3	1
Minneapolis	44.95	-93.25	1
Montreal	45.6	-73.7	1
Nashville	36.2	-86.6	0.5
New Orleans	30.05	-90.3	1
New York	40.85	-73.7	1
Omaha	41.3	-96.05	0.5
Orlando	28.5	-81.3	0.5
Philadelphia	40	-75.2	0.5
Phoenix	33.6	-112	1
Pittsburgh	40.4	-79.95	1
Portland	45.45	-122.55	1
Reno	39.55	-119.7	0.5
Richmond	37.4	-77.3	0.5
Sacramento	38.65	-121.4	0.75
Salt Lake City	40.7	-111.95	0.5
San Antonio	29.55	-98.45	0.5
San Diego	32.8	-117	1
San Francisco	37.6	-122	1
Seattle	47.35	-122.25	1
St Louis	38.65	-90.35	1
Tampa	27.9	-82.4	0.75
Toronto	43.7	-79.5	1
Tucson	32.25	-110.85	0.5
Washington DC	38.9	-77	0.75

Table B.2: Summary of cities and radius.

Hyperparameter	Range	Selected value
max_depth	[6, 10]	9
min_child_weight	[1, 5]	2
eta	[0.1, 0.4]	0.3
gamma	[0, 1]	0

Table B.3: Summary of hyperparameters and their ranges used in the cross validation and the selected hyperparameters in the ML configuration.

OH prediction sets	# of models	Trained on	Column data source
General-WRF	1 for all cities	All urban WRF-Chem data	WRF-Chem
General-Satellite	1 for all cities	All urban WRF-chem data	OMI
City-WRF	49, one per city	WRF-Chem data for each respective city	WRF-Chem

Table B.4: Summary of the different OH prediction sets used in this work.

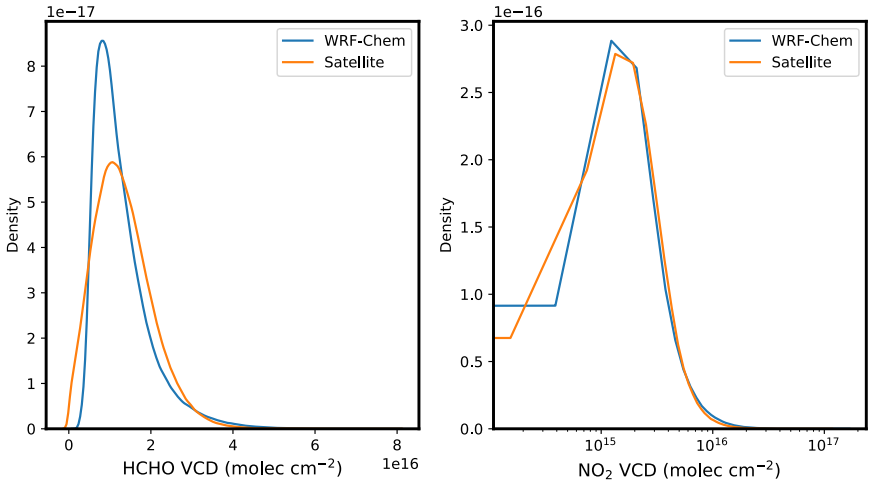

Figure B.1: The kernel density estimate (KDE) plots of HCHO column (a) and NO_2 column (b) from both WRF-Chem and satellite observations.

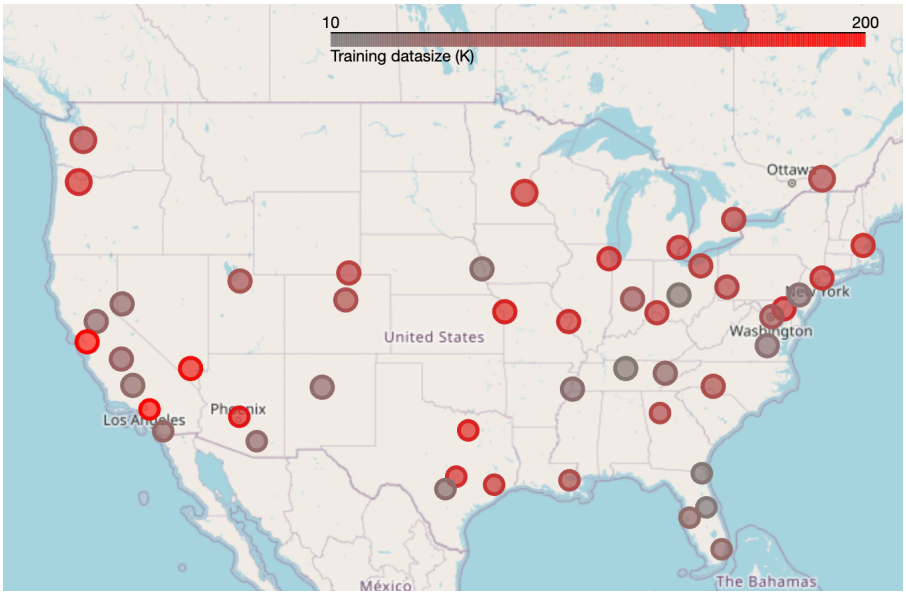

Figure B.2: The map of training data size for each city in the city-specific ML training system.

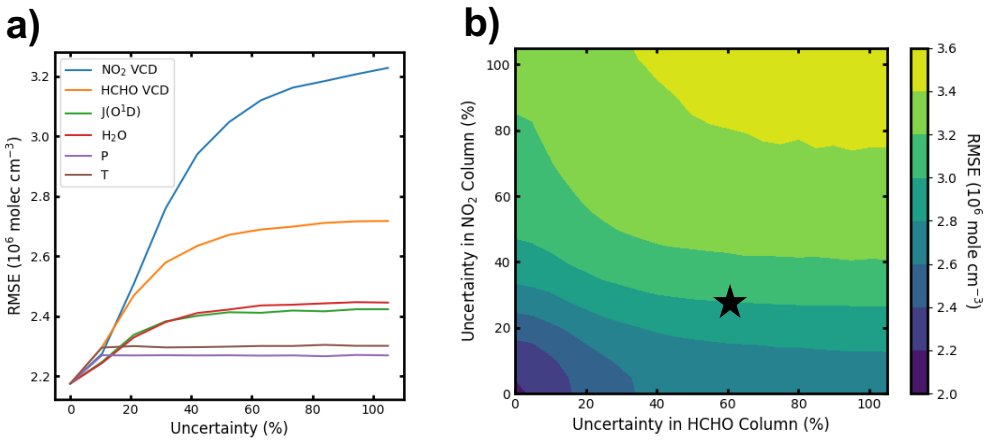

Figure B.3: The evaluation of uncertainty propagated through the uncertainty introduced in the feature sets. a) The RMSE as a function of uncertainty level prescribed to each feature denoted by different colors and b) the augmentation of RMSE with respect to uncertainties both in NO_2 column and HCHO columns. The star symbol marks the uncertainty level for the satellite retrieval products used in this study; 30% for NO_2 column and 60% for HCHO column, respectively.

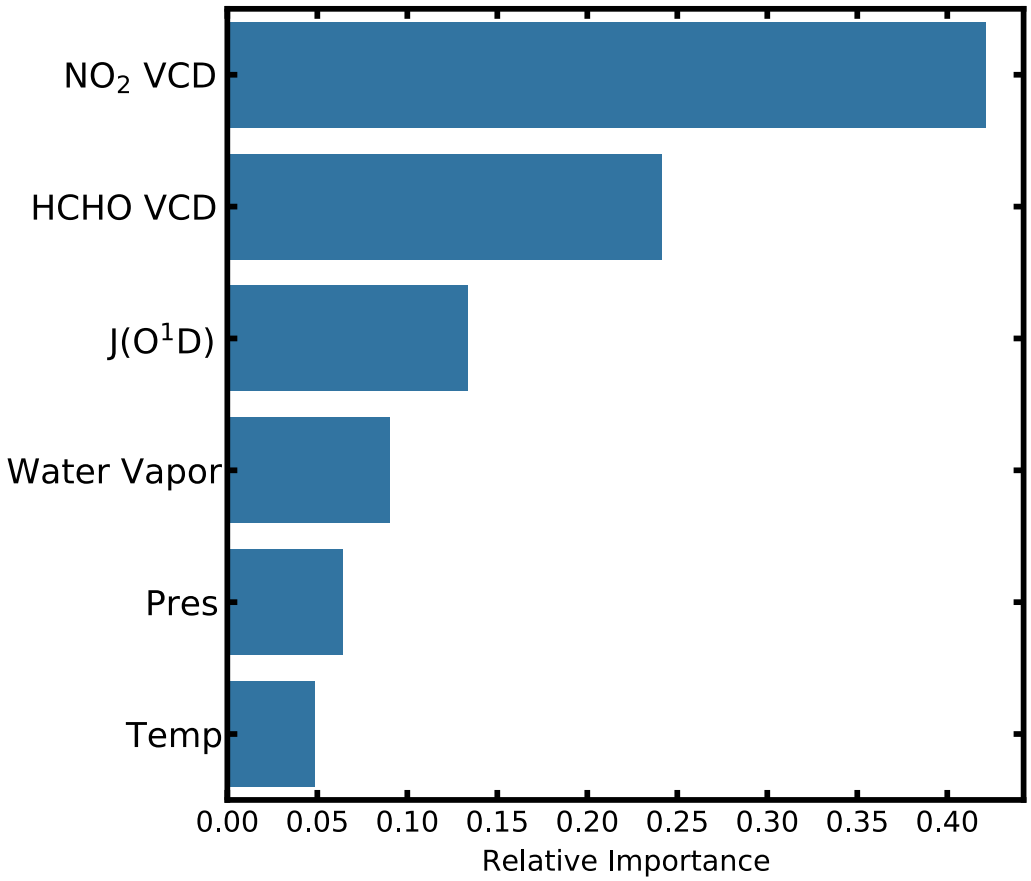

Figure B.4: The relative importance of features of from the generalized model.

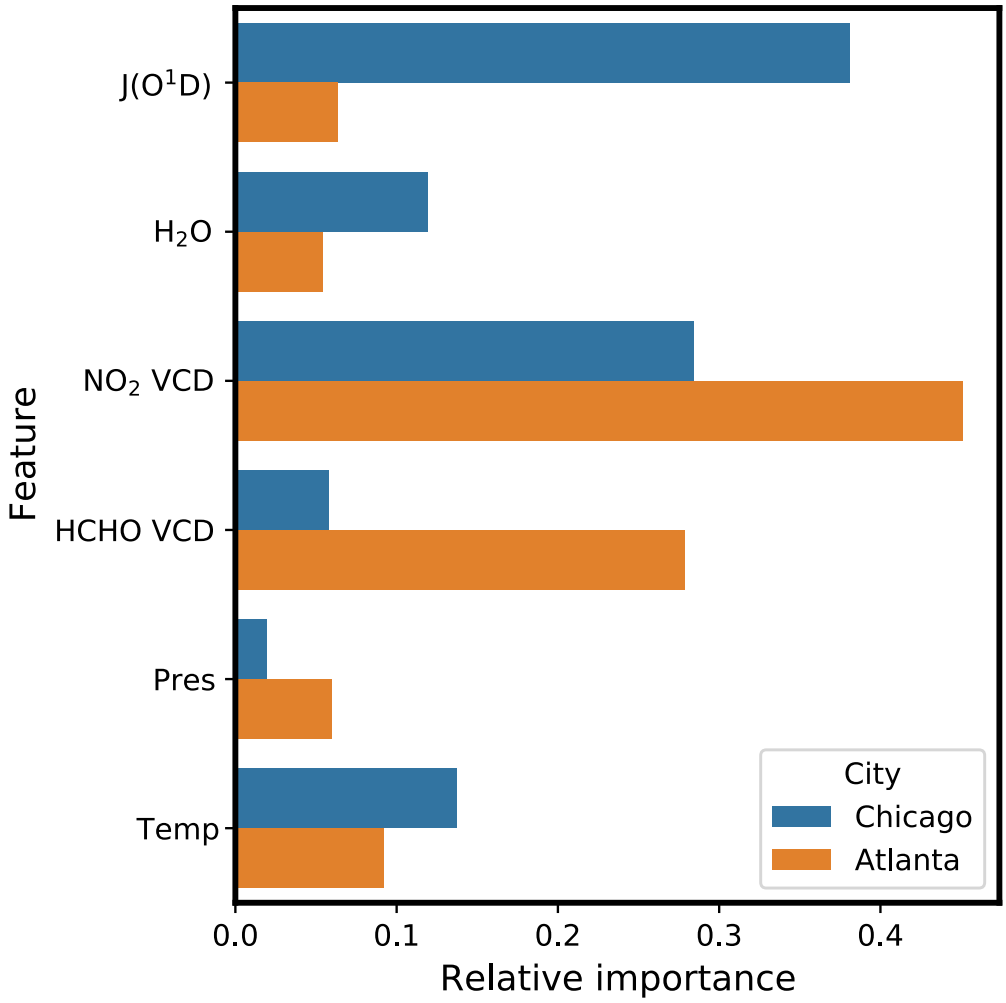

Figure B.5: The relative importance of features from two models representing urban OH chemistry over Chicago and Atlanta.

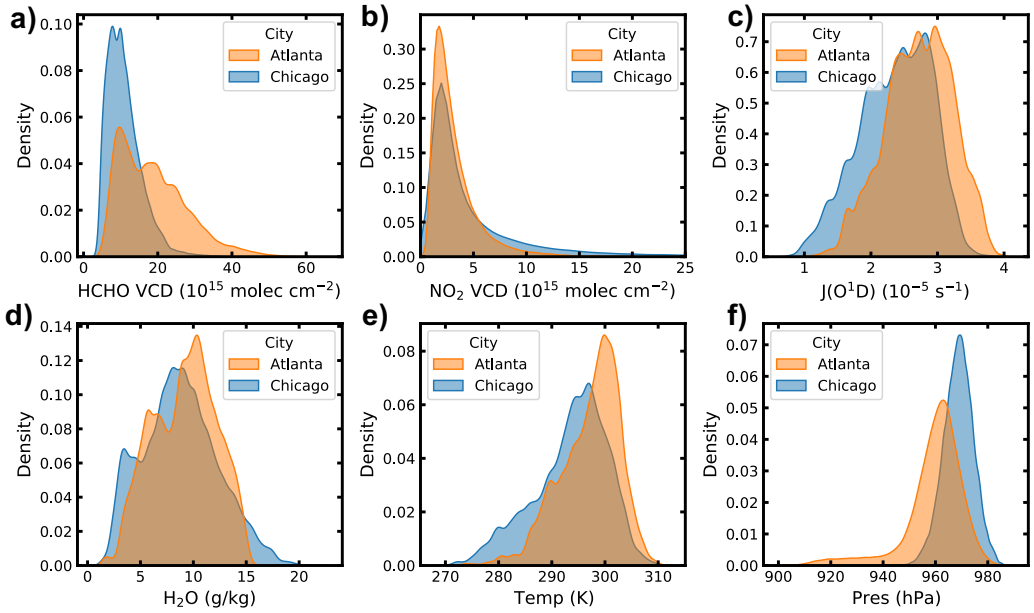

Figure B.6: The comparison of probability distributions for features across Chicago and Atlanta, including a) HCHO VCD, b) NO_2 column, c) J(O^1D), d) H_2O, e) temperature and f) pressure.

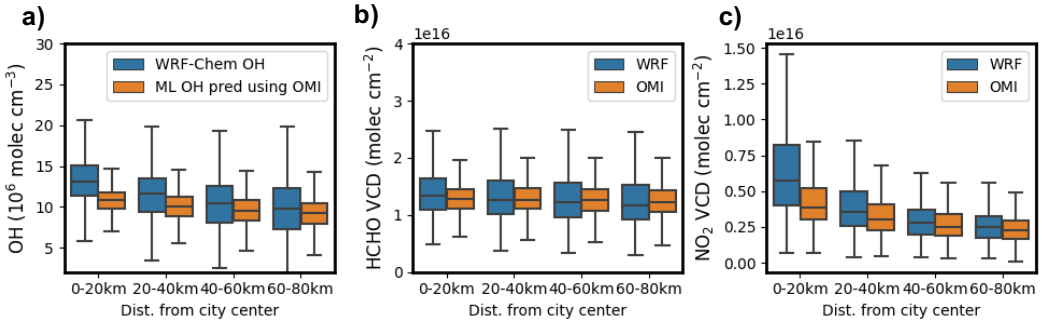

Figure B.7: The comparison of average spatial pattern for a) OH directly from WRF-Chem simulation and OH predicted from the ML model using observation-based features, b) WRF-Chem + OMI HCHO column and c) WRF-Chem + OMI NO_2 column.

Appendix C

Supplemental material for "Estimate of OH Trends over One Decade in North American Cities"

The chapter was adapted from the supplement of: Q. Zhu, J. L. Laughner, and R. C. Cohen (2022b). "Estimate of OH trends over one decade in North American cities". *Proceedings of the National Academy of Sciences* 119.16, e2117399119

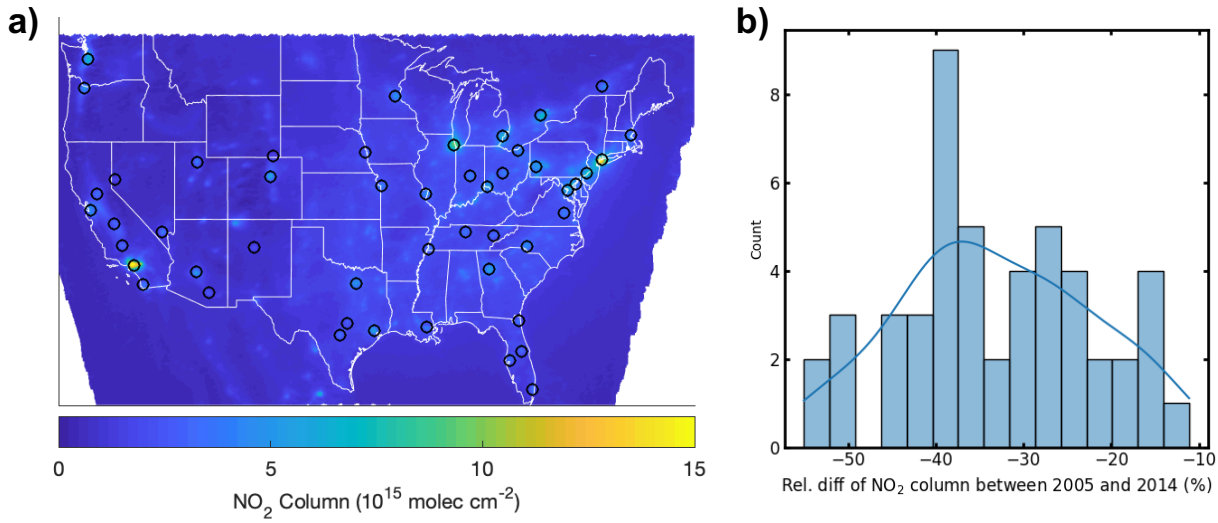

Figure C.1: The decadal average as well as decadal variation of NO_2 column observed from the space. a) The map of decadal average summertime NO_2 column between 2005 and 2014 over North America. The selected 49 cities are denoted by circles. b) the frequency distribution of the relative difference of NO_2 column between 2005 and 2014 over selected cities.

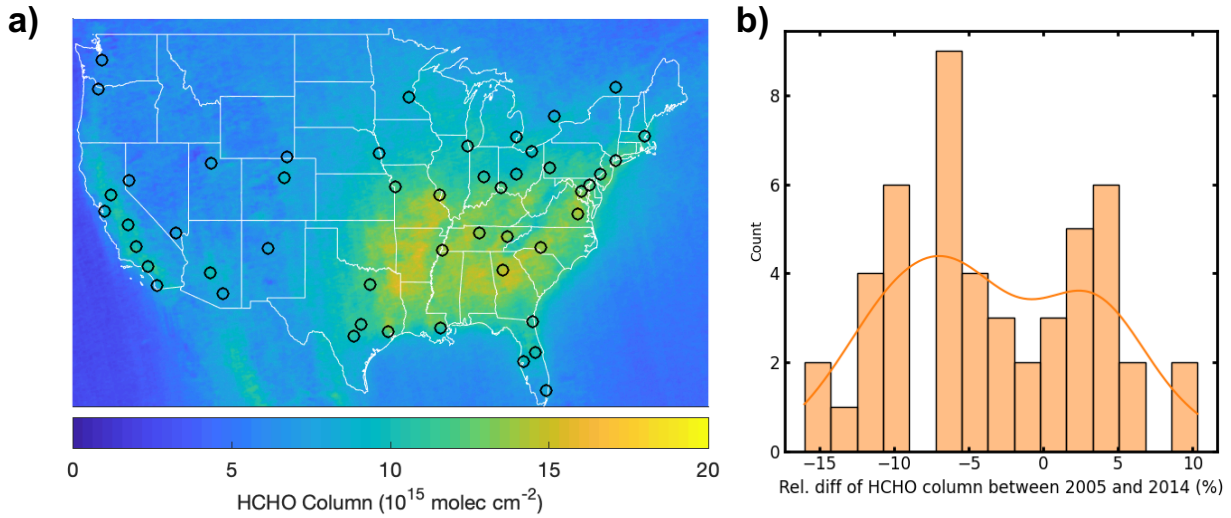

Figure C.2: The decadal average as well as decadal variation of HCHO column observed from the space. a) The map of decadal average summertime HCHO column between 2005 and 2014 over North America. The selected 49 cities are denoted by circles. b) the frequency distribution of the relative difference of HCHO column between 2005 and 2014 over selected cities.

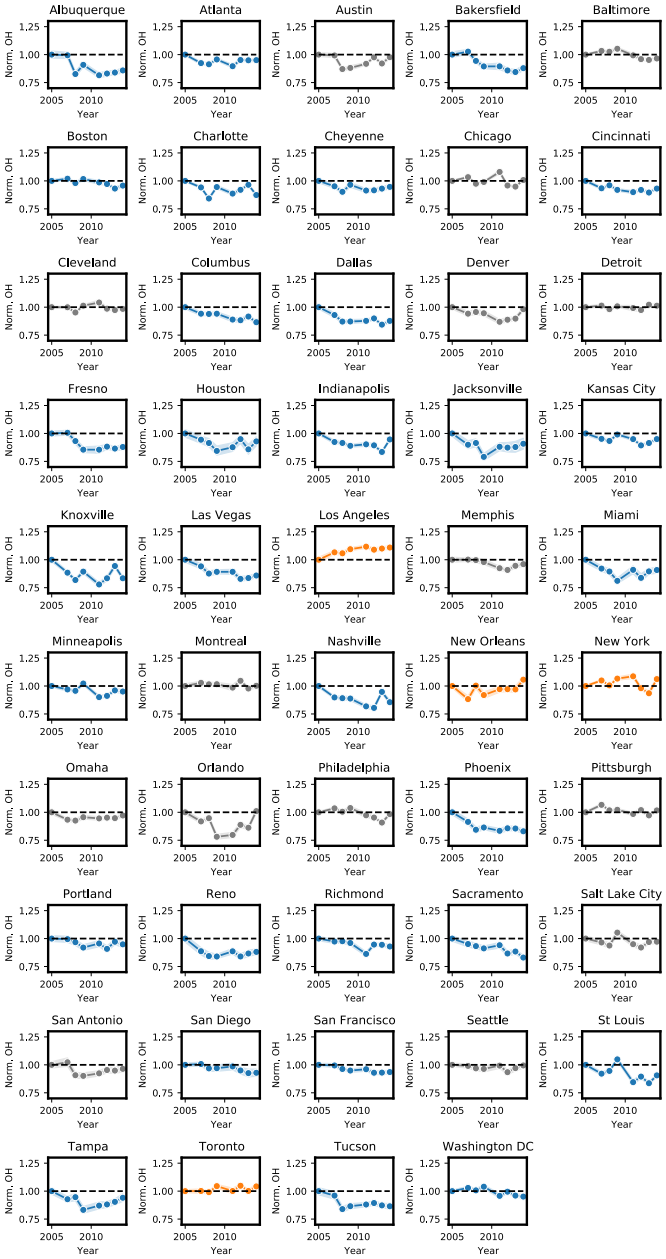

Figure C.3: The OH trends between 2005 and 2014 predicted by the ML model in 49 cities. The cities are categorized into 3 groups based on the relative difference between OH in 2005 and OH in 2014. 4 cities shown in orange present a statistically significant increase of OH, 30 cities shown in blue correspond to a statistically significant decrease of OH, whereas the remaining cities are shown in grey.

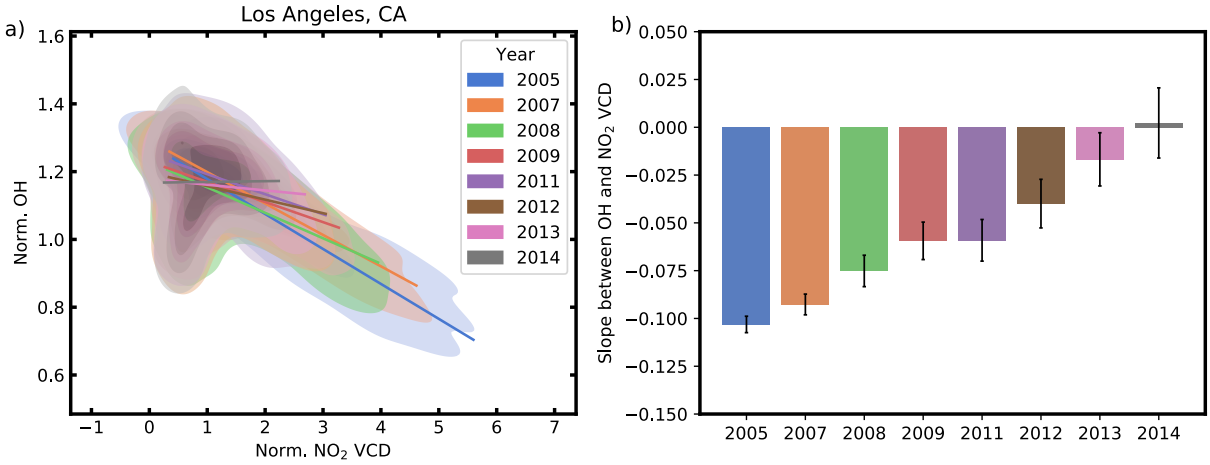

Figure C.4: The relationship of OH versus NO_2 column between 2005 and 2014 in Los Angeles, CA. Both OH and NO_2 columns are normalized to their annual average in 2005. a) shows the the density plot of normalized OH and normalized NO_2 column and the linear fits. b) shows the slopes from the linear regression results in a) over 8 years between 2005 and 2014. The error bar denotes the standard deviation of the fitted slope. 2006 and 2010 are excluded due to missing data.

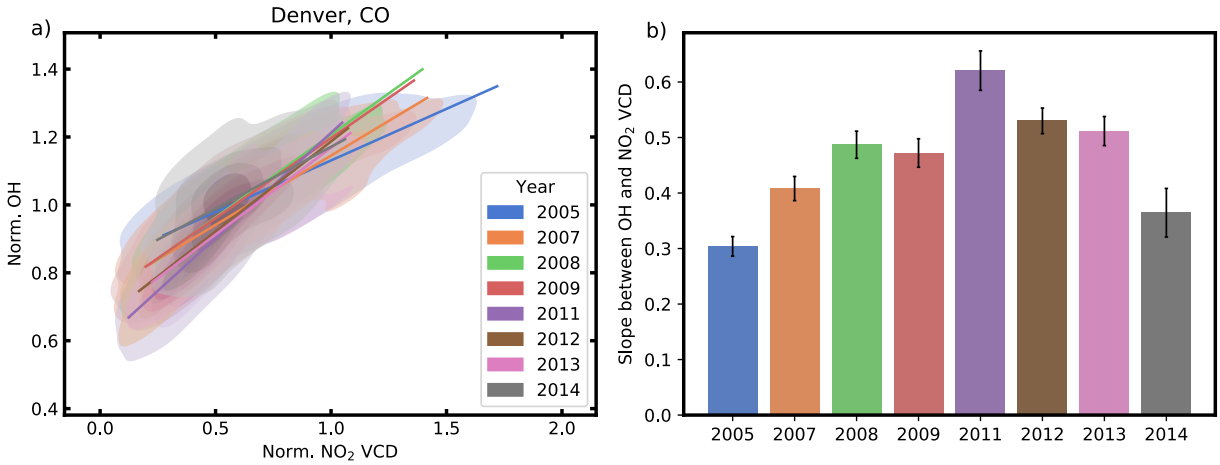

Figure C.5: The relationship of OH versus NO_2 column between 2005 and 2014 in Denver, CO, same as Fig. C.4.

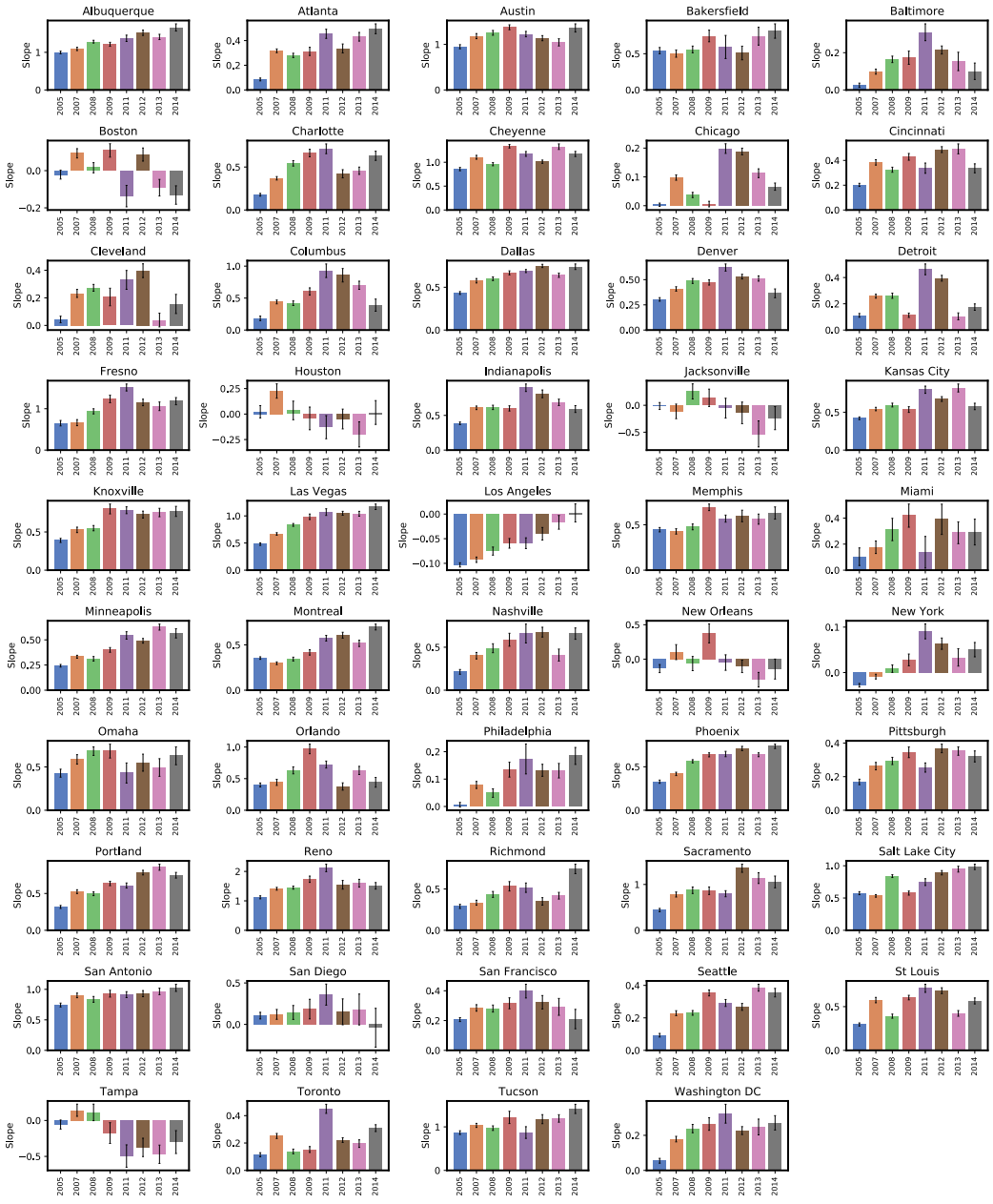

Figure C.6: The slope calculated from linear fitting between normalized OH and normalized NO_2 column among 49 cities over 8 years between 2005 and 2014, same as Fig. C.4 b) and Fig. C.5 b).